Technical University of Crete
School of Electrical and Computer Engineering

Multiband, Dynamic and Molecular Imaging

Master thesis by Theodoros-Marios Giakoumakis

Supervisor:	Professor Costas Balas
Committee:	Professor Michalis Zervakis
	Professor Minos Garofalakis

Chania 2016

Technical University of Crete

School of Electrical and Computers Engineering

Master Thesis

"Multiband, Dynamic Molecular Imaging"

Giakoumakis Theodoros – Marios

Supervisor: Professor Costas Balas

Abstract

Tumour heterogeneity describes differences of tumour cells either within the same malignant mass or amongst patients suffering from the same cancer type. It has only recently begun being explored by modern medical science and the repercussions in effective screening and treatment have yet to be fully understood. While research is progressing in search of new biomarkers, there is an increasing tendency to use multiple biomarkers to achieve more precise diagnosis. Under this light, we present a novel multiband bio photonic method and imaging modality capable of imaging in vivo dynamic phenomena and estimating and mapping functional and structural parameters of the observed tissue, fully customizable to record a given set of biomarkers. Complete spectral cube of dynamic phenomena, induced by multiple biomarkers, can be achieved by employing spectral estimation algorithms and single frame simultaneous acquisition of a limited number of spectral bands. The pharmacokinetics of each biomarker can be algorithmically separated, with use of regression algorithms, based on their spectral signature. In silico modeling of the pharmacokinetics of these biomarkers, using compartmental analysis, may adopt sets of biological parameters correlated with the observed response. Previous studies have reported a model of the cervical neoplastic epithelium which predicts the dynamic optical effects after the application of acetic acid. Global optimization analysis has proven that four structural and functional biological parameters correlated with cervical neoplasia can be accurately estimated, with the Differential Evolution (DE) algorithm achieving roughly 99% mean accuracy, as the best performing one. In the scope of this study, we proceed to estimate and map thousands of parameter sets from clinical data, using either DE or a look-up table (LUT) consisting of predefined solutions with at least 92% mean accuracy. The findings agree with literature. Moreover, the use of LUT is vastly time efficient compared to the use of DE, offering estimations within a couple minutes instead of days with similar accuracy levels. The suggested imaging modality can be proven an indispensable tool for reducing time and cost of screening procedures, by providing accurate, quantitative and objective information of biological parameters after the application of multiple biomarkers, while on the same time can be used to further understand dynamic phenomena through real time spectral imaging.

Acknowledgements

Table of Contents

Table of Figures

0. Introduction

Despite common belief, cancer has existed for all of human history. At around 1600 BC in the Egyptian Edwin Smith Papyrus exist an early description of breast cancer. It was the father of modern medicine, Hippocrates, the one that has given the name to the disease when he described several kinds of it. He referred to them with the Greek word "καρκίνος", *karkinos*, which is the Greek word for crab or crayfish. It occurs from the appearance of the cut surface of a solid malignant tumour, with "the veins stretched on all sides as the animal the crab has its feet, whence it derives its name". The ancient Greek physician Galen stated that "cancer of the breast is so called because of the fancied resemblance to a crab given by the lateral prolongations of the tumor and the adjacent distended veins". The Roman encyclopaedist Celsus translated *karkinos* into the Latin *cancer*, also meaning crab and recommended surgery as treatment in contrast with Galen's recommendation on purgatives. These recommendations largely stood for a thousand years.

It is only in medical advancements of the previous century that the true origins of the disease have begun to be accurately understood based on scientific evidence rather than educated speculations based on experience, and the true origins of the disease down to cellular level have begun to unravel. Yet it is no more than a decade that malignant tumour that lead to cancer have seized to be viewed as a concrete mass of either dead or mutated cells and the heterogeneity and complexity of tumours has started to be explored.

Understanding tumour heterogeneity is considered a crucial step in the fight against the disease, as hidden aspects of neoplasia are understood and thusly can be more effectively and accurately treated. Before stepping into treatment though, new screening methods that are of high sensitivity and specificity need to be established, preferable of low cost and wide field applicable. Towards that direction, studies towards new biomarkers are made, in hopes of a breakthrough.

Within this Master Thesis, a novel imaging modality that incorporates spectral imaging and compartmental modelling is defined with a wide spread of applications from simple observation to low cost alternative for tumour screening of mass volume populations. Spectral imaging is based on the Real Time Spectral Mapper, a real time spectral imaging system with capabilities of real time classification of spectra. Spectral fidelity of this system is further investigated and refined by understanding the spectral overlapping and the channel cross-talk phenomenon of silicon based sensors. This imaging technology enables accurate observation within a field of the electromagnetic spectrum of dynamic phenomena, while observing the temporal and spatial distribution of the concentration of a given set of stains and biomarkers.

Moreover, estimation of functional and structural parameters of the tissue and presentation of their spatial distribution with high accuracy and within a time frame suitable for clinical application is presented. The estimation is based on the solution of the inverse problem posed by a previously reported dynamic compartmental model and clinical trials of a dynamic contrast enhanced optical imaging system, which enables identification of malignant tissue in the epithelium of the cervix. Finally, the combination of said spectral imaging system and compartmental model as presented within the thesis, enables imaging and simultaneous application of multiple biomarkers, in vivo, in real time and non-invasively, thusly leading to more accurately discern of tumour heterogeneity and severity of the malignancy.

In chapter 1, an introduction to the basics causes and effects neoplasia leading to cancer are explored. Tumour heterogeneity is defined and the basic principles of a biomarker are defined.

In chapter 2, an introduction in spectral imaging is given, stating the basic principles of electromagnetic wave theory, its interaction with matter and as consequence with living tissue and state of the art imaging that exploits these phenomena.

In chapter 3, spectral overlapping of the electromagnetic responses recorded by a common sensor and the channel cross-talk phenomenon are identified alongside with their effects in imaging. Steps towards their elimination are presented, in the form of a simple algorithm.

In chapter 4, practical application of the said algorithm is assessed in microscopy tiles. Moreover, the effect of the algorithm in spectral estimation is measured.

In chapter 5, focus on intraepithelial cervical cancer is made and state of the art screening techniques of this form of malignancy, as an introduction to a biomarker induced dynamic phenomenon where the imaging modality can have a full scale application. Moreover, a previously developed biomathematical and biophysical model of the phenomenon is presented.

In chapter 6, the inverse problem is defined and the existence of its solution is explored through global optimisation and proposed. The proposed solution by the means of a global optimisation algorithm and a look up table based, is applied and compared towards one another, on real data gathered from clinical trials. Pseudo-colour maps of structural and functional parameters of the underlying tissue are drafted, as one of the primary capabilities of the proposed imaging modality

In chapter 7, the look up table based solution of the inverse problem is presented in detail and initial steps towards its refinement are presented.

In chapter 8, conclusions of this thesis are gathered and a complete generic presentation of the proposed imaging modality is given. Finally, future endeavours towards the next steps of calibrating and advancing the imaging modality are proposed.

1. Neoplasia and Tumour Heterogeneity

1.1 Neoplasia

The biological state of abnormal growth of tissue is characterised as neoplasia. When this proliferation forms a critical mass, it is commonly referred to as tumour. Although common, it is not always that a mass is formed, as lies the possibility that the immune system can regress the condition to normal state. Before entering the state of neoplasia, cells often undergo abnormal patterns of growth, such as metaplasia or dysplasia, which are reversible and not always progress to neoplasia.

Neoplasm are classified into four main groups according to World Health Organisation (WHO) [1]. These classes are

- Benign neoplasms. Circumscribed and localised masses that do not evolve into malignant.
- In situ neoplasms. Localised, non-invasive and destructive masses that hold the potential to evolve into malignant.
- Malignant neoplasms, also known as cancers. Invasive and destructive to the surrounding tissue masses. Hold the potential of metastases to other organs and lethal if left untreated or fail to respond to treatment.
- Neoplasms of uncertain or unknown behaviour. Metastatic neoplasm with unknown origin site of primary cancer.

Masses that are metastatic of a primary tumour or tumour occur following treatment such as chemotherapy and radiotherapy, are referred to as secondary neoplasm.

1.2 Cancer

A collection of related diseases, that manifest uncontrollable cell division and propagate into surrounding tissue, is commonly referred to as cancer. Human cell growth under normal circumstances serve at replacing aged or damaged cells. As such, the potential of malignant tumour lies in the entirety of the human body. When cancer develops, this cell replacement procedure becomes rather chaotic, with cells evolving into abnormal functional and structural morphologies, old or damaged cells surviving natural cell death and new cells forming uncontrollably. This overproduction of cells is what roughly formulates masses called tumours. Most commonly solid tumours are formed, yet there are cancer types that do not, such as types of leukaemia, which are cancers of the blood.

As cancerous tumours are referred all the malignant ones and hold the potential of spreading into or invading nearby tissues. Moreover, it is not uncommon to manifest metastasis. During this process, cancerous cells are separated from the main mass and relocate at distant tissue through blood or the lymph system. This can lead to manifestation of new tumour sites away from the original. Moreover, unlike benign tumours, when removed, a risk factor of reappearing and growing to a critical mass still lingers.

1.2.1 Cancer hallmarks

According to [2] there are six biological capabilities acquired in cellular level during the development of cancer. This capabilities are referred to as hallmarks. In [3], additional two emerging hallmarks were added, as well as two enabling characteristics. The hallmarks include:

Initially introduced hallmarks

- *Sustaining Proliferative Signalling.* It is considered the most fundamental trait of cancer cells. Under normal circumstances tissues regulate through external signalling the production or destruction of cells, sustaining cell population and maintaining tissue architecture. Under malignant progression, cancer cells develop the ability to deregulate these signals and self-signal proliferation inducing cellular growth in size and population.
- *Evading growth suppressors.* In response to the first hallmark, growth suppressing signals are induced in an attempt to reverse constant proliferation. The second hallmark refers to the ability developed by cancerous cell to avoid these signals.
- *Resisting Cell Death.* The natural end of a cell as part of a tissue is a regulated process, named apoptosis. During apoptosis, in simplified terms, a given cell is recycled by giving consensus to be consumed by neighbouring cells. Cancer cells, develop the ability to resist apoptosis inducing signals. As a result, the cell eventually becomes necrotic, a state in which bloats and explodes, releasing their contents to the surrounding microenvironment.
- *Enabling Replicative Immortality.* Normal body cells have a limited number of growth-and-division cycles, due to portion of DNA known as telomeres that shortens with every cell division. In contrast, cancer cells develop the ability to potentially enter an unlimited number of these cycles, by manipulating enzymes increasing the length of telomeres.
- *Inducing Angiogenesis.* Whether cells are cancerous or normal, access to nutrition and oxygen as well as disposal of metabolic waste and carbon dioxide remain indispensable part of their life cycle. Cancer cells develop the ability to constantly signal the tissue, requesting constant creation of vasculature in order to remain access to nutrition and dispose waste.
- *Activating Invasion and Metastasis.* In cellular level this hallmark describes the alterations developed in regards with their shape and attachment with surrounding cells.

Emerging hallmarks

- *Avoiding Immune destruction.* This emerging hallmark, marks the inability of the immune system to identify and eliminate neoplastic cells.
- *Deregulating Cellular Energetics.* In direct correlation with the alterations of cellular life cycle cancer cells manifest differences in terms of regulating their metabolism.

Enabling characteristics

- *Genome Instability and Mutation.* A succession on alterations in the genomes of neoplastic cells enable the manifestation of the aforementioned hallmarks.
- *Tumour-Promoting Inflammation.* This characteristic refers to the attempts of the immune system to eradicate neoplastic cells.
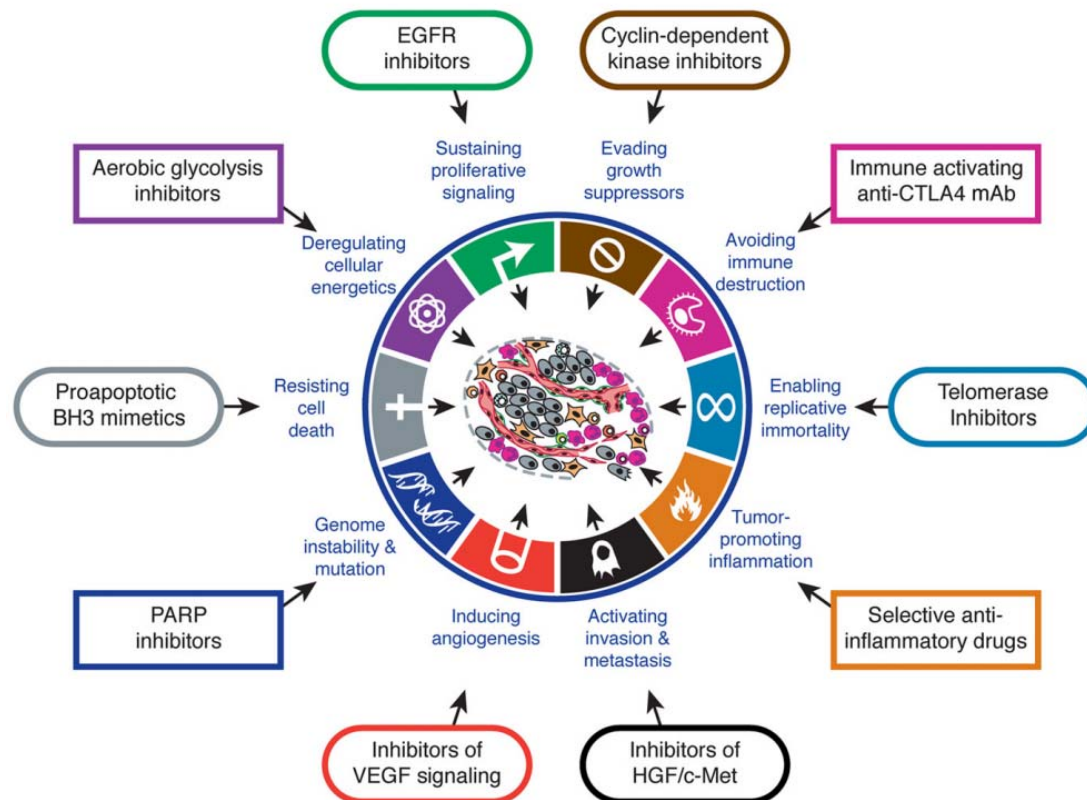
Figure 1 Hallmarks of Cancer and Corresponding Therapeutic Targeting

Research on understanding the reasons and mechanics behind the manifestation and progression of these hallmarks and characteristics, led to the manufacturing of targeted therapies and drugs in order to inhibit and reverse them as a targeted treatment. Most of these drugs target specific molecules involved in some way in enabling particular capabilities. This holds the advantage of reducing potential side-effects

1.2.2 Symptoms

Like most diseases, cancer manifests symptoms. Most of them depend on the organ that cancer originates, yet there are some general symptoms including weight loss or tiredness. Moreover, the symptoms depend on the type of cancer, leading few symptoms being specific. This leads to variations in manifestation in a population of patients. Due to the large variation of cancer types there is also a wide range of signs and symptoms, as well as variations in their manifestation. All these factors contribute in many misdiagnosis and treatment of cancer as other illnesses.

Typical symptoms include:

- unusual lumps or masses in the body
- Alterations in skin moles, such as size, colour or shape thickness
- Persistent cough or hoarseness
- Change in bowel habits, for instance diarrhoea or constipation
- Difficulties in swallowing or digestion
- Abnormal bleeding
- A persistent sore or ulcer
- Difficulties in urination
- Unexplained weight loss
- Unexplained ache
- Unexplained fatigue
- Skin changes, for example unexplained rashes
- Unexplained night sweats
- Abdominal pain

1.2.3   Causes

In general, it is impossible to pinpoint the actual cause of a particular cancer, due to the absence of fingerprints to various causes. The majority of cancers are provoked due to environmental factors and a small percentage due to inherited genetics. As environmental are characterised all factors that are not induced by inherited genetics and not just pollution as to what the term commonly refers to. Such factors can mean also lifestyle or behaviour. In general cancer as a disease is not transmissible, with the rare exception such as pregnancies or organ donating. On the other hand, there are certain cancer inducing factors that can be transmissible such as cancer inducing virus. An example of this virus is the Human Papilloma Virus (HPV) that is one of the main causes of neoplasia in the epithelium of the cervix leading to cervical neoplasia.

Common factors include:

- Tobacco use and contact with other chemicals substances, characterised as carcinogens.
- Diet, obesity and lack of physical activity
- Infections, by cancer inducing diseases. The usual suspects are viruses, referred to as oncoviruses.
- Exposure to radiation, both ionizing and non-ionizing
- Stress
- Heredity of genetic defects.
- Physical agents inducing chronic inflammation due to their physical effects, like for instance prolonged exposure to asbestos.
- Hormones that may promote cell proliferation.

1.2.4   Diagnosis

A definitive diagnosis requires the examination of a tissue sample by a pathologist. Due to the nature of cancer though, it is mostly recognised by signs or symptoms or through screening procedures. Medical tests including blood tests, X-rays, CT and PET scans as well as endoscopy is usually employed to investigate whether someone has cancer.

Screening

Unlike diagnosis prompted by symptoms or signs, screening aims to detect cancer at primal stages before said symptoms appear, thusly aiding in more efficient treatment. These involve medical tests, such as blood and urine tests, physical examination or medical imaging [4].

Often large groups, usually within a specific age group, undergo screening, usually referred to as universal screening, mass screening or simply population screening. On the other hand selective screening refers to identifying people at higher risk, such as people with family history.

The efficiency of screening procedures is not without err, thusly it is not uncommon for false positive results, where healthy individuals are suspected of cancer, or false negative results, where cancer patients are dismissed as healthy and existing cancers fail to be identified in early stages.

For a screening test to be accepted and widely used, it must be effective, safe, well-tolerated and with acceptable sensitivity and specificity. Meaning it must be sensitive enough in recognising cancers and accurate enough as to not have high rates of false positive results. If signs of cancer are detected, more definitive and invasive follow-up tests are performed to reach a diagnosis. Screening for cancer can lead to cancer prevention and earlier diagnosis. Early diagnosis may lead to higher rates of successful treatment and extended life. Consequently, several factors are considered to determine whether the benefits of screening outweigh the cost and potential risks of a screening procedure. These include:

- Possible harm directly from the test, such as for instance exposure to harmful ionizing radiation during X-ray imaging.
- Sensitivity and specificity of the procedure.
- Occurrence likelihood of the suspected cancer. Screening procedures for rare cancers are not considered normally as useful
- Possible harms from follow-up procedures
- Availability of suitable treatment
- Impact on treatment efficiency
- Necessity of treatment
- Nature of procedure. If for example it is invasive or painful, people will tend to reject to undergo such procedure for screening purposes.
- Cost

1.2.5   Classification

Cancers are usually classified by what resemblance the tumour cells have with other human cells. These cells are presumed to be the origin of tumour [4]. These types include:

- ***Carcinoma***: Cancers derived from epithelial cells. This group includes many of the most common cancers and include nearly all those appearing in the breast, prostate, lung, pancreas and colon.
- ***Sarcoma***: Cancers arising from connective tissue, such as bone, cartilage, fat and nerve. They develop from cells originating in mesenchymal cells outside the bone marrow.
- ***Lymphoma*** and *leukemia*: When cancerous hematopoietic cells leave the marrow and mature in the lymph nodes (lymphoma) and blood (leukemia)
- ***Germ cell tumour***: Cancers derived from pluripotent cells, most often presenting in the testicles or the ovary.
- ***Blastoma***: Cancers derived from immature cells or embryonic tissue.

It is not rare cancers to be named for the size and shape of cells during microscopic examination, such as giant cell carcinoma or small-cell carcinoma.

1.2.6   Research

With current medical advancements and taking the nature of cancer into account, it is highly unlikely that a single cure for cancer can be find. High competition among researchers for low amount of financial resources has limited cooperation between research groups as well as attempts for highly innovative risky research. Yet on the same time, continuous improvements in understanding molecular and cellular biology has allowed for advancements in diagnosis and treatment.

In clinical trials, various experimental cancer treatments are researched and compared to the best existing ones. In case of successful treatment of a single cancer type, it is accustomed to be tested against other types. Moreover, novel diagnostic tests are under development in order to better target therapies, personalised for each patient based on each individual needs and biological differences.

Cancer research focuses on causes and effects such as:

- Agents, such as virus, or events, such as mutations, that provoke or advance cellular changes at a genetic level.
- The precise nature of the genetic damage and the genes that are affected by it
- The consequences of those genetic changes on the biology of the cell, both in generating the defining properties of a cancer cell and in facilitating additional genetic events that lead to further progression of the cancer.

1.3   Tumour heterogeneity

Tumour heterogeneity refers to differences observed in the morphology and the phenotypic profile of different tumour cells [5]. This phenomenon occurs both between tumours of different type (inter-tumour heterogeneity) and within tumours of the same type (intra-tumour heterogeneity). These diversities pose a significant challenge in designing and introducing effective treatment strategies. Therefore, a significant portion of research is targeting in understanding and characterizing heterogeneity, thusly allowing for a better understanding of the causes and progression of the disease. In turn, this holds the potential of creating more refined treatment strategies incorporating knowledge of heterogeneity achieving higher efficiency.

Research on tumour heterogeneity has led to a broad definition of cancer development as an evolving process. Due to the nature of the disease, where multiple mutations accumulate, and with inherited genetic differences among human population, heritable heterogeneity has been until recently the main focus of study. On the other hand, it is only recently that the structural differences of the sublcones of tumours and the tumour microenvironment, significantly contributing to tumour evolution, development and outcomes of clinical treatment [6].

Multiple types of heterogeneity have been observed between tumour cells, stemming from both genetic and non-genetic variability. This complexity originates from inherited genetic differences, interactions between expressions of different genes interacting with each other as well as with their environment, and from interactions between neoplastic cells and their micro-environment [6]. This multiple additive sources of complexity results in highly heterogeneous phenotypes, which in turn express themselves in a diversity of symptoms, as well as response to treatment.

Due to the genetic heterogeneity, biomarkers that may predict treatment response or prognosis may not be widely applicable. However, it has been suggested that the level of heterogeneity can itself act as a biomarker. In increased number of different subclones lies the chance for a subclones that may resist treatment. Further research into developing biomarkers that account for heterogeneity is still in progress.

1.3.1   Tumour microenvironment

Heterogeneity between tumour cells can be further increased due to heterogeneity in the tumour microenvironment. Spatial differences in the tumour, such as for instance availability to nutrition or oxygen may impose different selective pressures on tumour cells, leading to a wider spectrum of dominant subclones in different tissue regions of the tumour. The influence is also a likely reason for the heterogeneity between primary and metastatic tumours seen in many patients, as well as the inter-tumour heterogeneity.

1.3.2 Models of heterogeneity

Two models are used in order to explain the heterogeneity of tumour cells, the cancer stem cell model and the clonal evolution model. The models are not mutually exclusive, and it is believed that they both contribute to heterogeneity in varying amounts across different tumour types.

Cancer Stem Cells

The cancer stem cell model asserts that within a population of tumour cells, there is only a small subset of cells that are able to form tumours. These cells are termed cancer stem cells (CSCs). They possess the ability to both self-renew and differentiate into non-tumorigenic. The CSC model is based on the assumption that differences in the stem cells result to differences observed between tumour cells. Stem cell variability can be result of epigenetic changes or clonal evolution of the CSC population, where advantageous genetic mutations can accumulate in CSCs. Evidence of the cancer stem cell model has been demonstrated in multiple tumour types including leukemias, glioblastoma, breast cancer and prostate cancer. On the other hand, the existence of CSCs is still under debate, with one reason for this being that markers for CSCs have been difficult to reproduce across multiple tumours.

Clonal Evolution

In the clonal evolution model, tumours occur from a single mutated cell, accumulating additional mutations as it progresses. This proliferates to subpopulations, each with the ability to divide and mutate further. This chain of mutations may give rise to subclones that possess an advantage over the others within the tumour environment and may become dominant in the tumour over time. When proposed, this model allowed for the understanding of tumour growth, treatment failure, and tumour aggression that occurs during the natural process of tumour formation.

Evolution of the initial tumour cell may occur by two methods:

- *Linear expansion*: Sequentially ordered mutations accumulate, resulting in clonal expansion of tumour cells. Mutations are a stochastic process, thusly it is unlikely to reflect the endpoint of a malignant tumour.
- *Branched expansion*: Expansion into multiple subclonal populations occurs through a splitting mechanism. This method is more associated with tumour heterogeneity than linear expansion.

1.4 Biomarker

A biomarker, also known as biological marker, is an index or in some cases a substance, that can be detected and measured in parts of the bode like the blood or tissue and indicate a biological state or condition. In some cases, their use is imperative in achieving or simply confirming a prognosis. Biomarkers can be difficult to validate and require multiple points of validation.

Specifically in medicine, in most cases a biomarker is defined as a substance that can be traced and is introduced in the body as means of organ examination and monitoring or as an indicator of existence, absence or degree of manifestation of disease state. Other biomarkers include brain volumetric measurements or measurements of electrical activity. Furthermore, in cases of cancer detection, mutant proteins are attempted to be detected, since they can be expressed by genetic degradation found in existing tumour [8].

There are disease-related and drug-related biomarkers. Disease-related biomarkers can be further distinguished to risk indicator or predictive biomarkers, diagnostic and prognostic biomarkers. Predictive biomarkers help project the effect of a treatment. A diagnostic biomarker is used to identify the existence of a disease, while on the other hand a prognostic biomarker indicates the development of a disease in a case of study regardless of type of treatment [9]. On the other hand, drug-related biomarkers indicate effectiveness and potential pharmacodynamics of a drug. Biomarkers used for personalised medicine typically fall under the prognostic or predictive categories. Clinical use of a biomarker needs high sensitivity and specificity, usually over 90% in order to be widely used.

There can be multiple ways to classify a biomarker, based on different parameters. Such classification can be:

- Imaging biomarkers, usually non-invasive, providing qualitative as well as quantitative data.
- Molecular biomarkers, indexes to biophysical properties in a sample.
- Diagnostic biomarkers
- Disease prognosis biomarkers
- Monitoring biomarkers
- Pharmacodynamics biomarkers, indexes to certain pharmacological response.

A cancer biomarker refers to a substance or a process that validates the presence of a cancer. It can be a protein or a molecule produced by the tumour or simple a specific bodily response. Multiple cancer biomarkers are used in diagnosis, prognosis and treatment course decision, response and monitor.

Identification, development and wide application of biomarkers has only recently begin to attract attention. In most cases, a simple validation of presence or a response over or under a certain threshold is used as indication, providing only qualitative information. Quantitative analysis is not yet widely employed and severely lacking, due to the difficulties of measuring and analysing biomarkers and their pharmacokinetics, more so when current procedures use in-vitro samples instead of in-vivo diagnosis.

1.5 Epilogue

Identifying, characterizing and treating tumour heterogeneity is still under active research with personalised treatment and more effective treatments as ultimate goal. Therefore, it is a rising need, to identify new and more robust biomarkers, while taking into consideration heterogeneity, with main focus of intra-tumour differences, as well as tumour microenvironment pressure [7].

However, most of current techniques for identifying heterogeneity involve invasive procedures for acquiring samples of the tumour. Wide field application of such screening techniques with heterogeneity identification purposes would be inapplicable, since tissue sampling from multiple regions is impractical for most cancer types. Moreover, in cases of metastasis it would require multiple samples from each tumour sighting, which is frequently unavailable [5]. On the other hand, cellular and molecular heterogeneity within a relatively small sample still holds potential predictive value.

Moreover, identifying and monitoring qualitatively and more importantly quantitatively analysing biomarkers, proves a whole new set of challenges. There is a wide variety of biomarkers, in both being introduced substances or tumour induced ones, each demanding a specific procedure or critical sample mass for application. Moreover, the application of a single biomarker might prohibit the use of another simple due to lack of available sample or unavailability of simultaneous signal acquisition due to technological insufficiency. Moreover, technology for biomarker signal acquisition in most cases might be of high cost and introduce high temporal complexity for a single diagnosis.

In this scope, the goal of this Master Thesis is to lay foundations for dynamic phenomena observation device capable of

- real time spectral imaging in order to spectrally de-convolve multiple biomarkers

- spatially and temporally estimate their concentrations and observe their pharmacokinetics

- estimate and map functional and structural variables of the tissue under study via inverse problem solution, by employing biomathematical model of the pharmacokinetics of a specific biomarker.

Within this Master Thesis, spectral fidelity of this system a real time spectral imaging system is further investigated and refined by investigating the spectral overlapping. Moreover, a previously reported by our group, dynamic compartmental model of the Acetic Acid cancer biomarker, that enables identification of malignant tissue in the epithelium of the cervix, as well as estimation of functional and structural parameters of the tissue, is further refined in order to achieve reduction of temporal complexity. Furthermore, we explore and propose the combination of said spectral imaging system and compartmental model, in order to enable application of multiple biomarkers, thusly more accurately discern tumour heterogeneity and severity of the malignancy.

2. Electromagnetic radiation

Electromagnetic radiation (EMR) is the radiant energy emitted by charged particles manifesting as magnetic (M) and electric (E) fields, perpendicular to each other and continuously oscillating, in sync. The substance through which waves of light travel is referred to as the **medium**. The maximum travelling velocity of this energy is through vacuum at 300.000 kilometers per second (186.000 miles per second) (*c* in vacuum, *v* in other media), with direction perpendicular to both fields. The physical distance of a full oscillation is known as the *wavelength* (*λ*). The height of the wave is known as the *amplitude*. *Frequency* (*f*) describes the number of vibrations of the wave per unit length of time. If we know the velocity and wavelength of an electromagnetic wave, we can determine its frequency using:

$$f = \frac{v}{\lambda} \qquad (2.1)$$
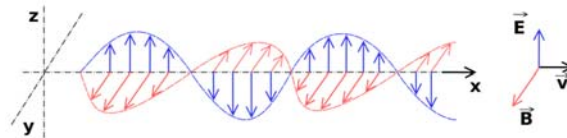
Figure 2 The Electromagnetic Waves are perpendicular and synchronous, towards one another, oscillating waves of electric and magnetic fields

2.1 Quantum Theory

Although the electromagnetic wave explanation of light seemed to be the most complete, it still failed to account for certain effects produced by light (i.e. visible by human eyes portion of EMR), like the photoelectric effect. In the early 1900s, Max Planck hypothesized that radiation was not simply produced in continuous waves of energy, but rather discrete (or individual) packets of energy that he called **quanta**. A few years later, Albert Einstein extended Planck's quantum theory to light, and called these packets—or particles—of energy **photons**. Einstein proposed that light consisted of streams of these high-speed energy particles. The energy of a photon is directly proportional to its frequency; so electromagnetic radiation with a higher frequency also has a higher energy level. Consequently, if we know the *frequency* of a wave of light we can determine the *energy* of its photons. . The energy of an individual photon is quantized and is greater for photons of higher frequency.

This relationship is given by Planck's equation:

$$E = hf = \frac{hc}{\lambda} \qquad (2.2)$$

Where,

- E is the energy per photon,
- h is Planck's constant.
- f is the frequency of the photon,
- c is the speed of the photon in vacuum
- λ is the corresponding wavelength of the photon

The *total* energy produced by waves of light will also be determined by the *number* of photons present, which is related to the *amplitude* of the light wave and its intensity. In modern theory, light has a **dual nature**, manifesting properties of both a particle and a wave. Essentially, light consists of high-speed particles of energy that travel in a wave-like manner, known as photons.

2.2 Visible Light and Colour

Electromagnetic radiation is divided into different sections, for convenience of study and vary from cosmic rays to radio wave. The portion of the spectrum that the eyes of each organism perceive varies depending the organism. **Light** is considered as the *visible* portion of the electromagnetic spectrum that the human eyes can perceive. This means that the radiation can stimulate the **photoreceptors** within the retina of the eye, creating a visual sensation. This region consists of electromagnetic radiation whose waves range from roughly 400 to 700 *nanometres* (nm) in length. The range of radiation visible to the human eye is referred to as the **visible spectrum**, ranging from violet (~400) at one end of the spectrum to red (~700) at the other, and represents a small fraction of the total electromagnetic spectrum.
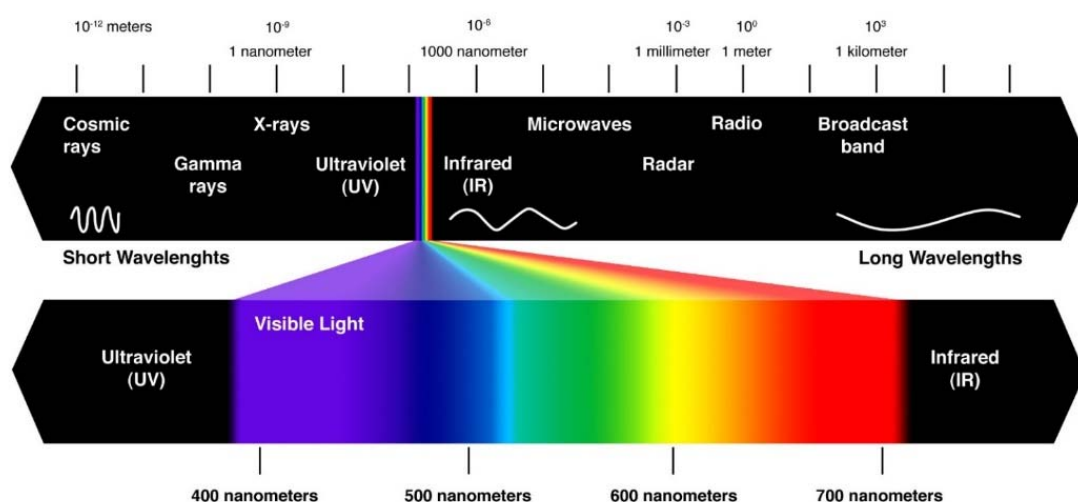
Figure 3 Spectrum of Electromagnetic Radiation with Focus on the visible light

White light is composed of the summation of wavelengths in the visible spectrum. Individual wavelengths within the visible spectrum, by themselves, create different colour sensations. These are the **spectral colours,** whereas the absence of wavelengths within the visible spectrum is perceived as the colour black. EMR with directly shorter wavelengths and as consequence higher frequencies than the visible spectrum is named **ultraviolet radiation**. EMR with directly lower frequencies and longer wavelengths than the visible spectrum is named **infrared radiation**. These two forms of radiation are *not* visible to the human eye. This thesis will focus on the visible spectrum, commonly referred to simply as light, with potential applications to a more broad scope of the EMR.

2.3   Light-Matter interaction

Light is **emitted** by a **luminous** or **primary source**, which is a source of energy that can generate visible radiation. Most other objects are visible because they **reflect** light from luminous sources. These objects are called **secondary sources**. When light is incident upon an object, the atoms in the surface of the object interact with this energy. At this point, the energy from the incident light can interact with the object in a variety of ways. The three most common ways of interaction for lenses include:
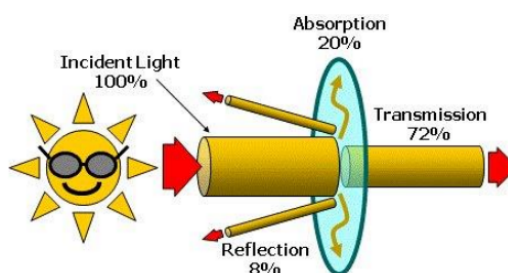
Figure 4   Graphic display of possible interaction of Light when entering a medium

- **Reflection:** Most objects **reflect** some degree of light, redirecting back towards the medium. The amount and colour of light reflected from an object will depend upon the nature of the reflecting material and the angle of the incident light. Reflection can be described with a simple relationship, known as the **law of reflection**, which states that the **angle of incidence** (i) of the incident light is equal to the **angle of reflection** (r) of the reflected light. Mathematically, the law of reflection is given by:

$$i = r \qquad (2.3)$$

  In cases where there are local non-uniformities in the reflecting material, the angle of reflection may deviate. This case of reflection is named scattering. This effect can also occur due to objects that are small relative to the wavelength of light, redirecting it in many directions. When the particles are smaller than the wavelength of light, a phenomenon known as **Rayleigh scattering** occurs. The amount of light scatter produced by Rayleigh scattering is inversely proportional to the wavelength (or colour) of light, so that blue light is typically scattered more than red light.

- **Absorption:** Most objects will **absorb** some degree of light, converting it into heat (or another form of energy). Basically, the incident electromagnetic energy transforms into kinetic energy of the atoms. The **absorptance** of an object describes the fraction of incident light that is absorbed for a given thickness. Very dark or opaque objects have a high absorptance, while relatively clear objects have a low absorptance.

- **Transmission:** Objects that are at least slightly **transparent** will **transmit** some degree of light, allowing it to pass through the material. Basically, the atoms in the surface absorb the energy and pass it along to their adjacent atoms, until the energy is finally released out the other side. The **transmittance** of an object describes the fraction of incident light that is transmitted for a given thickness. Highly transparent objects have a high transmittance, while opaque objects have a low transmittance. In many cases, as the light passes through the object, it is **refracted**, or deviated from its original path.

In other transparent media, including lens materials, waves of light will travel at a slower rate. The velocity of light in a medium will vary as a function of the *refractive index* for that material. The **refractive index (n)** of a transparent medium is essentially a measure of the "optical resistance" of the material to EMR, and is defined as the ratio of the velocity in air compared to the velocity in the material:

$$n = \frac{v_{air}}{v_{medium}} \qquad (2.4)$$

Except for air, which has a refractive index of 1, the refractive index of most substances is *greater* than 1 (n > 1). The *higher* the refractive index of a lens material, the *slower* the light travel through it. In reality, the refractive index of any material varies slightly as a function of the wavelength. This means that various colours of light will each actually have a slightly different refractive in the same lens material. This phenomenon is responsible for **chromatic dispersion**, or the breaking up of white light into its component colours by prisms and lenses. Blue light, which has a higher refractive index than red light, is **refracted** more than red. Chromatic dispersion is a result of the fact that colours of light with *shorter* wavelengths, like blue, travel more *slowly* through most transparent materials than colours with *longer* wavelengths, like red. Therefore, blue light generally has a *higher* refractive index than red light.
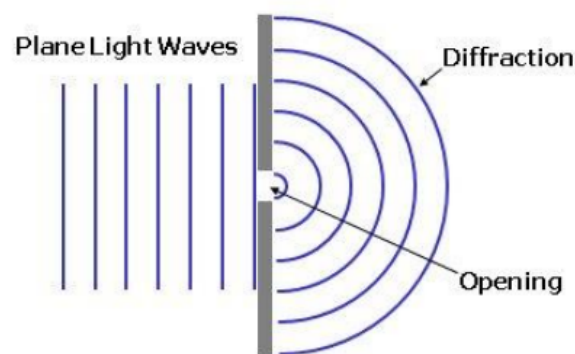
Figure 5 Propagation of diffraction light passing through a small opening

Although less relevant to spectacle lenses, light can also interact with objects—particularly small objects—in other ways due to its wave-like behaviour. Light can be **diffracted**, which is the subtle spreading (or bending) of light at the edge of an object or opening, particularly when the opening is small relative to the wavelength of light. Essentially, light waves reaching the edges of the opening act as new point sources for light waves continuing beyond the opening, allowing these waves to spread out as if they originated from the opening, itself.

Waves of light that reach the same place at the same time can also combine to form a new wave pattern without permanently disrupting each other, a phenomenon known as **interference**. When the *peak* of one light wave combines with the *peak* of another, their amplitudes add to reinforce each other, resulting in *inphase* or **constructive interference**. When the *peak* of one light wave combines with the *trough* of another wave, the amplitudes of these two waves subtract to cancel each other out, resulting in *out-of-phase* or **destructive interference**. *Antireflection coatings* rely on this phenomenon to reduce reflections by employing an optically thin layer of material that causes two separate waves to combine with each other after one wave has been offset in space from the other wave by one- wavelength. This causes the peaks of the first wave to align with the troughs of the second wave, resulting in *destructive* interference, cancelling the amplitude of the reflected light.
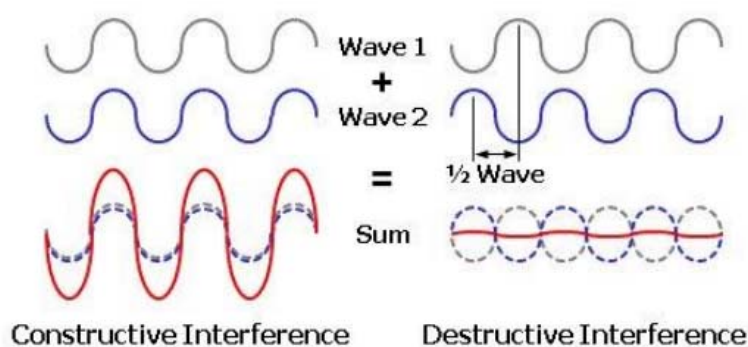
Figure 6 Graphic representation of Interference between two waves

2.4 Fluorescence – Phosphorescence

According to the quantum theory, the energy levels in atoms and molecules are quantized. If the energy of the incident photon matches the gap between to energy levels in the molecule, it can be absorbed, otherwise it will pass through without interacting and the molecule will be transparent to that radiation. When photon is absorbed, the transitions between the specific energy levels can be divided into high energy electronic transitions (UV and VIS regions) and low energy vibrational or rotational transitions (NIR and IR regions).
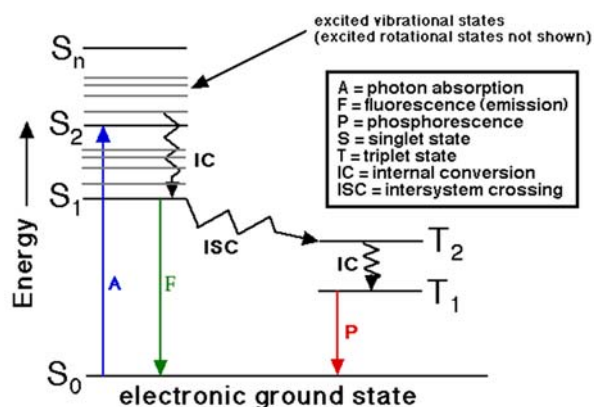
Figure 7 Jablonski Diagram. Energy levels and the possible pathways following light absorption by an absorbing molecule (Chromophore).

As it is shown in Jablonski diagram, Figure 7, after the absorption of a photon and the subsequent excitation to the higher energy level (S0 --> Sn), the molecule relaxes down to the lowest excited energy level; then relaxation from the lowest excited state to the ground state may happen through different processes. If the spin state of the initial and the final energy levels be the same (S1 --> S0), the relaxation is called fluorescence. If the spin state of the initial and the final energy levels are different (T1 --> S0), the relaxation is called phosphorescence. Fluorescence and phosphorescence are radiative processes. Transitions between the same spin states are called internal conversion (IC), while such transitions between different spin states are called intersystem crossing (ISC). Usually the stable ground state in most molecules is the single state (S0 in Figure 7), while the triplet states (T1, 2 in Figure 7) are unstable excited states with an increased internal energy. Oxygen is one of the rare molecules for which the lowest triplet state is the ground state. Excited molecular oxygen is in the singlet state. This is important in the photodynamical reaction occurring during photodynamic therapy (PDT) [10]. There is another type of photon-electron transition called stimulated emission, which happens in atoms. When an atom or molecule is already in an excited state, then an incoming photon with quantum energy equal to the excess internal energy of that atom or molecule, can produce a second photon of the same energy by stimulating the atom or molecule to fall down to its lower energy state. This is the principle of the light amplification that occurs in lasers (Light Amplification by Stimulated Emission of Radiation). Photons produced by stimulated emission have the same phase and frequency, resulting in very intense and coherent light (laser).

2.5 Light Tissue interaction

The effects of EMR upon biological systems (and also many other chemical systems, under standard conditions) depends both upon the radiation's power and frequency. For lower frequencies of EMR up to those of visible light (i.e., radio, microwave, infrared), the damage done to cells and many ordinary materials, under such conditions, is determined mainly by heating effects, and thus by the radiation power. By contrast, for higher frequency radiations at ultraviolet frequencies and above (i.e. X-rays and gamma rays) the damage to chemical materials and living cells by EMR is far larger than that done by simple heating, due to the ability of single photons in such high frequency EMR to damage individual molecules chemically.

2.5.1 Tissue optics

As it was described in Subchapter 2.3 light may interact with matter, and consequently with tissue, in one of the following cases (Figure 8):

a) **Absorption**: specific molecules in the tissue, known as chromophores, absorb the optical energy of the photons and convert it into other forms,

b) **Reflection**: the light beam bounces off the surface with no transmission or possibly no interaction,

c) **Transmission**: the light beam can pass through superficial tissues to interact with deeper areas. Due to the difference of the refractive index of intra and extracellular space the path of light deviates in a certain angle.

d) **Scattering**: once the light beam enters the target tissue it will scatter in various directions, since the various molecules and parts of the cell act as local non-uniformities.
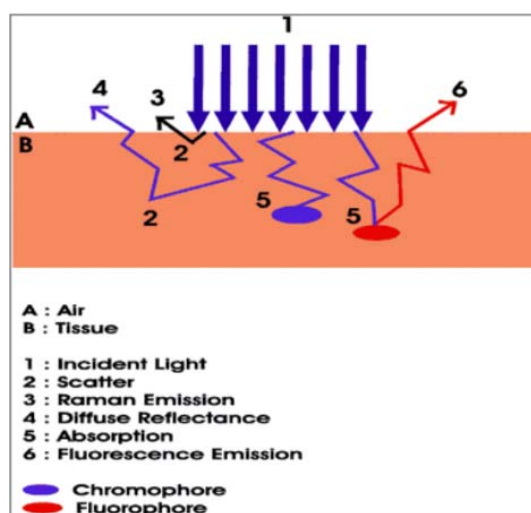
Figure 8   Mechanisms involved in light and tissue interaction

Additionally, various interaction mechanisms between light and tissue are identified in the following major categories that lead to alterations of the tissue structure or composition:

a) ***Photochemical***: absorption of light by molecules present in or added to tissue (basis for Photodynamic Therapy - PDT),

b) ***Thermal***: biological effects due to deposition of thermal energy in tissue (basis for in laser surgery),

c) ***Photoablative***: in the ultra violet (UV) wavelength range photons possess sufficient energy to cause photo –dissociation of biopolymers and subsequent desorption of the fragments (basis for sterilization/ purification processes),

d) ***Electromechanical***: occurs at very high fluence rates where dielectric breakdown of tissue is induced which can lead to the formation of plasma. The rapid expansion of such plasma generates a shock wave which can rupture the tissue.

2.5.2 Optical properties of human tissues

In general, light propagation in biological tissues is affected by three light matter interaction processes: refraction, scattering and absorption, defined in by refraction index (n), scattering coefficient (μ_s) and absorption coefficient (μ_a), respectively [11]. These are treated as fingerprints in biological optics. Scattering occurs due to fluctuations in refractive index of media, whether those fluctuations manifest due to discrete particles or more continuous variations. In biomedical optics, scattering provides feedback during screening and therapeutic procedures. It depends on the structural characteristics of a tissue, e.g., the density of lipid membranes in the cells, the size of nuclei, the presence of collagen fibres, the status of hydration in the tissue, etc. [12]. Due to continuous scattering of light, it is possible for light to propagate back towards the direction of the light source. In such case the phenomenon is referred to as backscattering and novel technologies take advantage of such imaging potentials for extracting information on the physiology of the tissue. Of equal screening and therapeutic value is also the occurring tissue absorption of photos, which is the primary event allowing a laser or other light source to effect tissue. Without absorption, there is no energy transfer to the tissue and it is left unaffected by the light. It also provides a diagnostic role, as well. It can provide a clue to the chemical composition of tissue, and serve as a mechanism towards optical contrast during imaging [12]. While absorption coefficient (μ_a) provides information on the concentration of various chromophores [13], the scattering properties provide information on form, size, and concentration of the scattering components in the medium [14, 15].

2.6 Spectral Imaging

With the fluctuation of modern demands for novel technological gadgets addressed to the average consumer, specifically with the innovations in smartphone technologies, there have been major advances in the field of optical imaging. Colour imaging (CI) systems are able for high resolution and frame rate imaging 3D or 2D video and image capture, with minimal equipment size, at low costs. These systems imitate the function of human vision in order to reproduce the scene as it was perceived by human eyes. Silicon based photosensitive sensors are employed and usually in combination with specially coated lenses are employed to record either two- (Monochrome) or three- (most commonly RGB) dimensional data where each of the three dimensions represents the spatial intensity and chrominance of light.

Spectroscopy is the study of the interaction between matter and EMR depending on the given wavelength. Spectral Imaging (SI) is the application of spectroscopy to each and every pixel of a sensor, in order to record information on the spectrum on each pixel, thusly combining spatial and spectral data.

Each image captured corresponds to a different wavelength and each pixel holds spatial information of a given target. The stack of images acquired by a SI system is known as spectral cube (Figure 9), and the data is represented in multiple dimensions, spanning spatial and spectral information (x, y, λ).
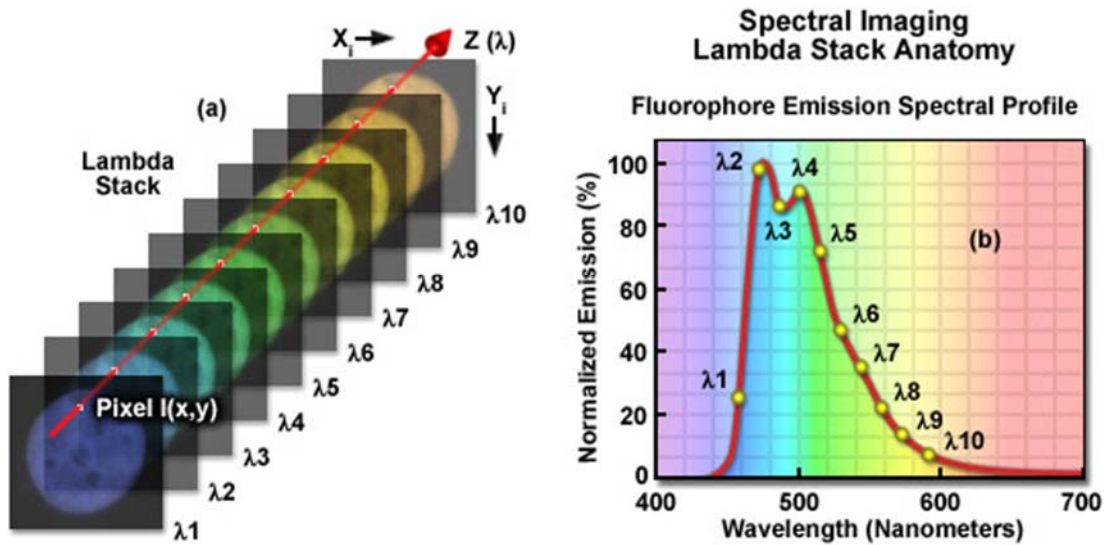
Figure 9 Graphical Representation of a Spectral Cube. On the left each dimension of the cube is represented. On the right a single pixel is presented

21

The distinct variations in the EMR-matter interaction according to the given molecules with respect to wavelengths is called as spectral signature. More specifically, for a given material, the amount of radiation reflected, absorbed or transmitted varies with wavelength. Technically it can be observed as a collection of pixels of the same spatial information observed by exposure on different wavelength. Observing and classification of spectral signatures has application in various fields of science from astronomy, where the chemical composition of a star can be identified by the reflected spectrum, to biomedicine.

Human vision and consequently CI systems that emulate human vision, integrates portions of the light to its photoreceptors, thusly hiding shuttle spectral differentiations necessary for identifying and classifying these spectral signatures. On the other hand, SI can provide a more objective identifier and thusly a more accurate classifier. Despite SI advantages, they remain inaccessible for many applications due to high cost, increased size. Lack of acquisition or computational temporal complexity has made it challenging for observation of dynamically developing phenomena, yet recent innovations have opened the path for such application, by development of real-time snapshot spectral images.

There are two main techniques a spectral cube can be acquired, depending on the purpose and needs of the intended application. That is by scanning with different methods the spectral response of a target or by a single sensor exposure and employment of spectral estimation techniques.
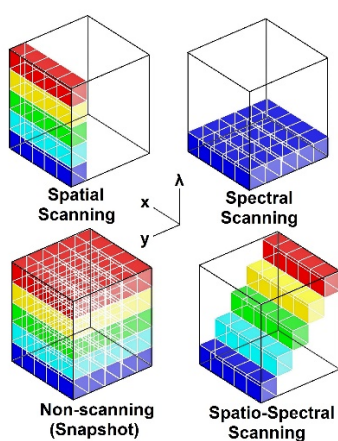
Figure 10 Graphical representation of pixel sequence acquisition of spectral imaging devices

- **Scanning SI.** Scanning devices usually consist of an imaging sensor and interchanging optics and, regardless of the methodology employed, have time consuming cube acquisition and post-acquisition process, spanning minutes. This renders scanning systems inappropriate for radically moving targets, such as live tissue, or dynamic phenomena, such as molecular imaging. Moreover, due to existence of narrow spectral optics used, there is low light throughput. There are three main methodologies for scanning SI.
    - *Spatial scanning.* In spatial scanning, in each sensor exposure a full spectrum of a given pixel line is captured. Hyperspectral imaging (HSI) devices designed for spatial scanning obtain data by projecting a portion of the target onto a slit and dispersing the slit image with a prism or a grating. This leads to having the image analysed per lines and integration of opto-mechanical parts. These line-scan systems, is based on synchronised movement between the imaging system and the target, by moving either or both. Therefore, line-scan systems are particularly common in remote sensing and to imaging materials moving upon a conveyor belt. A special case of line scanning is *point scanning*, where a point-like aperture is used instead of a slit, and the sensor is essentially one-dimensional instead of 2-D, as for example on a of the shelve spectrometer.
    - *Spectral scanning.* In spectral scanning, each sensor exposure represents the spectral response at a single wavelength or an integration of a portion of the EMR depending on the optical bandpass filter at use, either tuneable. HSI devices for spectral scanning are typically based on optical band-pass filters, either tuneable or fixed. The cube is acquired by exchanging filters, for instance with the use of a filter wheel, the imaging system and the target are stationary. In such setup, spectral smearing and spatial blurring can occur if there is movement within the scene, invalidating spectral and spatial correlation/detection. On the other hand, there is the advantage of being able to target spectral bands of interest with specific filters, as well as having a direct representation of the two spatial dimensions of the scene.
    - *Spatiospectral scanning.* In spatiospectral scanning, in each sensor exposure a spatial portion of it corresponds to a different wavelength. This technique was introduced in 2014 and the imaging system consists of an imaging device at a *non-zero* distance behind a slit, while the slit lies between two dispersive elements. Scanning is achieved by movement of the whole imaging system, by moving only the camera, or by just moving the slit. This technique attempts to unite spatial and spectral scanning in order to exploit advantages of each methodologies so as to alleviating some of their disadvantages.

- **Non-scanning or snapshot.** In non-scanning techniques, a single sensor exposure contains information to reproduce full spatial and spectral data, by employing spectral estimation techniques or sacrifices spatial information for simultaneous multispectral acquisition. These techniques shorter acquisition times, yet they have higher post-processing time and computational effort as well as higher economic cost, due to the increased complexity and sophistication of the optomechanical system in use, and often lower light throughput due to use of multiple optics. This approach includes:
    - *The HyperPixel Array imager*, where an optical processor is employed in order to serialize the spatial information and record it to a spectrometer and then digitally decode it [16].
    - *The multiaperture spectral filter approach*, where a sensor is divided and in each portion a lens with a dedicated bandpass filter is coupled representing a single part of EMR [17]
    - *A coded aperture snapshot spectral imager*, a compressive-sensing–based approach using a coded aperture. Standard imaging lens is used to form an image of a remote scene in the plane of the coded aperture modulating the s8patial information over all wavelengths of interest with the coded pattern [18].
    - *A microfaceted-mirror-based approach*, where an image slicer is employed. By taking advantage of the reflection angle, which varies according to wavelength, and expand the reflected beam, different wavelengths with the same spatial profile are recorded on different portions of the sensor [18].
    - *A generalization of the Lyot filter*, which projects different wavelengths upon different portions of the sensor by the use of a birefringent spectral de-multiplexor [19].
    - *A non-Bayer sensor approach*, where different portions of the sensor are covered with different bandpass filters instead of the classically RGB filter approach [20]. Ximea LTD launched a commercial camera with such approach in 2015, yet still the price range is over 12.500 euros.
    - Multiple sensor simultaneous full frame capturing of a small yet adequate number of narrow bands via beam splitting optomechanical parts [21].

Most non-scanning approaches suffice to the multiple spectral bands acquired in imaging. Recent approaches attempt to interpolate intermediate spectral bands by estimating missing data. This attempts allow acquiring missing information by taking advantage of a priori data and is promising in providing full spectra that do not exhibit sparks but smooth changes between bands.

2.6.1 MUSIS Hyper Spectral Camera

Figure 11 MuSIS HS Camera

MUSIS is a hyperspectral scanning system capable of spectral imaging (both reflectance and fluorescence) with high spectral resolution and high throughput ratio, D. Anglos et al [22], C. Balas [[23], developed an electronically tunable narrow band pass optical scanner. Displacement of the optical elements of the latter, results in the tuning of the imaging wavelength, which is performed with the aid of electromechanical manipulators controlled from the PC via microcontroller. MuSIS HS' **Error! eference source not found.** technical features are:

- Spectral imaging acquisition of 5nm full width half maximum (FWHM), performing in 34 spectral bands of about 20nm each, in the spectral range 360nm (Ultraviolet)–1000nm (Near Infrared).

- Real time capturing & displaying images with an analysis of 1600x1200 pixels.

- Minimum transmittance is 40% across its operational spectral range.

- Tuning spectral range of the filtering system is matched with the responsivity spectral range of the charge coupled device (CCD) image sensor, with the capability of extending to longer wavelengths, up to the mid-infrared range (photocathode).

- A megapixel CCD camera, for feeding back the single band signal, based on the IEEE-1394 data transferring protocol, capable of acquiring images at a rate of 15 frames/s at full resolution and of more than 30 frames/sat VGA resolution.

- A special calibration procedure [24] is executed before any imaging procedures, compensating for the wavelength dependence of the response towards the electro optical parts of the system and the given light source.

- Operating in imaging mode, an image at each wavelength band is acquired while, in spectroscopy mode, a fully resolved diffuse reflectance and/or fluorescence spectrum per image pixel can be recorded (image spectral cube). The combination of spectral and color imaging with calibration enables the system to operate as either Imaging Spectrometer or Imaging Colorimeter.

2.6.2 Spectral Estimation

Although the aforementioned snapshot imaging techniques allow instant capturing of multiple bands, it is still a small fraction of the entire of the spectrum. Therefore, Spectral Estimation (SE) algorithms are usually employed in order to accurately interpolate the missing bands. This leads to project low dimensionality data, such as 3 or 10 bands cubes, to higher dimensionality. Ultimately, this allows for snapshot imaging to lead to acquisition of data equivalent to a scanning device at shorter acquisition times, thusly combining speed and higher spectral resolution. SE is subjected to a number of limitations. These include

- Long post processing times in order to interpolate correctly the missing bands or register the sensor acquired bands.
- A trade-off between spatial and spectral resolution is a given, in single sensor approaches, since portions of the sensor are assigned to a single band.
- Image distortions
- Poor light throughput
- Spectral entanglement of information between the channels of the RGB sensor.

Many method have with high accuracy estimation have been proposed. Such methods include Wiener estimation, R matrix, Linear Projection and interpolation. Most popular algorithms for spectral estimation are Wiener Estimation, Fast Fourier Transform, Principal Component Analysis, Wavelets, Singular Value Decomposition, Hilbert Transform and Discrete Cosine Transform. Moreover, it is common to use a priori knowledge of a reference sample.

2.6.3 Real Time Spectral Mapper

Based on the last aforementioned approach, in Epitropou et al [25] a novel real-time multispectral imaging system that can simultaneously acquire six spectral bands and provide spectral information in any desired wavelength within the visible spectrum, via spectral estimation, was presented. The approach focus on two sensor simultaneously capturing 6 narrow bands by mirroring the target on two RGB sensors and coupling each with a different multibandpass filter, each complementary towards the other as far as the visible spectrum is concerned. The acquired bands are then correlated with a priori knowledge and a higher dimensionality cube is estimated. This approach yields the advantage of shorter post processing times since no registration or post acquisition correction algorithms are required other the chosen SE. Moreover, the optical parts are kept to a minimum, allowing sufficient light throughput. The overall system presented is constructed a compact complete system that incorporates off the shelf optomechanical products, providing a reduced cost approach than the rest of the snapshot spectral imaging solutions. On the other hand, this approach suffers from substantial overlapping between the RGB primary filters transmission characteristics and the three bands projected upon the sensor, thusly a given set of bands is transmitted by more than one of the primary filters and at different amounts.

Spectral fidelity of this system is further investigated and refined by investigating this spectral overlapping and proposing and approach to accurately deconvolve the recorded response.

3. Spectral Deconvolution and Channel Cross-talk

During the acquisition of a spectral image of a target, there are several factors contributing to the acquired result, from the light source to the selected sensor and optics. In order to accurately receive the spectrum of the target without interference from outside factors, it is imperative to understand the contribution to the result by each factor.

3.1 Multi band pass filters

Multi band pass filters (MBPF), are coated optics that transmit light in several discrete narrow spectral bands, while absorbing or reflecting the complementary bands, depending on the coating used. They are widely used in fluorescence imaging in order to rapidly identify samples, by cutting off excitation and transmitting emission spectra. The filters are optimised to provide high transmission, steep edges and deep blocking for balance in contrast, brightness, and colour representation.

3.2 Chip Colour Camera

In a simplistic approach, one could argue that a photosensitive chip converts photons into electrons. The number of electrons is proportional to the number of photons. The camera electronics are colour blind, meaning that the sensor cannot distinct the wavelength of the incident photon yet it produces an electron as long as the corresponding wavelength is within the sensor sensitivity range. Spectral camera sensitivity is regulated by optical coating filters coupled with the sensor, known as colour filter arrays (CFA) or colour filter mosaic (CFM). Each pixel is assigned to a different and unique colour channel. In order for the sensor to retain full spatial information, the missing pixel values for the remaining two colour channels are interpolated, usually by bilinear interpolation. The overall spectral sensitivity of the sensor is equal to the product of the responsivity of the sensor and the transmission of the filter.

More specifically, the CFA filter the light according to the incident wavelength, so as each pixel include spectral information correlated to spatial coordinates. For example, the Bayer filter (Figure 12), which is most commonly used, gives information about the intensity of light in red, green, and blue wavelength regions. The raw image data of a single sensor consist of intensity corresponding to the spectral sensitivity of the filter at each pixel, providing raw data for a single sensor colour channel. A full colour image, with intensities at all three primary colours, is interpolated with by use of a demosaicing algorithm custom for each type of CFA in order to incorporate spectral and spatial information. The spectral transmittance of the CFA elements in junction with the demosaicing algorithm determine the colour rendered for the full frame. The spectral sensitivity and corresponding quantum efficiency of both the sensor and the CFA are typically wider than the visible spectrum, thusly all visible colours can be reproduce. The recorded electrical voltage values per pixel is then translated to a CIE colour matching function.
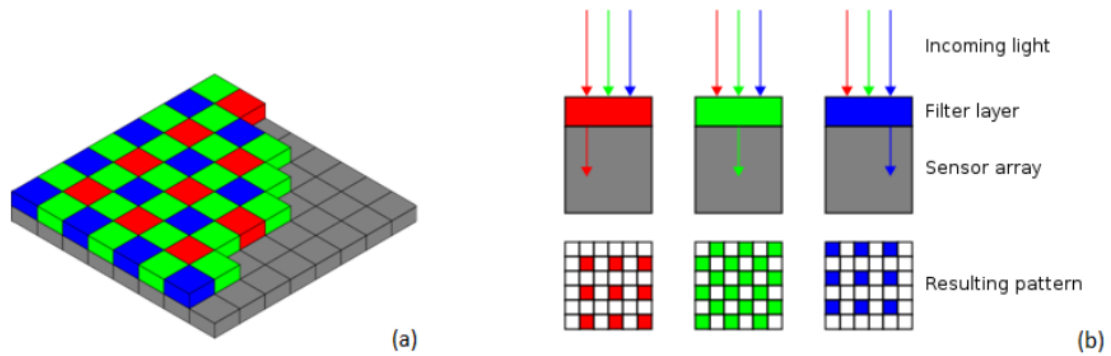
Figure 12 A) The Bayer Colour Filter Mosaic. B) The filter mosaic per channel and its interaction with light

Each CFA approach has a different relative spectral response, depending on the coating of the optical filters that are used and modify the per pixel spectral response of the camera, with Bayer colour filter being the most commonly used. Other filters are presented in Table 1.

Table 1 Commonly used Filter Arrays

Pattern	Name	Description	Pattern size (pixels)
	Bayer filter	Very common RGB filter. With one blue, one red, and two green.	2×2
	RGBE filter	Bayer-like with one of the green filters modified to "emerald"; used in a few Sony cameras.	2×2
	CYYM filter	One cyan, two yellow, and one magenta; used in a few cameras of Kodak	2×2
	CYGM filter	One cyan, one yellow, one green, and one magenta; used in a few cameras.	2×2
	RGBW Bayer	Traditional RGBW similar to Bayer and RGBE patterns.	2×2
	RGBW #1	Three example RGBW filters from Kodak, with 50% white.	4×4
	RGBW #2		
	RGBW #3		2×4

28

The acquired spectral response of a target is the summation of interactions between light and matter from the emission of the source to the recording of the sensor. The response is the product of the spectral profile of the light source that interacts with the spectral characteristics of the target. The reflected or transmitted light from the target is then filtered by the optics of the recording system, whether they are MBPF or the CFA of the sensor, before it is recorded upon the sensor. Therefore, is paramount the imaging system to be calibrated in correspondence to the light source so the spectral signature of the target can be deducted without being corrupted by the spectral sensitivity of the imaging system or the spectral profile of the light source.
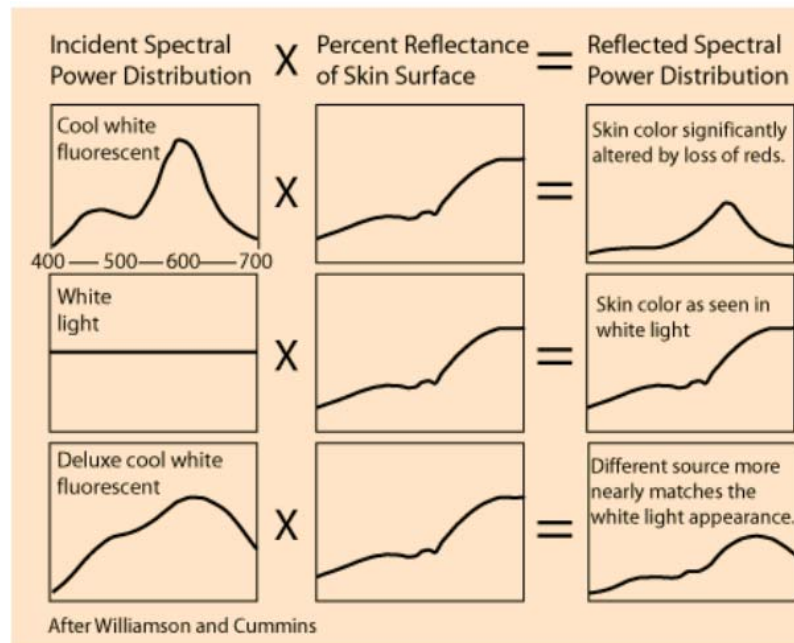
Figure 13 Influence of different light sources to the perceived spectrum of skin.

3.3 Cross-talk phenomenon

Any given optical sensor used in imaging of the visible spectrum, is manufactured according to the spectral specifications defined by human vision. This means that a camera attempts to imitate the capabilities of human vision in regards to colour perception and spectral overlapping. By allowing all channels to have sensitivity to all wavelengths of the visible spectrum, yet with various degrees of said sensitivity, a colour blending is achieved imitating the colour perception of human eyes. In Figure 14, the relative sensitivity of the human photoreceptors as well as that of a given senor is presented one next to the other, where the spectral overlapping of the three primary colours is evident.
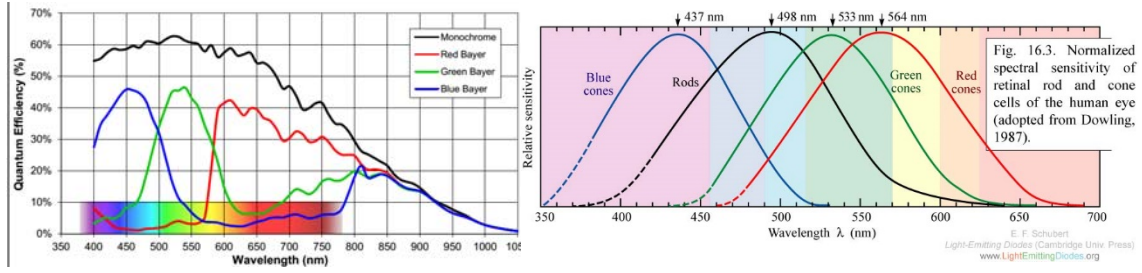
Figure 14 On the left the sensitivity of a sensor as presented by the manufacturer. On the right the relative sensitivity of the human photoreceptors. The overlapping in both systems works towards allowing the capturing of the same gamut of colours

Hirakawa [26] analysed the cross-talk phenomenon as coding of chrominance data embedded in the measurements of the sensor. Optical diffraction and minority carriers are identified as the predominant causes of this phenomenon that contaminates the data recorded by the sensor. Optical diffraction occurs where photons are forced to stray away from the centre of the pixel when there is high incident angle of light. Minority carrier deterioration occurs when electrons stray from the target when the charge is collected. The contamination occurring by this phenomenon is aggravated by the miniaturisation of the pixels leading to the decreased distance between neighbouring pixels. The most noticeable effect is the desaturation of colour, mainly due to the combining neighbouring pixel measurements with different spectral sensitivity via the demosaicing algorithm. The author comments that although the research focuses on the physical aspects of the phenomenon, existing deconvolution or image deblurring methods do not suffice due to the complexity of the sensor data and then proceeds to a spatio-spectral sampling approach to analyse the mechanism underlying the cross-talk phenomenon. Lastly, a method is proposed to correct this contamination by a pixel-wise inverse matrix operation, supported by numerical experiments.

3.4   Channel cleansing

The sensitivity of a given pixel of a Bayer tiled sensor depends on photosensitive materials of the pixel and the given RGB micro filter coupled with the said pixel. This allows a broad sensitivity range over the visible spectrum. When coupled with a bandpass filter, this range is modified accordingly. If the filter is a multi-bandpass filter (MBPF), this leads each pixel to be unevenly sensitive to any of the three narrow spectral bands. This thesis, aims on application of triple multi-bandpass filters coupled with standardised RGB silicon based sensor. The bandpass filters are simulated with the use of off-the-shelf LEDs with narrow spectral emission.

A channel though it exhibits a dominant broad sensitivity peak over the corresponding EMR spectrum, it retains a low sensitivity over the rest of the visible spectrum, partially due to the cross-talk phenomenon as well as sensitivity leak of the CFA filters. Assuming that the spectral bands of the MBPF are located in the red (R), green (G) and blue (B) channel sensitivity areas of the optical sensor and that R_{Broad}, is the collective response value of the R channel, then R_{Narrow}, R_{Green} and R_{Blue}, will be the R channel values recorded at the red, green and blue band of the MBPF. Making the same assumptions for the G and B channels, then:

$$R_{Broad} = R_{Narrow} + R_{Green} + R_{Blue}$$
$$G_{Broad} = G_{Red} + G_{Narrow} + G_{Blue} \qquad (3.1)$$
$$B_{Broad} = B_{Red} + B_{Green} + B_{narrow}$$

It is therefore essential to disentangle the recorded spectral information for recovering the narrow spectral images, whose spectral content corresponds to the spectrum of the MBPF coupled with the Bayer tile filter. Due to this fact, an inverse matrix unmixing algorithm that

can deconvolve the spectral information and eliminate the crosstalking of the channels in each band of the MBPF, is employed.

By considering each broad channel response as a percentage of each individual variable for each equation in the system 3.1, the system advances as following

$$R_{Broad} = w_{RR} * R_{Narrow} + w_{RG} * G_{Narrow} + w_{RB} * B_{narrow}$$
$$G_{Broad} = w_{GR} * R_{Narrow} + w_{GG} * G_{Narrow} + w_{GB} * B_{narrow} =>$$
$$B_{Broad} = w_{BR} * R_{Narrow} + w_{BG} * G_{Narrow} + w_{BB} * B_{narrow}$$

$$\begin{bmatrix} R_{Broad} \\ G_{Broad} \\ B_{Broad} \end{bmatrix} = \begin{bmatrix} w_{RR} & w_{RG} & w_{RB} \\ w_{GR} & w_{GG} & w_{GB} \\ w_{BR} & w_{BG} & w_{BB} \end{bmatrix} * \begin{bmatrix} R_{Narrow} \\ G_{Narrow} \\ B_{Narrow} \end{bmatrix} = W * \begin{bmatrix} R_{Narrow} \\ G_{Narrow} \\ B_{Narrow} \end{bmatrix} \qquad (3.2)$$

Where,

- W is the weight matrix,
- R_{Broad}, G_{Broad}, B_{Broad} are the intensity of the light as recorded by a colour sensor
- R_{Narrow}, G_{Narrow}, B_{Narrow} are the actual spectral band light intensities, before light reaches the surface of the sensor.

Since "broad" signals are known and W matrix can be calculated as it is described in equation (3.2), then spectral intensities of the narrow band signals can be calculated by a matrix inversion. Furthermore, the W matrix is refines as to include information in order to deconvolve the spectral information filter by the MPBF ad well as to remove the contamination from the cross-talk phenomenon and the CFA spectral leak of coating.

Solving towards the narrow response free of crosstalking:

$$\begin{bmatrix} R_{Narrow} \\ G_{Narrow} \\ B_{Narrow} \end{bmatrix} = W^{-1} * \begin{bmatrix} R_{Broad} \\ G_{Broad} \\ B_{Broad} \end{bmatrix} \qquad (3.3)$$

This process enables the concurrent acquisition of any three spectral bands, by using a triple MBPF (TBPF) and an ordinary color camera with high spectral fidelity. This approach may be expanded to the concurrent capturing of four spectral bands, by using color cameras with four channels response and quadruple MBPFs. Also, with the use of optical dispersing elements, more than one camera can be used, to increase the number of the acquired spectral bands to six, allowing for sufficient single capture information fed to spectral estimation algorithms, leading to real time spectral imaging, as described in [25].

3.5   Channel Cleansing based on experimental measurements

In order to remove the cross-talking between the camera channels, the camera spectral sensitivity can be used as it is described in [27], and then verified and employed in real time spectral estimation in [28]. Furthermore, based on this approach, in the scope of this thesis different light source as well as sensors with different spectral sensitivity are employed in order to test the robustness and efficiency of the approach.

A perfect sensor is one with such efficiency that converts a single photon into a single electron, and then converts electrons to measured counts. In absence of light there should be no signal. Repetitive exposures to the same stable light source should give the same average signal with a deviation about the average determined only by Poisson statistics. All pixels should have exactly the same characteristics.

These are the optimal specifications of a sensor, yet there is no such device in practice. However, modern imaging detectors come very close, in quality and efficiency. The most important properties of a photon detector by which they are characterised and compared are:

- *Quantum efficiency:* the ratio of electrons produced towards the number of incident photons
- *Noise:* the irreducible electronic fluctuations in the output signal from an imaging device
- *Dynamic range:* the ratio of the maximum signal the device can detect without saturation towards the noise level
- *Linearity:* the proportionality of the output signal towards photon arrival rate
- *Spectral response:* the portion of the EMR over which the device is sensitive
- *Temporal response:* the time interval over which the device cannot respond to another incoming photon

3.5.1 Measuring the spectral sensitivity of a colour camera manually

Materials and methods

USB3 Vision Cameras

A USB3 Color Vision Camera with low power consumption, high speed, 1600x1200 resolution with 90fps. This CMOS sensor based camera was used as the main camera for the experimental training procedures described in Subchapter 3.5.2.
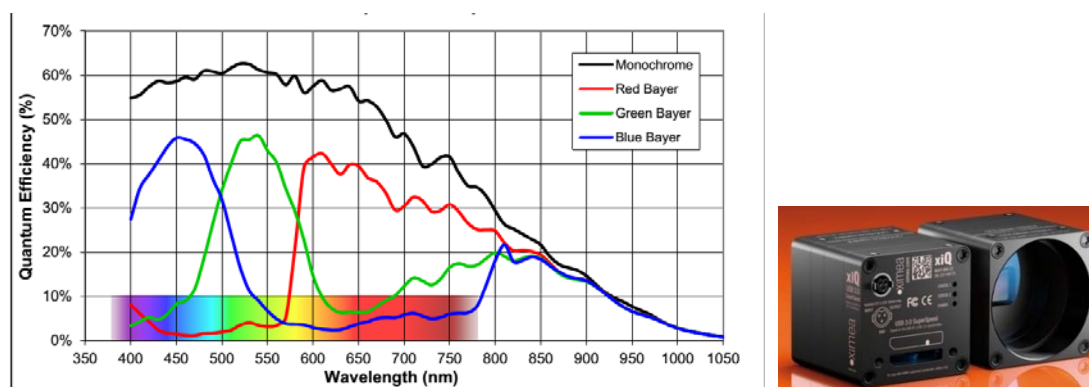
Figure 15 On the right is an image of the USB3 vision camera. On the left the spectral response of the camera of both colour and monochrome versions is given

In order to acquire correct color and multispectral data, calibration of the camera was performed. Using a white target, the camera was white balanced so all three channels (RGB) would have the same value. Shutter and Gain was also adjusted so the images produced would not be saturated.

Table 2 The primary parameters of the sensor

Sensor	EV76C560ACT-EQV
Type	Global shutter, overlap mode
Resolution (pixel)	1280 x 1024
Active area (mm)	6.9 x 55
Sensor diagonal [mm]	8.7
Optical format [inch]	1/1.8
Pixel Size (H × V) [µm]	5.3 × 5.3

Beam splitter

A **beam splitter** is an optical device that splits a beam of EMR in two. In its most common form, a cube, it is made from two triangular glass prisms which are glued together at their base using polyester, epoxy, or urethane-based adhesives. The thickness of the resin layer is adjusted such that (for a certain wavelength) half of the light incident through one "port" is reflected and the other half is transmitted due to frustrated total internal reflection. Polarizing beam splitters, such as the Wollaston prism, use birefringent materials, splitting light into beams of differing polarization.

Table 3 The primary parameters of the beam splitting optics

Figure 166 Image of beam splitting cube optics

Dimensions (mm)	25.0 x 25.0 x 25.0
Dimensional Tolerance (mm)	±0.1
Clear Aperture (%)	>90
Surface Accuracy	λ/8
Surface Quality	40-20
Beam Deviation (arcmin)	±2
Bevel	Protective bevel as needed
Substrate	N-BK7
Transmission (%)	Average: 45
Transmission Tolerance (%)	±5
Absorption (%)	<10
Polarization	<6%
Coating	VIS
Coating Specification	R_{avg} <0.5% @ 430 - 670 nm
Construction	Cube
Wavelength Range (nm)	430 - 670
Type	Non-Polarizing Beamsplitter

LED Tuneable light source

The LED light source used is a custom tuneable led light source, presented firstly in [29]. This light source is capable of providing us electromagnetic radiation which extends from UV to near infrared, using a number of narrow band emission LEDs and propagating their light through optical fibres, one for each one. LEDs are connected to an Arduino, controlling operation and intensity. Other circuits (microcontrollers) are also used for current stabilization, handling etc. The tuneable LED source is energy efficient and has high throughput (85%), stability, low cost and tuneability. Electromagnetic radiation of this source extends from 380 nm (Ultra Violet), to 980 nm (near infrared).
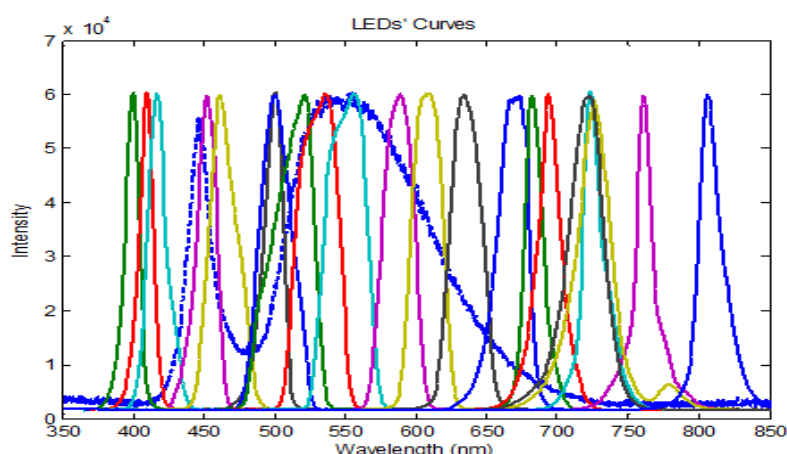
Figure 17 The spectral emission of the Tunable LED light source

Halogen light source

A halogen lamp, is an incandescent lamp that has a small amount of a halogen such as iodine or bromine added. The combination of the halogen gas and the tungsten filament produces a halogen cycle chemical reaction which redeposits evaporated tungsten back onto the filament, increasing its life and maintaining the clarity of the envelope. Because of this, a halogen lamp can be operated at a higher temperature than a standard gas-filled lamp of similar power and operating life, producing light of a higher luminous efficacy and colour temperature. In the experimentations a halogen light source model was used. Before every usage an amount of at least a half hour was allowed in order to allow the operating lamp temperature of operation to be achieved and the emitted spectrum to be stabilised.
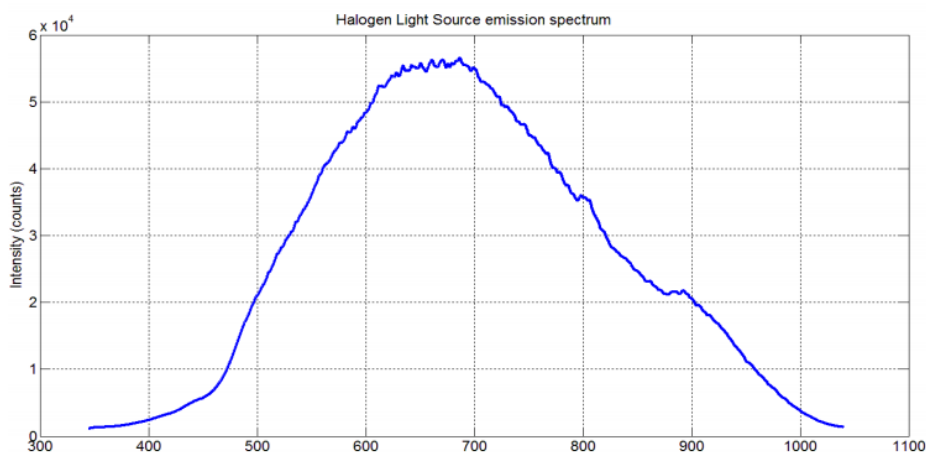
Figure 18 The spectral emission of the Halogen lamp light source

Spectrometer

The spectrometer used is of high spectral resolution. It is a modular spectrometer, easily configured for a wide range of absorbance, reflection and emission applications. The compact unit has a 3648-element CCD array detector with response from 200-1100 nm, an optical bench with on-board electronic shutter and 16-bit A/D resolution with auto nulling feature.
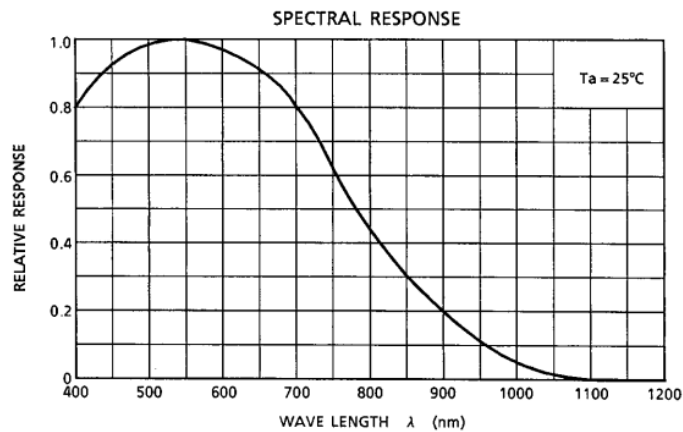
Figure 19 The spectral sensitivity of the sensor used by the spectrometer

Roscolux Films

The Roscolux films are based on one of two types of plastic, co-extruded polycarbonate plastic or deep dyed polyester. The sheets are sized 50 x 61 cm and the rolls: 1.2m x 7.62m

Figure 20 An image of the Roscolux Filter Films

The filters create color by absorbing certain wavelengths and transmitting the rest. Thus, a red filter absorbs blue and green, allowing only the red wavelengths to pass. The process is subtractive, thusly heavily dependent to the spectrum emitted by the light source.

The Rosco swatch book provides detailed information on the spectral energy curve of each filter. The curve describes the wavelengths of color transmitted through each filter.

SENSOR PARAMETERS

As mentioned in Subchapter 3.2, the acquired spectral response of a target is the summation of interactions between light and matter from the emission of the source to the recording of the sensor. In order to retrieve the pure spectral response of a target from spectral imaging, it is paramount to have knowledge at any given measurement of the spectral response of both the light source and the imaging system, so as to remove their interference and isolate the spectral signature of the target. Focusing on the imaging system, an experiment is designed following a very simple in concept and with high accuracy methodology. The relative spectral response of a camera was calculated by stimulating it with very narrow band illumination, of the same intensity at each wavelength, with different light source filtered by a monochromator, an optomechanical device that isolates photons of a very narrow wavelength spectrum through diffraction. Various researchers have investigated methods for characterization which do not use such equipment [30], due to high cost and limited availability, yet still prune to errors.

In contrast to the human eye, silicon based sensors are also sensitive to near infrared light, while the optical gratings used to differentiate the channels manifest similar sensitivity to infrared light (IR). This leads to imaging data spectral contamination, since all channel responses would be altered by IR light. An IR cut filter corrects this situation, by allowing only visible light to be recorded by the sensor. However, cameras without IR cut filter provide more flexibility because they enable the users to apply their own filter depending on the particular requirements. An alternative to this is careful selection of light sources and control over the illumination of the imaging environment. In the scope of this thesis, the measurements are always made under controlled illumination environment and the imaging sensors used are IR cut-off optical filter.

Besides the spectral sensitivity, the final output frame is also determined by operating settings of the imaging sensor. In the following table, basic camera parameters are depicted.

Table 4 Primary parameters influence image quality of a sensor

Parameter	Output frame influence
Shutter	Exposure time of the sensor
Gain	Amplification of the output signal of the sensor
Offset (Brightness)	Increase of the grey/colour levels
Sharpness	Enhances blurred images
Gamma	Manipulation of middle grey/colour levels
Saturation	Adjustment of colour saturation
Hue	Shift colour values
White Balance	Adjust colour channel amplification

3.5.2 Measurements

The relative spectral response of a colour CCD camera was measured using the following experimental setup:

Firstly, a custom multispectral LED light source was coupled to a tunable diffraction grating monochromator, with a minimum tuning step of 0.2nm and 3.4nm FWHM. The camera was focused at the exit slit of the monochromator, in a distance of 40cm. Amongst the camera and the monochromator, a cube beam splitter (25mm, non-polarizing) was mounted, splitting 50% of the monochromatic light to the camera and the other 50% to the spectrometer. In order to secure that on each step of the monochromator the sensor was exposed at an equal volume of photons and at single wavelength. Through this setup, the output light from the monochromator was kept to a constant value by adjusting the output intensity of the LEDs. This process was done for every tuning step, practically 5nm, as the transmittance of the monochromator and the emission spectra of the LED source alter throughout their wavelength active range. The combination of the LEDs, the monochromator and the spectrograph produced a tunable wavelength light source with a flat response between 400 and 700 nm. The same process was followed after a halogen lamp was coupled with the monochromator, in place of the custom multispectral LED light source. The measurements practically were made from 410nm due to lack of insufficient illuminance of both light sources at the blue range of the spectrum. The practical set up of the experiment is shown in Figure 21.
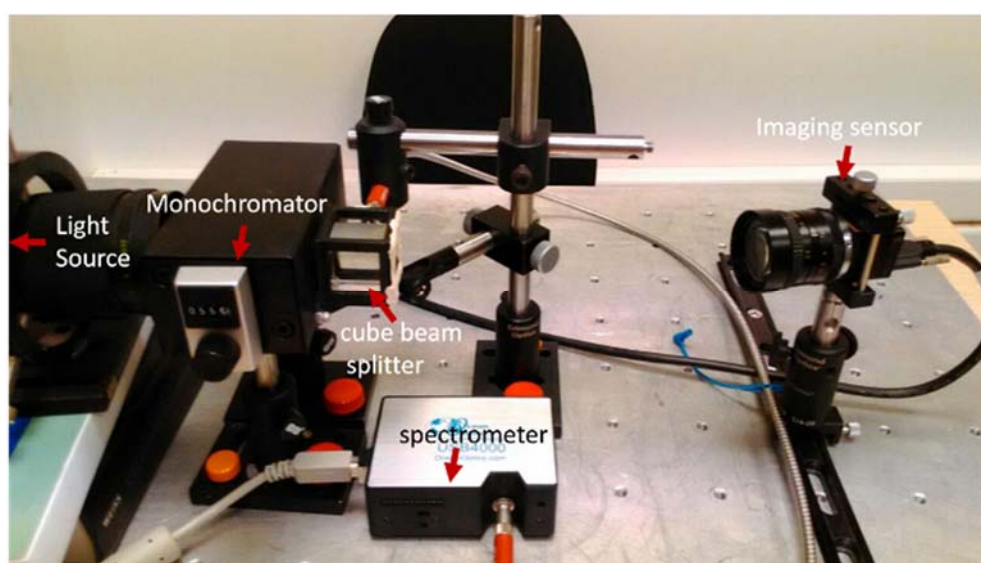
Figure 21 Image from the used experimental setup

In order to assure fidelity of the measurements of the spectrometer, the spectral sensitivity of its sensor, as shown in Figure 19, was taken into account and the light source intensity was adjusted at each step in order to nullify said interference, as show in Figure 22.
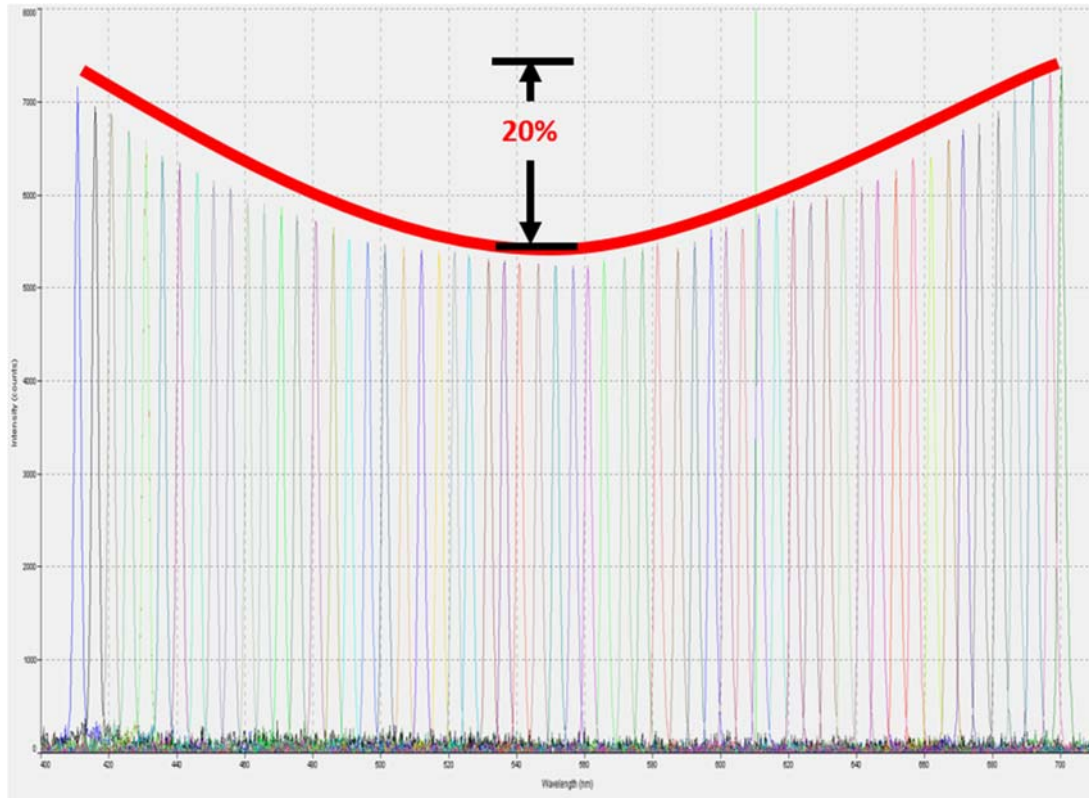
Figure 22 Experimental Spectral Intensity measured by the spectrometer

For a single wavelength exposure, four frames were acquired from the colour sensor. The mean of those frames per pixel was considered spectral response of the sensor for the given wavelength. This step was necessary for removing shot noise. Shot noise is caused by the random arrival of photons, since each photon is an independent event, and in a given time period is governed by a Poisson distribution. With a large enough sample, a graph plotting the arrival of photons will plot the familiar bell curve. Shot noise is most apparent when collecting a relatively small number of photons, as where the lightning conditions during the described measurements.

Moreover, the camera was set with default settings, except for Shutter, Gain and White Balance parameters. Gain was nullified in order to remove effects of analogue amplification. Shutter was set so as the frames would not be saturated or there were a wavelength step of dark frame. The White Balance settings was adjust so as the peak response at the each channels would be equal on their respective expected maximum sensitivity wavelengths, based on the quantum efficiency characteristic curve given by the vendor.
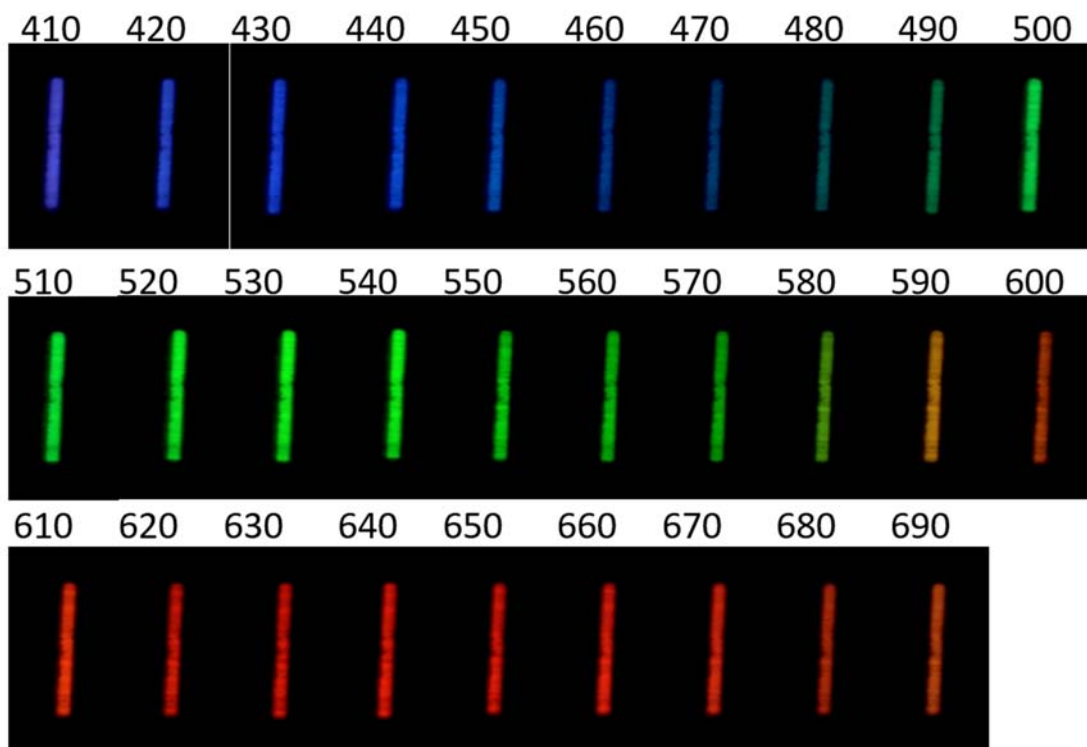
Figure 23 Shot Noise free image stills at each wavelength using LED light source
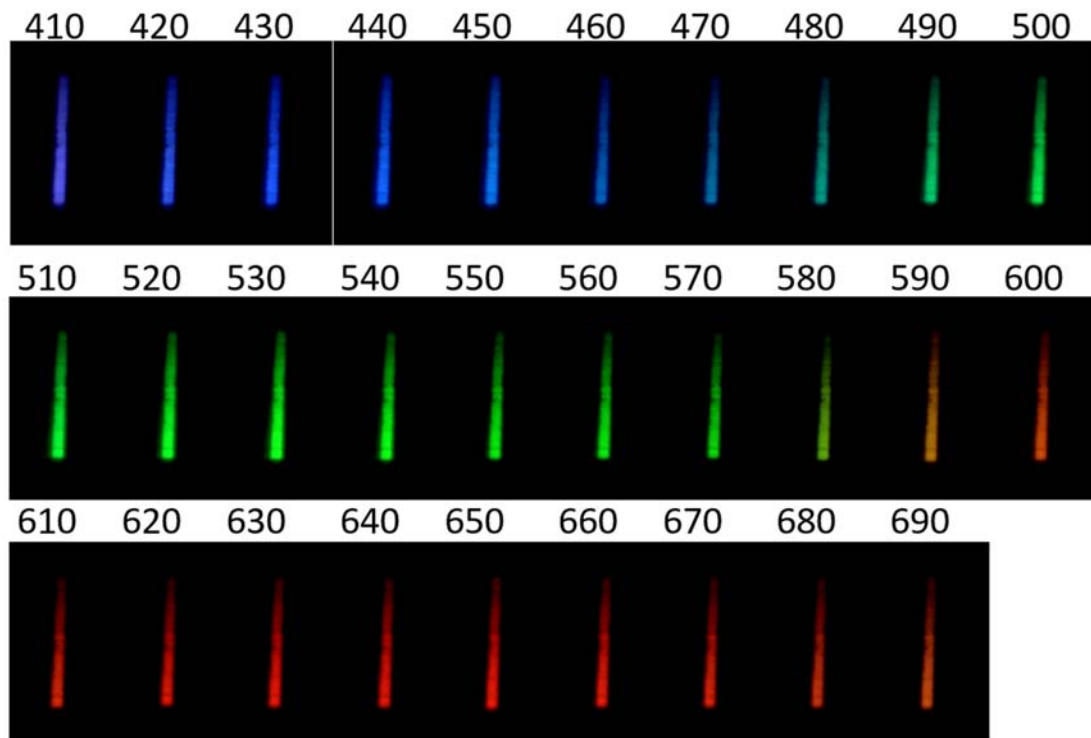
Figure 24 Shot Noise free image stills at each wavelength using Halogen lamp light source

Mean, median and max of a 10x10 pixel area from the center of the image as well as the central pixel spectral response from the pixels per nanometer, as presented in Figure 25, follow the same pattern of response. Central pixel response is chosen, based to the properties of light propagation per nanometer from the light source towards the sensor and light dispersal on micro-optics. This way the effects of stray light and diffraction limit are nullified giving a more accurate ratio.

Spectral Response of the CCD per channel is isolated from the central pixels of the image.
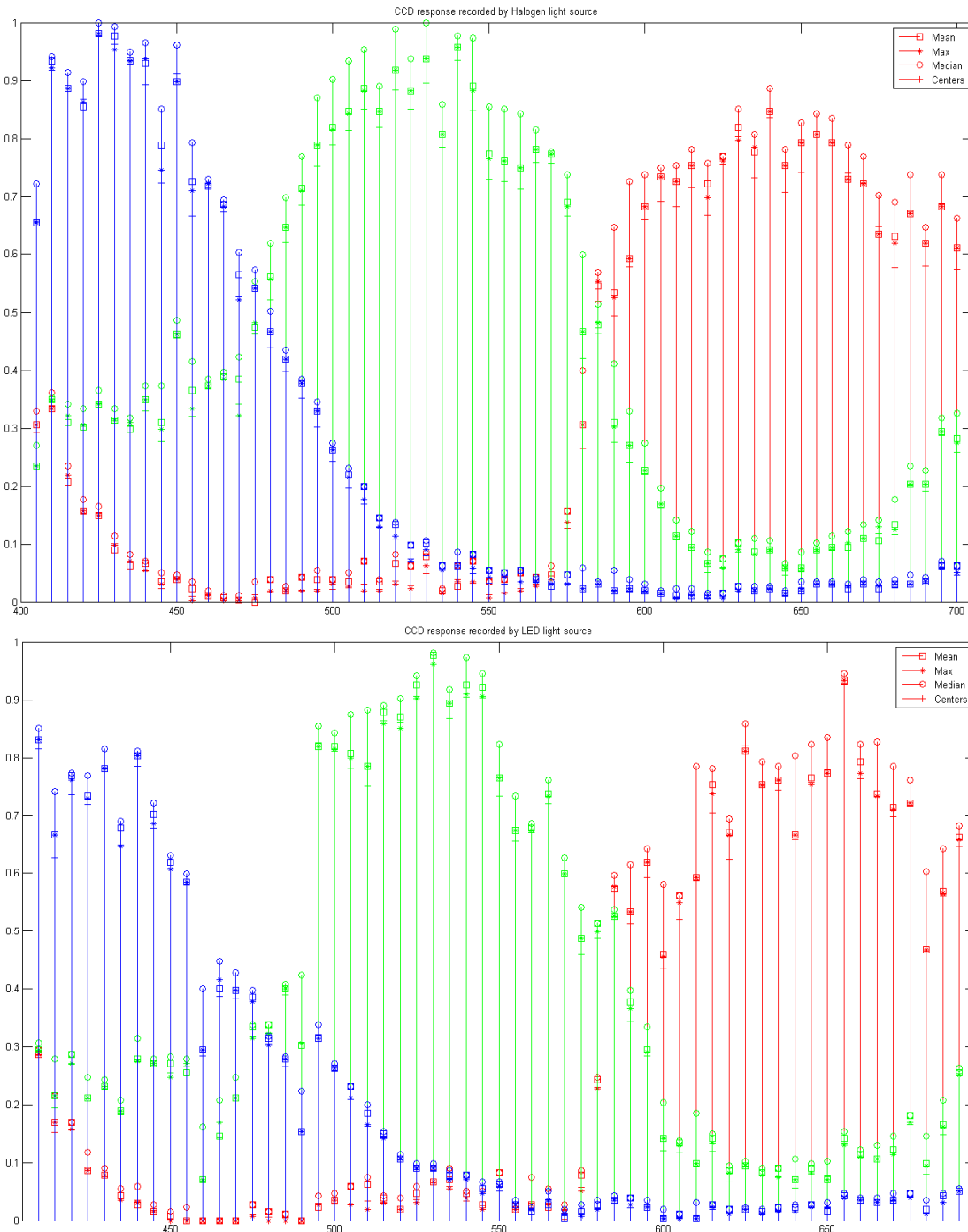
Figure 25 Spectral sensitivity of the sensor recorded at each wavelength using the mean, max and median value of a 10x10 pixel area in the center and the central pixel. On the bottom is the recorded sensitivity using a Halogen lamp on top is using the LED light source.

As it can be seen in Figure 25 the recordings differ while using different light sources and keeping the rest parameters of the experiment stable, meaning same lenses, sensor and optomechanical parts. These differences amount to differentiations of the measurement parameters by human interference on the optomechanical parts and the sensor settings. In more detail, the wavelength output of the monochromator is dependent on the angle of incident light at the inner optics. This exact angle is almost impossible to be reproduced in multiple measurements. Moreover, the spectrometer measurements are not accurate but approximate on the light intensity as a photometer would be, yet the luminescence of a single LED at a single wavelength band is under the measuring capabilities of standard photometers without mounting focusing lens, as it was practically observed.

This leads on slight differentiations of light intensity between wavelength steps as well as the two light sources. Finally, this light source per wavelength intensity difference was apparent at the sensor, therefore different sensor settings, more specifically Shutter and Gain parameters, were used in order to achieve same pixel intensity with both light sources during the white balancing procedure.
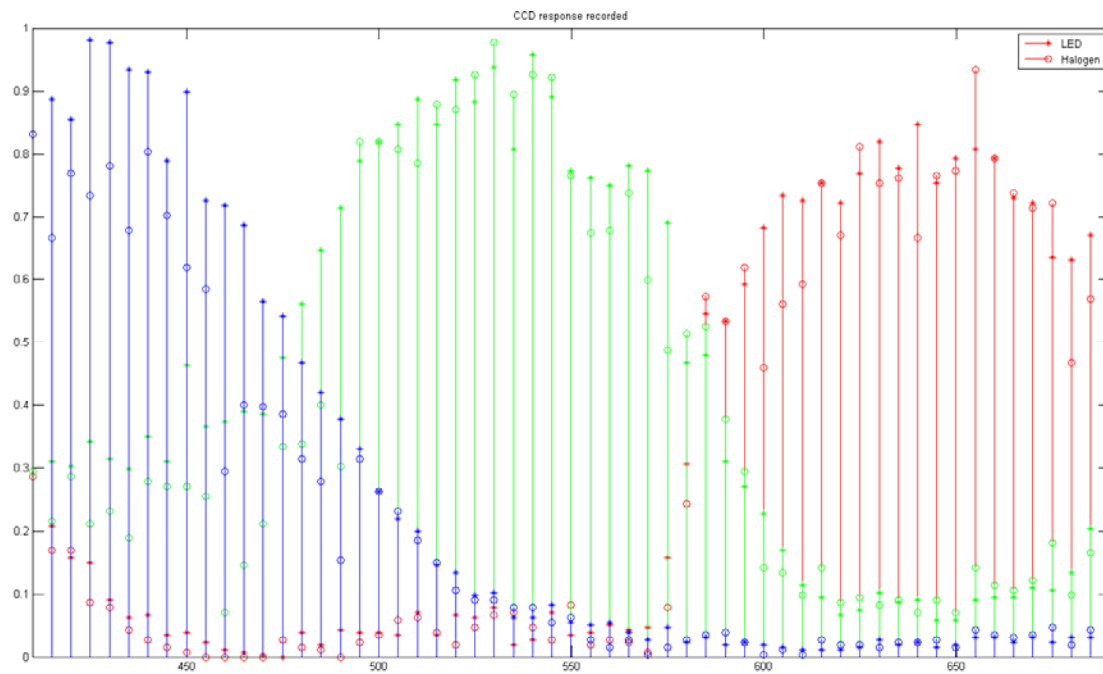
Figure 26 Spectral Sensitivity recorded by the sensor at the central pixel

As seen in Figures 24 to 26 all three channels provide signals at each and every wavelength, as a summed physical manifestation of channel cross-talking phenomenon of all possible sources. Figure 27 is the final outputted spectral sensitivity of the specific sensor, having impact on the performance quality of the sensor during imaging, as well as the results of solving the equation 3.3. The intermediate wavelengths are interpolated so as each profile has information for every wavelength with step 1nm instead of 5nm step.

From equation 3.2 and based on the analogies per measured nanometer the cross-talking of the channels can be quantified as:

$$RGB' = W^{-1} * RGB \Rightarrow$$

$$
\begin{array}{c} R' \\ G' \\ B' \end{array}
=
\begin{array}{ccc} 1 & -G/R & -B/R \\ -R/G & 1 & -B/G \\ -R/B & -G/B & 1 \end{array}
*
\begin{array}{c} R \\ G \\ B \end{array}
\qquad (3.4)
$$

Where:
- R', G' and B' are the estimated unmixed channel responses and
- R, G and B are the measured channel responses.
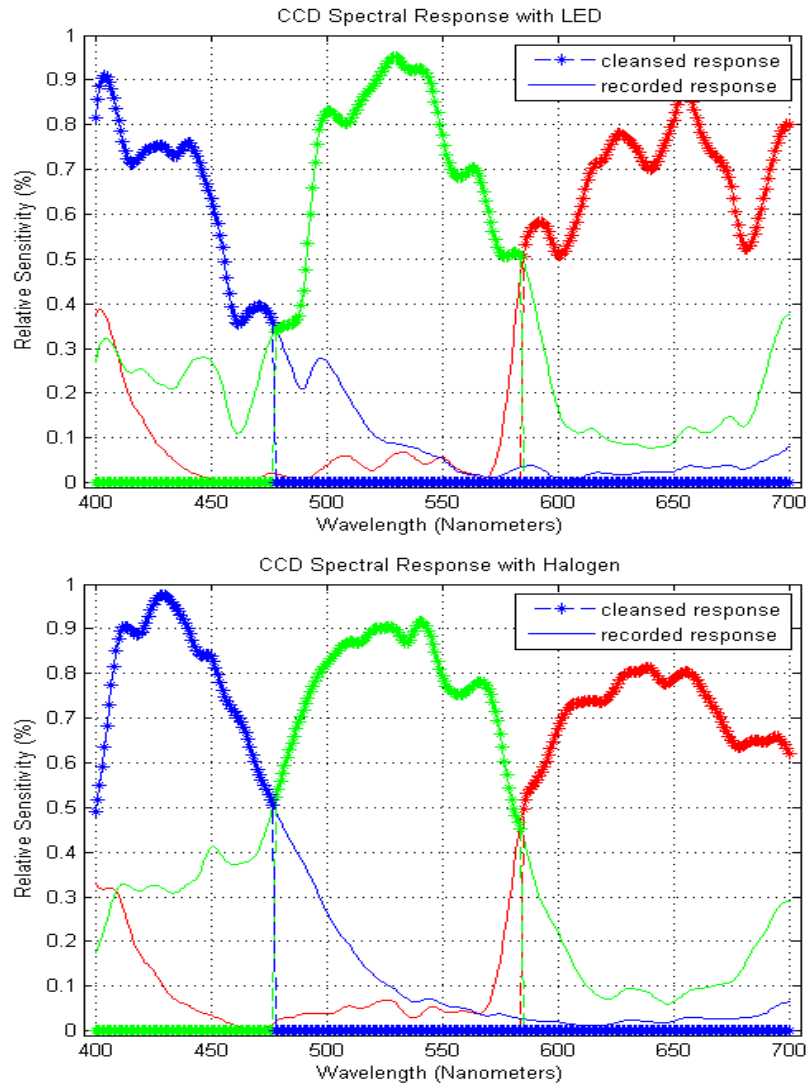
Figure 27 The spectral sensitivity of the camera before and after application of the 3.3. On top using the tunable LED light source and on bottom using the Halogen lamp light source.

42

The RGB response of a camera for a given channel is the integral of the spectral response of the channel. Knowing the spectrum of the light source, the margins of the spectral response integral are known, thusly the expected camera RGB response can be calculated from the measured spectral response and thusly the proper weight matrix for the cleansing algorithm can be calculated.

In case of the full visible spectrum captured by a common RGB sensor the weighted matrix at white balance settings used during the measurement, has been calculated as

$$W^{-1} = \begin{bmatrix} w_{RR} & w_{RG} & w_{RB} \\ w_{GR} & w_{GG} & w_{GB} \\ w_{BR} & w_{BG} & w_{BB} \end{bmatrix}^{-1} = \begin{bmatrix} 1 & -G/R & -B/R \\ -R/G & 1 & -B/G \\ -R/B & -G/B & 1 \end{bmatrix} = $$
$$\begin{bmatrix} 0.9632 & -0.2122 & -0.0421 \\ -0.1218 & 0.9550 & -0.1282 \\ -0.1405 & -0.4338 & 0.9193 \end{bmatrix} \quad (3.5)$$

White balance

The manual of the camera used in the experiment mentions that the white balance can be adjusted with three coefficients, one for each colour channel. These coefficients can be set individually in order to increase or decrease the contribution of each channel and therefore allow the user to control the colour tint of the image, with range of values [0, 8] and in practise provide the natural channel contribution for value 1. This contribution is in principal a digital gain applied per channel, configurable by 8-bit SPI registers according to:
- The 2 MSB are used for precision P
- The 6 LSB are used to control the gain G (from 0 to 63)
- The digital colour gains follow this rule:

$$Gain = 2^{P-2} * (1 + \frac{G}{64}) \quad (3.6)$$

- For P=0 Gain varies from 0.25 to 0.5 in steps of 0.004
- For P=1 Gain varies from 0.5 to 0.99 in steps of 0.008
- For P=2 Gain varies from 1 to 1.98 in steps of 0.016
- For P=3 Gain varies from 2 to 3.97 in steps of 0.0.31

In practice, we measure the effect the channel gain changes have on a measurement of a white target. For this purpose the light sources are set to standard unchanging settings
- LED source set to equal luminosity for each LED
- Halogen source set to default luminosity in medium level of current

Moreover, camera settings (Shutter, Gain etc.) except for channel individual gain is fixed and unchanged through the experiments

Channel individual gain is changed in steps from the available values [0, 8] dB with variations in order to study their influence.

Eight different base measurements were made where
- Each channel gain was set to the same value with 0.01 step intervals
- The channels were set to the values that provided white balance for the measurements in Subchapter 3.5.2 and each channel gain was altered stepwise (step = 0.01) and in turn
- The channels were set to the values that provided white balance for the measurements in Subchapter 3.5.2 and the other two channel gains were altered stepwise (step = 0.01) and in turn
- The channels were set to the zero and each channel gain was in turn altered stepwise (step = 0.01)

In conclusion, CCD behavior in individual channel gain is affected by the light source spectrum as seen by the response with Halogen light source towards the behavior with the LED light source. On the other hand, the tendency exhibited is similar to both light sources, where the channel contribution change exponentially. This allows the estimation of the expected influence to the cleansing coefficients in cases where the individual channel gains of the camera is in different settings than the ones used in order to train the system and calculate the channel analogies. Thusly, equation 3.5 becomes

$$RGB_{cleansed} = (W^{-1} * W_{wb}) * RGB_{recorded} \qquad (3.7)$$

Where

$$W_{wb} = 1 - (RGBGain_{training} - RGBGain_{current}) \qquad (3.8)$$

Different cameras allow control over $RGBGain$ with different methods or to a different extents. In order to have W_{wb} independent of the camera at hand, the weight can be calculated directly from the response of the camera to a white target. The three channels have been measured at a given balance at the given emission of a light source. This balance can be correlated with the balance measured by an image of white target captured with another sensor and the weight matrix that was experimentally measured can be accordingly adjusted to correspond to sensors of different quantum efficiency than the one used in our measurements.

By measuring the changes on the response of the camera when the only variable tampered is the analog gain of each channel we identify a consistent linearity to the intensity changes. This changes are more apparent using the LED light source were all channels are exposed to a flat white spectrum instead of exposure to the emitted spectrum of the halogen source where there is little intensity at the blue wavelengths and high intensity at the red ones.
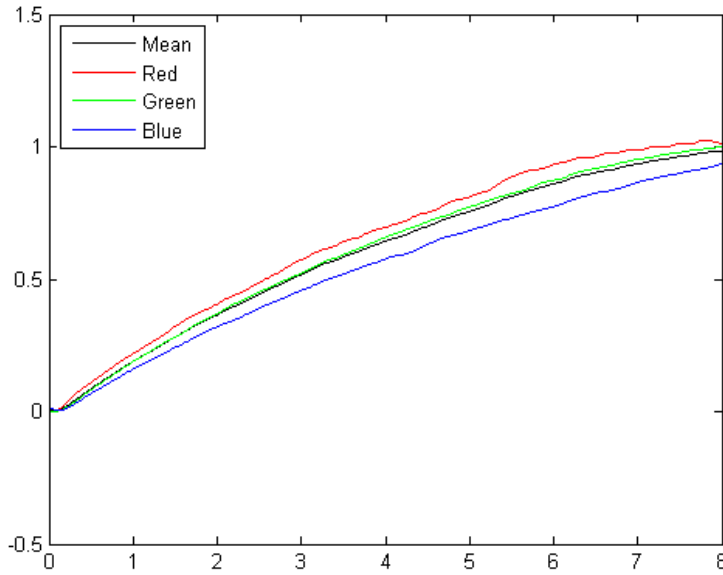
Figure 28 Difference in the recorded per channel response, when all acquisition parameters are stable and white balance is altered stepwise for each channel
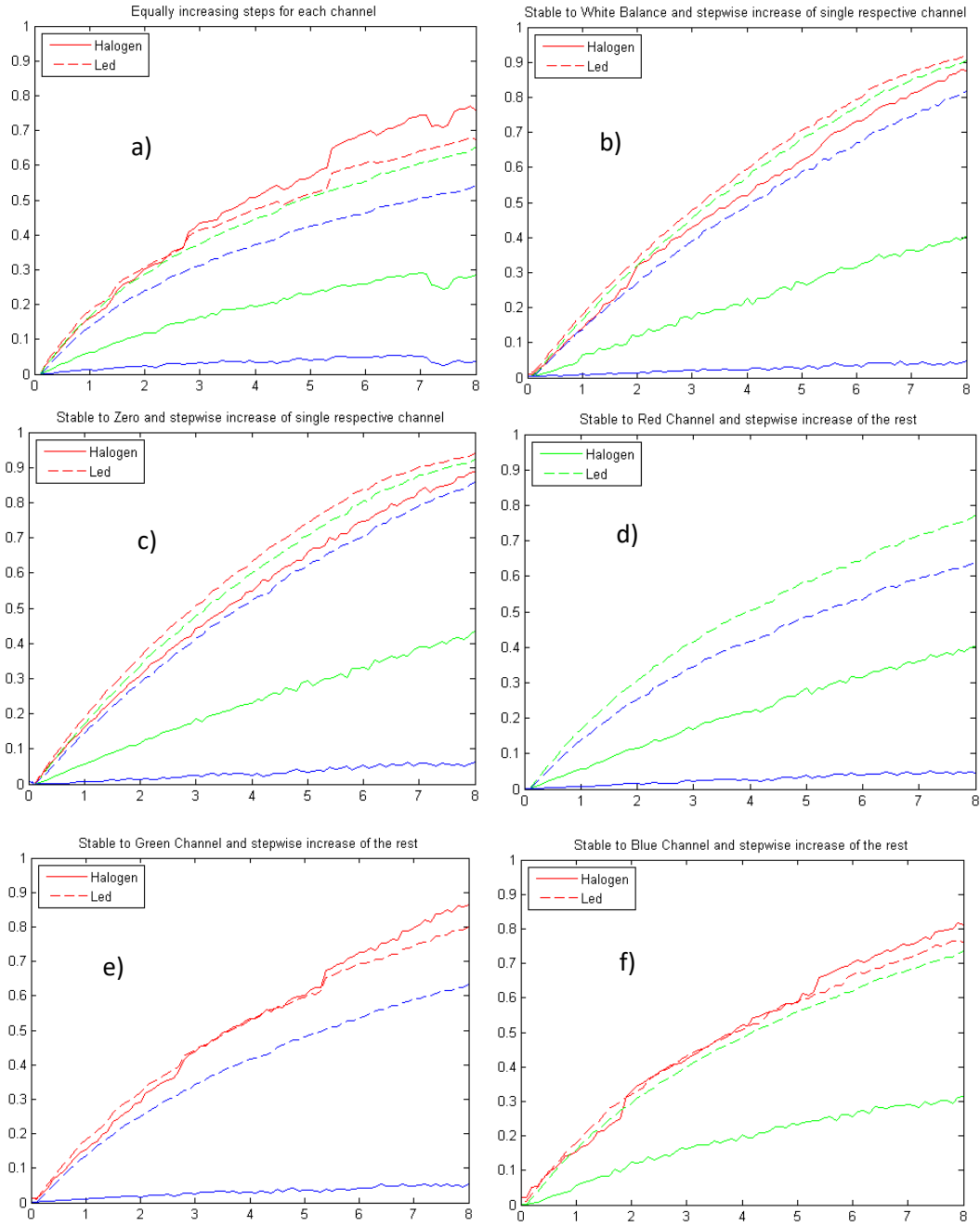
Figure 29 Difference in the recorded per channel response, when all acquisition parameters are stable and white balance is altered:

a) all 3 channel gains are increased stepwise simultaneously

b) each channel gain is increased stepwise while the other two are set constant to the value during the training measurements

c) each channel gain is increased stepwise while the other two are set constant zero

d) each channel gain is increased stepwise while the red channel is set constant to zero

e) each channel gain is increased stepwise while the green channel is set constant to zero

f) each channel gain is increased stepwise while the blue channel is set constant to zero

3.6   Channel Cleansing Algorithm

Thusly equation 3.7 is the mathematical representation of the Channel Cleansing Algorithm:

$$RGB_{cleansed} = (W^{-1} * W_{wb}) * RGB_{recorded} \qquad (3.7)$$

Where W^{-1} is a 3x3 normalised matrix where that removes the contribution of each channel towards the other two and W_{wb} is the difference of the current balance of the three channels in correlation with the balance during the experimental measurements. This matrix holds all the information needed to remove the channel cross-talk phenomenon from the information acquired by a multichannel sensor, while on the same time isolated the spectral information according to the selected spectral range.

By applying pixel by pixel the equation 3.9 to the acquired images by the monochromator measurements, the following images come as result:
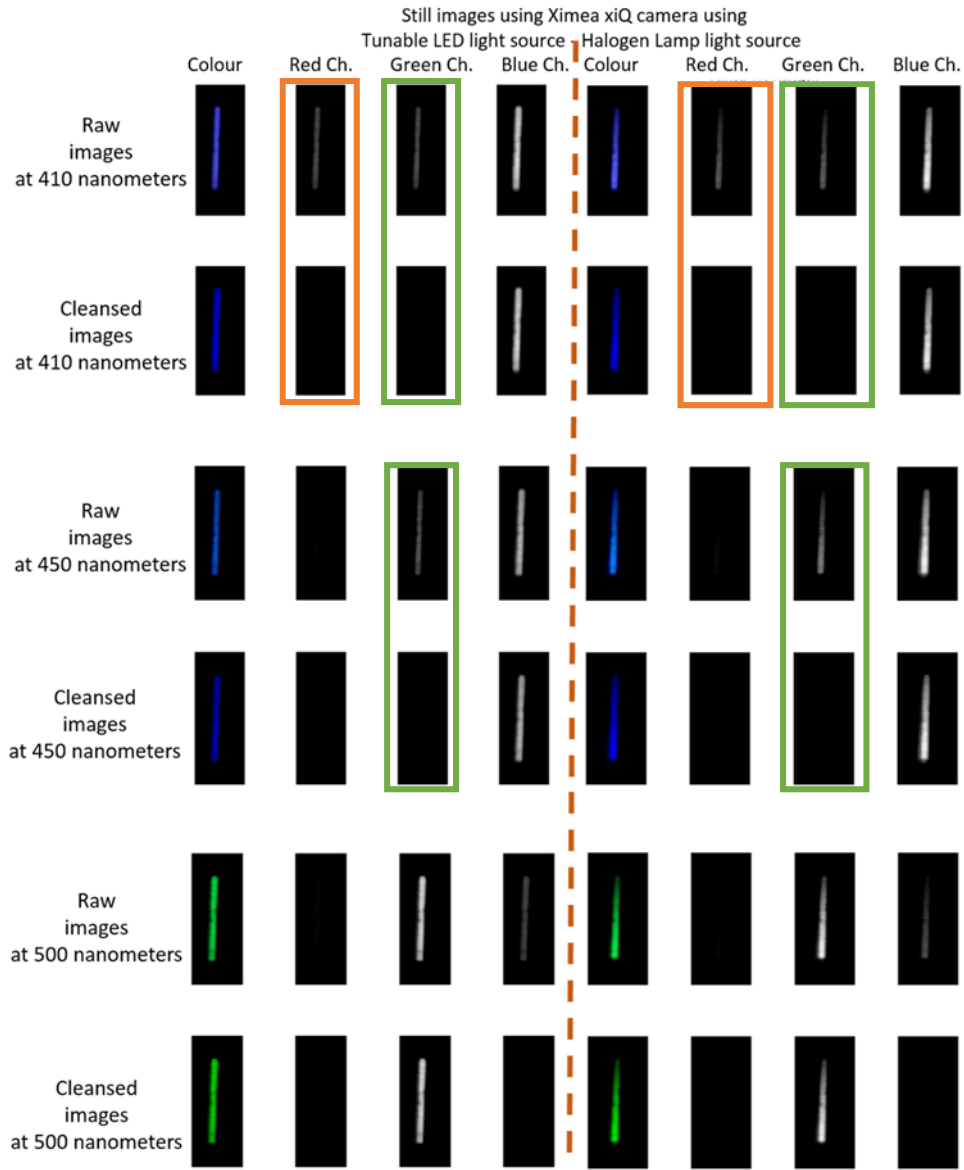
Figure 28 Shot noise free images at 410, 450 and 500 nanometres. Left of the dashed line are images acquired using the tuneable LED light source, whereas right are acquired using the halogen lamp light source. Each first raw per nanometre is the average of four frames of the same target without further processing, while each second row is the image after removing the channel cross-talking phenomenon.
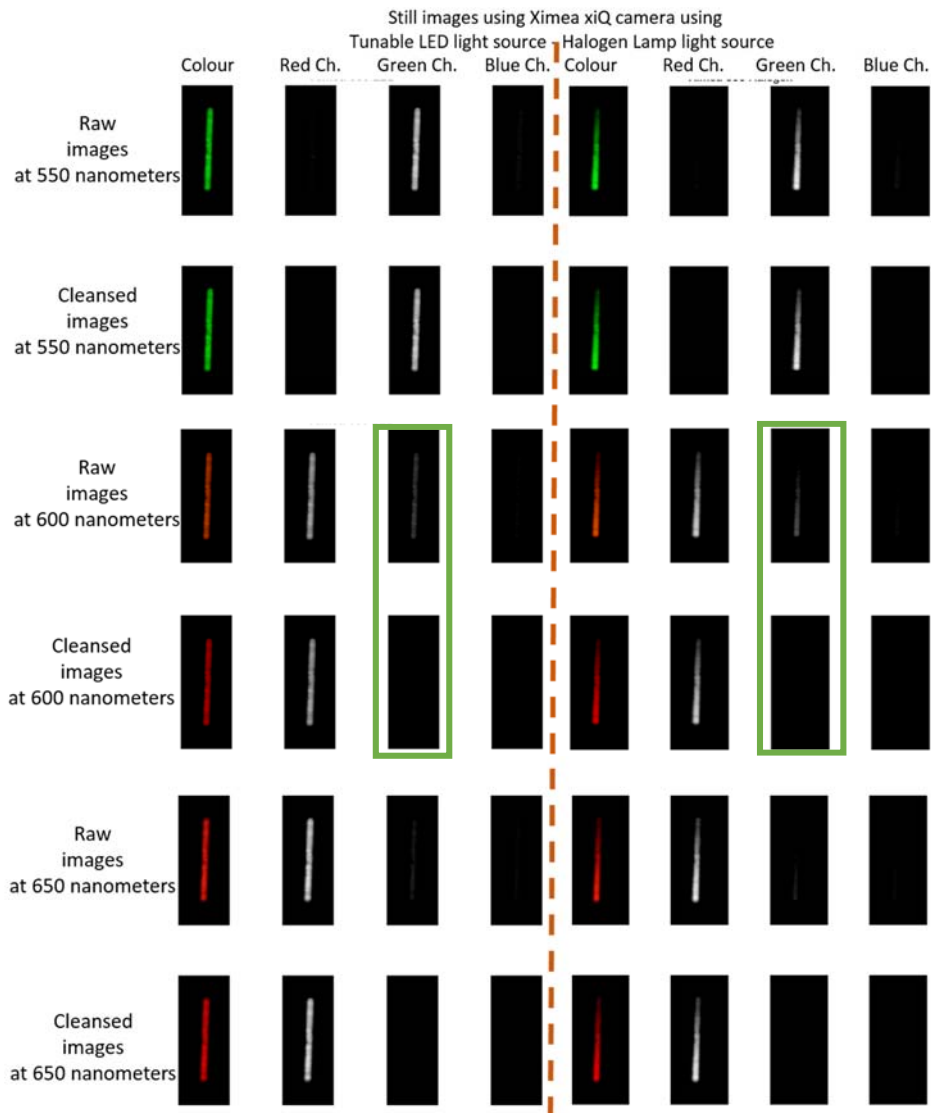
Figure 29 Shot noise free images at 550, 600 and 650 nanometres. Left of the dashed line are images acquired using the tuneable LED light source, whereas right are acquired using the halogen lamp light source. Each first raw per nanometre is the average of four frames of the same target without further processing, while each second row is the image after removing the channel cross-talking phenomenon.

As seen in Figures 30 and 31, the procedure spectrally isolates the dominant channel from the other two and removes the cross-talk phenomenon. The cross-talk phenomenon is more intense at bordering nanometers between channels, such as 500 and 600 nanometers, and even more so at the edges of the colour filter edges such as 410 nanometers. This inteferrence is removed while the intensity of the dominant channel remains at nominal levels.

4. Channel Cleansing algorithm in Practice

In order to assess the accuracy and efficiency of the weighting factors proposed, two separate experimentations were conducted and assessed using common metrics used in literature.

Firstly, a reflective white target was used, while a LED light source consisting of 3 LEDs is used to simulate a multiband optical filter simulating the acquisition process of a sensor needed for real time spectral imaging. In comparison to the methodology a simplified version of the weighting factors is used by calculating the analogies of each single LED exposure compared to a target captured with simultaneous exposure to the triplet of LEDs.

Secondly, full spectra of selected Roscolux filters were acquired using the MuSIS HS camera. Then spectra were estimated based on sequential single LED emissions as well as simultaneous emissions of two triplets of LEDs in order to assess the trade-off between acquisition time and estimation accuracy.

4.1 Commonly Used Metrics

4.1.1 Euclidean Distance

In mathematics, the Euclidean distance or Euclidean metric is the "ordinary" distance between two points that one would measure with a ruler, and is given by the Pythagorean formula. By using this formula as distance, Euclidean space (or even any inner product space) becomes a metric space. The associated norm is called the Euclidean norm. The Euclidean distance between point p and q is the length of the line segment connecting them ($\overline{pq}$).

In Cartesian coordinates, if $p = (p_1, p_2,..., p_n)$ and $q = (q_1, q_2,..., q_n)$ are two points in Euclidean n-space, then the in-between distance is given by:

$$d(p,q) = d(q,p) = \sqrt{(q_1 - p_1)^2 + (q_2 - p_2)^2 + \cdots + (q_n - p_n)^2}$$

$$= \sqrt{\sum_{i=1}^{n}(q_i - p_i)^2} \qquad (4.4)$$

4.1.2 Root Mean Square Deviation (RMSD)

The root-mean-square deviation (RMSD) is a frequently used metric of the differences between estimated and observed values, representing the sample standard deviation of their differences. RMSD is a proper measure of accuracy, only to compare forecasting deviation of different models or methods for a particular variable and not between variables, due to scale dependency.

$$RMSE = \sqrt{\frac{\sum_{i=1}^{n} \Delta x_i^2}{n}} \qquad (4.1)$$

Where, in the scope of this thesis

- n is the number of spectral channels
- x the spectral reflectance vector.
- Δx_i^2 is the squared difference of the i-th channel values of 2 spectra.

4.2 Measures of Spectral Similarity

4.2.1 Spectral Angle Mapper (SAM)

Spectral Angle Mapper (SAM) is a physically-based non-parametric supervised spectra classifier that uses an *n*-D angle to match pixels to reference spectra [31]. It determines the spectral similarity between two spectra by calculating the angle between them and treating them as vectors in a space with dimensionality equal to the number of bands. This technique, takes into consideration only direction of vector and not length, thusly is relatively insensitive to illumination. Smaller angles represent closer matches to the reference spectrum. SAM classification assumes reflectance. However, if radiance data are used, the error is generally not significant because the origin is still near zero.

$$\langle x, y \rangle = \|x\|\|y\| \cos(x, y) \rightarrow$$
$$\theta(x, y) = SAM(x, y) = \cos^{-1}\left(\frac{\langle x,y \rangle}{\|x\|\|y\|}\right), \ \ 0 \le \theta \le \frac{\pi}{2} \tag{4.2}$$

4.2.2 Goodness of fit (GFC)

GFC is defined as the cosine of the angle between the estimated spectrum $\hat{S}$ and MUSIS HS acquired spectrum S, thus

$$GFC = \frac{\sum_{\lambda=400}^{700} \hat{S}(\lambda)S(\lambda)}{\sqrt{\sum_{\lambda=400}^{700} \hat{S}(\lambda)}\sqrt{\sum_{\lambda=400}^{700} S(\lambda)}} \tag{4.3}$$

4.2.3 Accuracy Validation Thresholds

In order to quantify the spectral match between the measured and estimated spectra, the aforementioned quantitative measures were used in combination to produce three thresholds, used as criteria in order to indicate the level of accuracy.

	GFC (%)	**Spectral Angle (rads)**
Criterion 1	> 99	< 0.2
Criterion 2	> 99.5	< 0.1
Criterion 3	> 99.9	< 0.1

The level of accuracy was defined by the following:

Estimation Measures < 1st threshold: Satisfactory or poor

$\geq$ 1st threshold: Good estimation

$\geq$ 2nd threshold: Very good estimation

$\geq$ 3rd threshold: Excellent estimation

4.3   Channel Cleansing Validation

In order to confirm the robustness and quality of the procedure, the quantum efficiency of CCD coupled with MBPF is simulated using LEDs
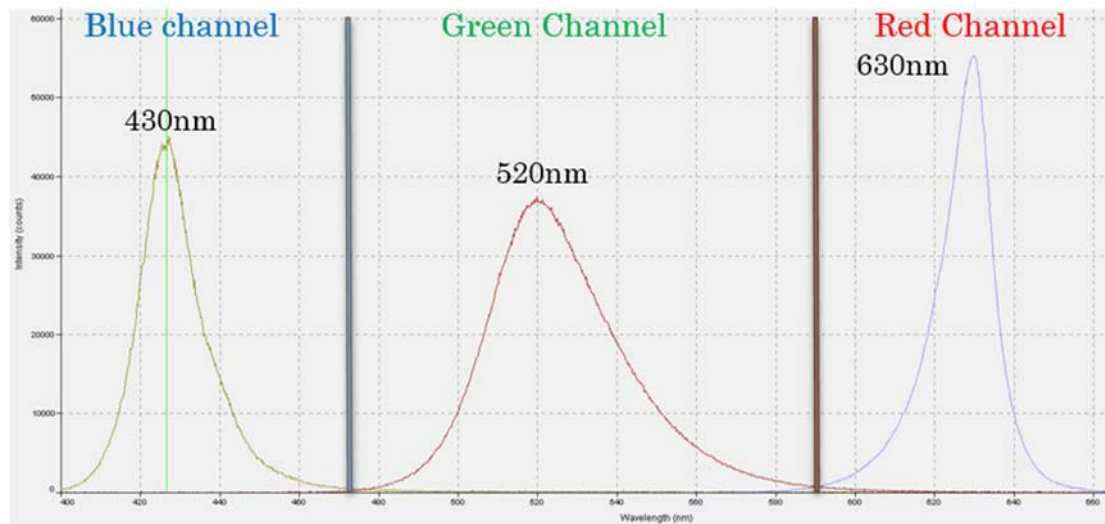
Figure 30 The spectral emission of the LEDs used to simulate α triple band pass optical filter. The spectrum is divided based on the spectrum recorded by each channel. The wavelength of the peak intensity is identified for each LED
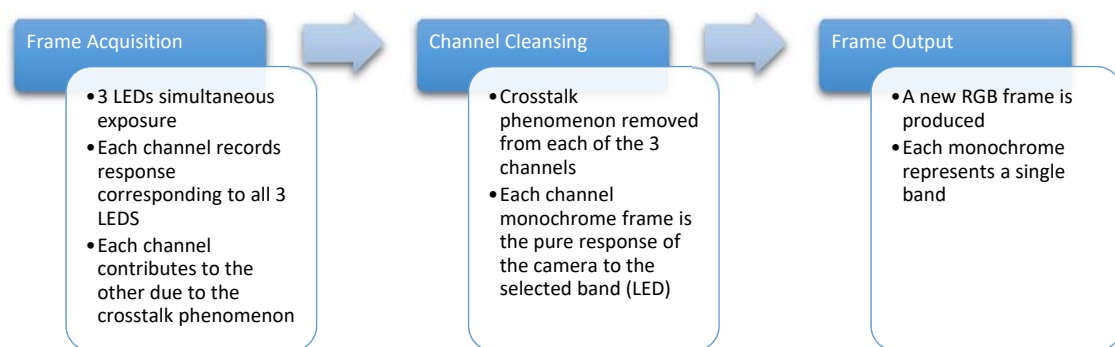
Figure 31 General Flow Chart of the Cleansing Algorithm

The participation of each channel to each band is measured in order to be properly deconvolved. Moreover, the participation of each channel to each of the rest channels based on the exposed EMR is measured in order to be properly cleansed. A weight matrix is created to correspond to the spectral range in question. The crosstalk phenomenon is physically removed and each channel corresponds to a single wavelength band.

Two different weight matrices are used in order to compare and contrast accuracy of the cleansing. One is the weight matrix formulated by recorded response with monochromator as described previously. For all means and purposes the first matrix will be referred to as theoretical weight matrix. The second is a weight matrix formulated by recorded response of the sensor with single LED exposure for each of the 3 bands in order to calculate contribution

of each channel towards the other as well as towards each spectral band. For all means and purposes the second matrix will be referred to as LED weight matrix. As target, a white reflective target was selected.

In both methods, the steps of the algorithm remain the exact same as described in 3.6. The only difference is the weighted matrix used each time. The overall flow of the algorithm can be seen in Figure 33.
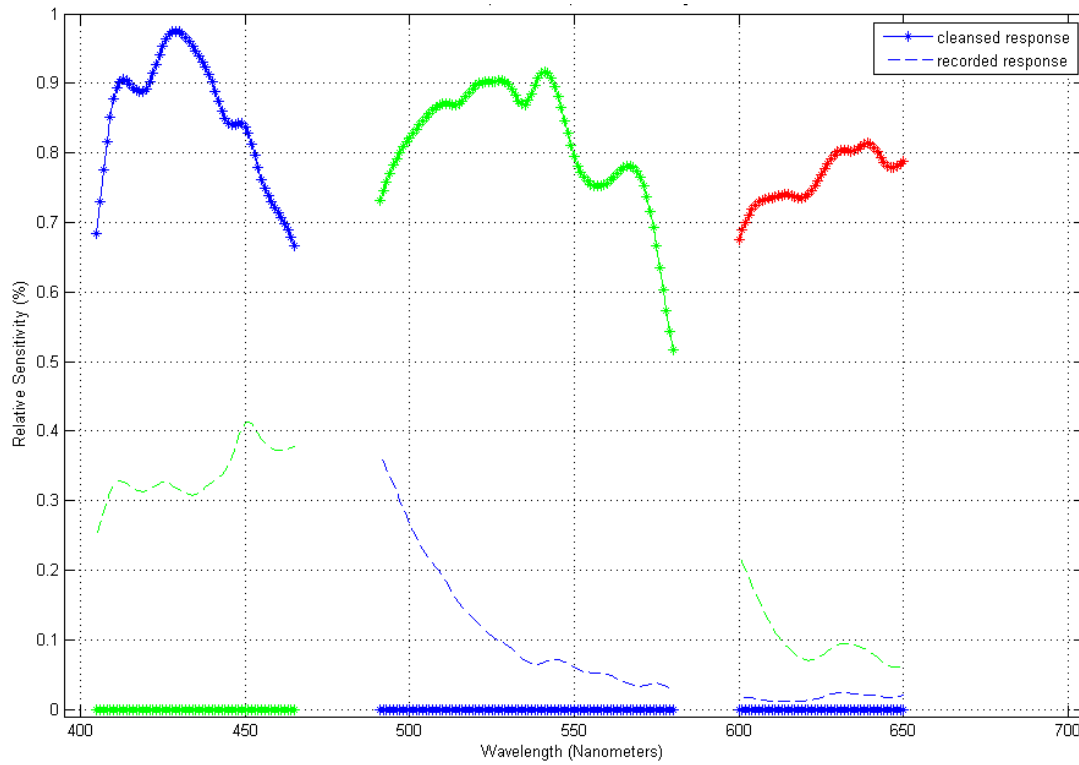
Figure 32 The spectral sensitivity of the RGB sensor once coupled with a triple band pass filter of the spectrum defined by the set of LEDs

The set of LEDs is 430, 520 and 630 nanometres. In Figure 34 the simulated spectral sensitivity of the sensor is given. The sensitivity would be as such, if it was coupled with triple band pass filter that had narrow bands ranging within the spectral emission range of the LEDs.

What needs to be noted is that White balance of the RGB sensor was set in such a manner that each channel would have equal intensity when all three are active. These settings, if the sensor was crosstalk free, amount to acquiring spectral information by activating each LED in turn and retaining information only from the dominant channel. This is a common practice that amounts to using a monochrome sensor and sequential LED activation to acquire the spectral cube.
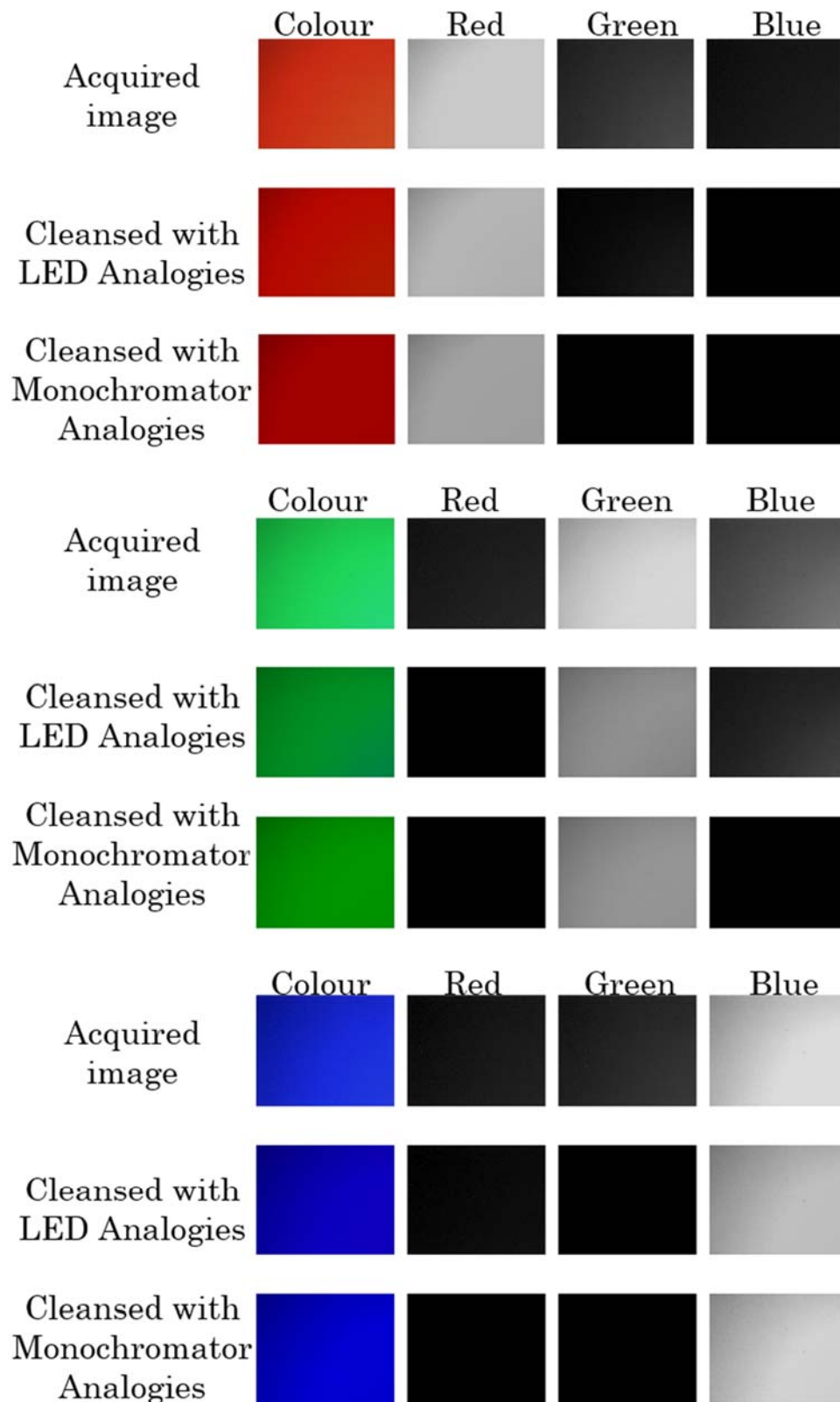
Figure 33 White reflective target exposed to a single LED each time. In the first row of each channel is the image acquired directly from the sensor. The second raw depicts the image after crosstalking phenomenon is cleansed using the LED analogies whereas the third was cleansed using the monochromator analogies. First column is the colour three-channel images and the next three columns is their respective monochrome channels.

In Figure 33, white target was imaged having active only one of the three LEDs in turn. In the first column the colour image acquired from the sensor is shown and then split to its three respective monochrome channels. The acquired images are cleansed of the cross-talking phenomenon using the monochromator analogies as depict on the third row per channel. Using these three images as reference a weight matrix of channel contributions is calculated in a similar methodology as the monochromator one and its results are shown on the second row of each of single LED acquired images.

Table 5 Mean relative pixel intensity of the sensor when exposed to a single LED

Active LED	Camera Channels	Acquired Image	LED weights	Monochromator weights
Red	Red	98.32 %	87.90 %	78.56 %
	Green	25.16 %	**6.57 %**	**0.00 %**
	Blue	11.09 %	0.02 %	0.00 %
Green	Red	14.16 %	0.00 %	0.00 %
	Green	99.73 %	67.75 %	69.66 %
	Blue	42.06 %	**18.98 %**	**0.00 %**
Blue	Red	10.76 %	**4.75 %**	**0.00 %**
	Green	18.95 %	0.00 %	0.00 %
	Blue	99.25 %	86.24 %	95.06 %

Subjectively we could argue that both cleansing matrices are as efficient and successful. One could even argue that only when exposed on the green LED the crosstalking phenomenon is present, which is easily proven false when the pixel intensities are examined. In order to objectively and quantitatively asses the process of cleansing of the images, the mean relative pixel intensity is compared.

As presented in Table 5 it is evident that a crude calculation of the weight matrix using single LED exposed images although it provides a good estimation, it fails to effectively remove the entirety of the crosstalking phenomenon. On the other hand using the weights calculated with the monochromator methodology, the crosstalking phenomenon is entirely removed. Moreover, the green and blue channels are less impacted by the monochromator matrix, by allowing 1.91% and 8.82% higher mean relative sensitivity, while the red has been dimmed by 10.56%. This is consistent if the wider spectral bands of the blue and green LED towards the red is considered.

These findings conclude that channel crosstalk cleansing can be achieved with statistical significant quality. The theoretical weight matrix yields higher results than a simply calculated matrix between the analogies from single LED exposure, yet it is unable to properly cleanse the images if it is lacking a priori knowledge of the light source emitted spectrum. Moreover, the

time complexity of the procedure to deconvolve and cleanse the images is allowing for video rate acquisition of the bands, thusly, enabling incorporation to the real time spectral imaging system described in Subchapter 2.6.3 and consequently increasing spectral fidelity by successfully removing the cross-talk phenomenon.

It is deem worthy for further investigation assessing the differences that occur from the use of different sensors at the exposure to identical targets and spectral bands in order to further investigate the robustness and accuracy of the proposed methodology.
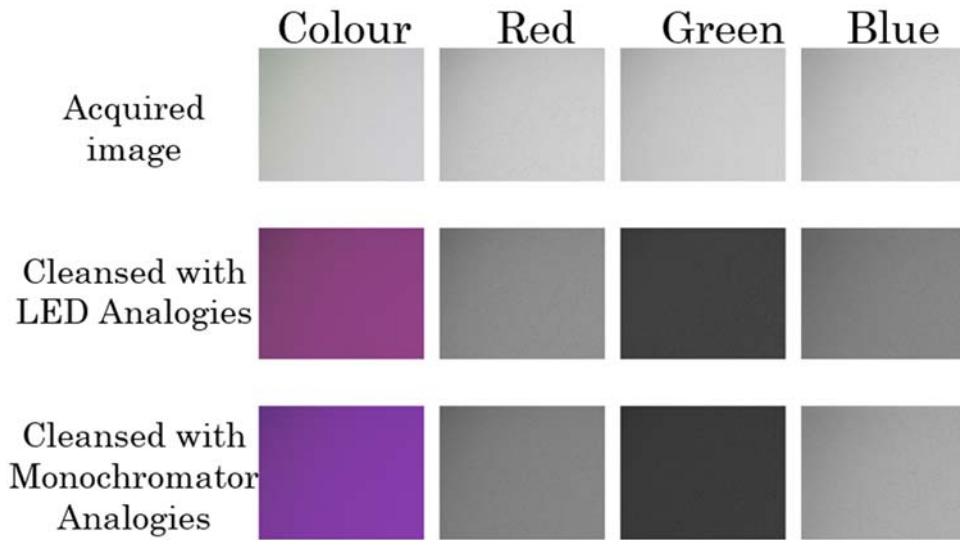
Figure 34 White reflective target exposed to all three LED. In the first row is the image acquired directly from the sensor. The second raw depicts the image after crosstalking phenomenon is cleansed using the LED analogies whereas the third was cleansed using the monochromator analogies. First column is the colour three-channel images and the next three columns is their respective monochrome channels

In Figure 34, the results of deploying the cleansing algorithm in an image acquired by simultaneous exposure to all three LED which simulate white light. The resulting images from both methods of calculating the weight matrix result in images that seem similar to the human eye. As seen in Table 6, when the sensor is exposed simultaneously to all three LEDs, the resulting crosstalking-free image is in need of recalibration in order to be balanced towards white. Moreover, the green channel is heavily dimmed, which is rational considering that it is the channel that contributes the most towards the other two bands and on the same time the green LED is the one with the widest full width half max emission of three.

Table 6 pixel intensity of the sensor when exposed to all three LEDs

Camera Channels	Acquired Image	LED weights	Monochromator weights
Red Channel	97.92	67.70	63.10
Green Channel	98.36	32.19	29.07

Blue Channel	97.58	62.39	80.10

4.5 Spectral Estimation Validation

In order to determine the impact of the procedure upon spectral estimation a second test was designed. A set of spectral targets of Roscolux filters was chosen, given in more detail at Table 7.

Table 7 Roscolux Filter Sets

Name	Code	Name	Code
Dempster Open White	00	Hemsley Blue	361
Medium Yellow	10	Italian Blue	370
Deep Straw	15	Leaf Green	386
Flame	18	Neutral Grey	398
Scarlet	24	Storaro Azure	2006
Turquoise	92	Full Blue	3202
Kelly Green	94	Roscosun 85N3	3405
Chocolate	99	CalColor 90 Green	4490
Neon Pink	343	CalColor 60 Magenta	4760

The set was used to train spectral estimation algorithm in order to acquire the full spectrum from 400 to 700 nanometers from six discrete spectral bands. The estimated full spectrum is compared for accuracy with full spectrum acquired by MUSIS HS full spectrum acquisition spectral camera. In the scope of this study, the actual accuracy and quality of spectral estimation was not under study, but merely the influence of spectral deconvolution and channel cleansing to the quality of spectral estimation. Training of spectral estimation was conducted once for data acquired by single LED exposure and once for data acquired by simultaneous exposure to two sets of three LEDs. In order to compensate for acquisition calibration errors, the spectra are normalized towards the Dempster Open White Rosco film.

In order to quantitatively compare the results, spectral similarity metrics were employed as described in Subchapter 4.2.

In detail, each full spectrum was acquired first by MUSIS HS and was designated as the reference spectrum. This is necessary as scanning hyperspectral imaging systems are considered the golden standard for full spectrum acquisition of static targets. These spectra are used as reference to assess the quality of each estimation.
Following, each target was exposed successively to each one of the six LEDs. After that, each target was again exposed with the same camera settings and the same LED luminance to the two sets of three LEDs. Each exposure was calibrated in order to be of significant intensity without noise interference, yet in levels where no saturation transpired. Each spectrum acquired was normalised towards the 00 Dempster Open White spectrum acquired from the equivalent acquisition procedure in order to remove calibration errors.
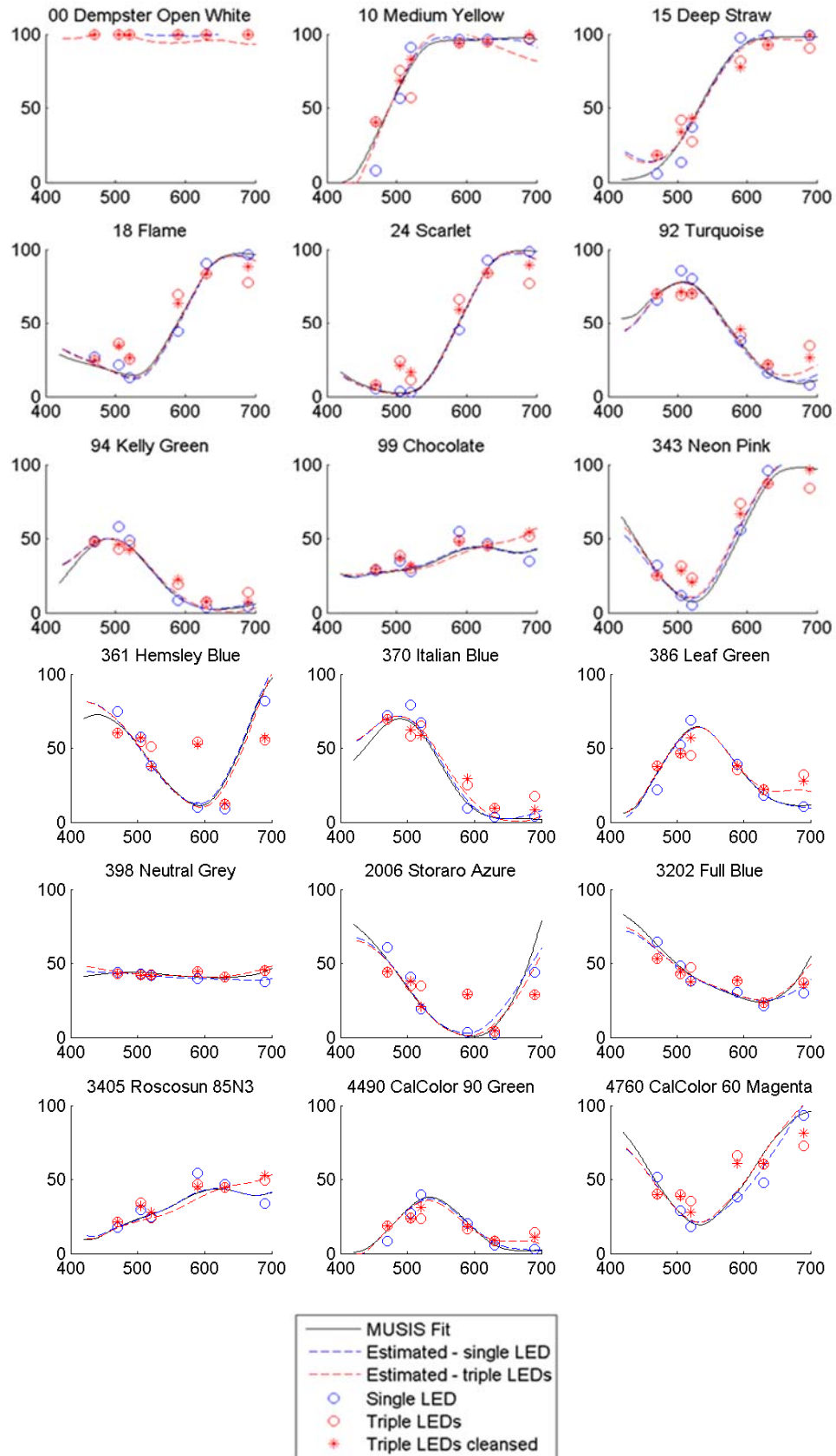
Figure 35 The spectra of 18 selected Roscofilm Spectra Target Filters is scanned by MuSIS (black). The targets were also imaged after sequential exposure to six narrow spectrum emission LEDs (blue circle) and simultaneous exposure to sets of triple of the same LEDs (red mark). The full visible spectrum for each target was estimated from the two different imaging methods using Wiener approximation.

In Figure 35 the spectrum of each Rosco filter is presented. In each graph with black is represented the spectrum acquired by the hyperspectral camera. Single LED exposure is denoted with blue whereas deconvolved and triple LED exposure is represented with red. The respective values after channel cleansing is denoted with red mark. The value of each filter is the mean of a full frame. Each value is normalised towards the equivalent spectrum of the first filter target, to remove deviations due to errors in acquisition procedure. As it can be seen in the figure, the actual cleansed recordings provide a higher spectral accuracy compared to the raw ones, with each value shifting towards the spectral curve, with rare exceptions.

Estimated spectra by either procedure, manifest a certain degree of deviation from the acquired spectra by MUSIS. This is due to insufficiency of the spectral estimation training set and deficiencies of the white balance calibration, which can be solved with more detailed training and more accurate white balance calibration during acquisition. Accuracy of the spectral estimation is out of the scope of this study.

It is our point of interest to compare only the influence of spectral deconvolution and cleansing procedure, without regards to the quality of the accuracy. For this reason, in order for accurate comparison of the procedure, the study focus to the deviation of the procedure by using a standard common denominator, that is the scanning spectral imaging. For that reason all the parameters of the acquisition remain the same in both imaging procedures.

Table 8 Quantitative Comparison Data of Spectral Estimation

	Euclidean Distance (%)	Goodness Of Fit (%)	Spectral Angle (rads)	Criterion 1 (%)	Criterion 2 (%)	Criterion 3 (%)
Single LED acquisition	6.44	99.83	0.0524	100	94	33
Triple LED acquisition – Deconvolved and cleansed.	8.20	99.66	0.0719	94	72	22
Difference	1.76	-0.17	0.0195	-6	-22	-11

As presented in Table 8 all methods present high accuracy and satisfy sufficiently at least the two first criteria. As evident, both procedures provide similar results. Euclidean distance loses accuracy by 1.76% whereas goodness of fit by merely 0.17%. On the other hand spectral angle loses accuracy by 0.0195 rads. These findings show that at a significant gain of acquisition speed the spectral estimation is aggravated by a minimal amount. Finally, in cases where single band exposure is unattainable, such as the use of multi-bandpass filters, it is proven that the estimation algorithm will not suffer severely, but can provide high quality results and higher accuracy of the spectral estimation can be attained by more detailed and carefully calibrated training of the algorithm. Moreover, further investigation with more accurate acquisition methods and finer white balance calibration that incorporate the spectral deconvolution and cleansing procedure, would provide higher spectral estimation accuracy.

From a qualitatively point of view, one can argue that the impact focuses mainly on the edges of the selected spectral bands. This can be speculated to be due to need for more detailed knowledge of a priori data for the algorithm beyond the 400-700 nanometers range in order to be able to successfully deconvolve and cleanse the data. Another additive problem may be the signal recorded by the tales of the LEDs used to provide the minimal needed for estimation spectral knowledge. Specifically the 690 nanometers peaked LED, reaches beyond the visible spectrum and the signal is additively recorded in all channels due to the deliberate absence of a bandpass filter that blocks IR radiation. Moreover, the other LEDs additively add luminance to

the channels at nanometers beyond the theoretical bounds. The influence of these are recorded at the sensor and attempted to be removed by the algorithm. Quantitatively, it is shown that this deviation is removed at a satisfying degree, while in future studies and field application, the use of multiband pass filters instead of LEDs will provide less noisy data. The influence to the proposed algorithm that absence of these higher recorded intensities may have, need to be further investigated before arriving at a final conclusion.

4.5 Conclusion

Current technologies for real time spectral imaging are either at prototyping stage or involve employing high cost complex optomechanical parts. The Real Time Spectral Mapper, suggests a low cost alternative for real time spectral imaging, without complicated calibration processes or need for total control of the surrounding environment. It can provide full spectra within the visible range of the EMR in video rate. This enables for multiband imaging of dynamic phenomena. In the scope of this thesis, we examined and proposed on the fly theoretical training of the algorithm for spectral deconvolution and cross-talk phenomenon cleansing of the acquired frames. The suggested method is of high accuracy with low influence to the spectral imaging which can be further reduced after more detailed study.
In order for the algorithm to be applicable and to minimise noise, the spectral range of the light source needs to be known. In cases where the spectral bands incorporated in the cleansing coefficients are absent of light, integrity of the results is heavily compromised, for the algorithm will negatively influence the outcome in order to compensate for the missing bands.
Moreover, there exists noise within the coefficients when the light source is not of true flat response white, meaning if there are differences in the luminance intensity of each wavelength. Although creating such a light source is extremely hard, a priori knowledge of the spectrum of the light source can compensate and correct the deviation.

Knowledge of the full spectra in cases of chemometrics, can be fed to regression algorithms and after proper training provide full spectra of each of the chemical components that consist the solution. In turn, quantification of the level of absorption manifested by a spectrum can be directly correlated with concentration of that component. Since each pixel represent a spectral signature of a mixture and by the aforementioned methodology spectra for each component can be identified and correlated with a specific concentration, it is achievable to estimate a per pixel concentration of each chemical concentration and create pseudocolour maps (Figure 36) that represent these concentrations and assist by offering a more quantitative way of leukemia prognosis. More details on the formulation of these maps as well as their contribution are discussed in [32].
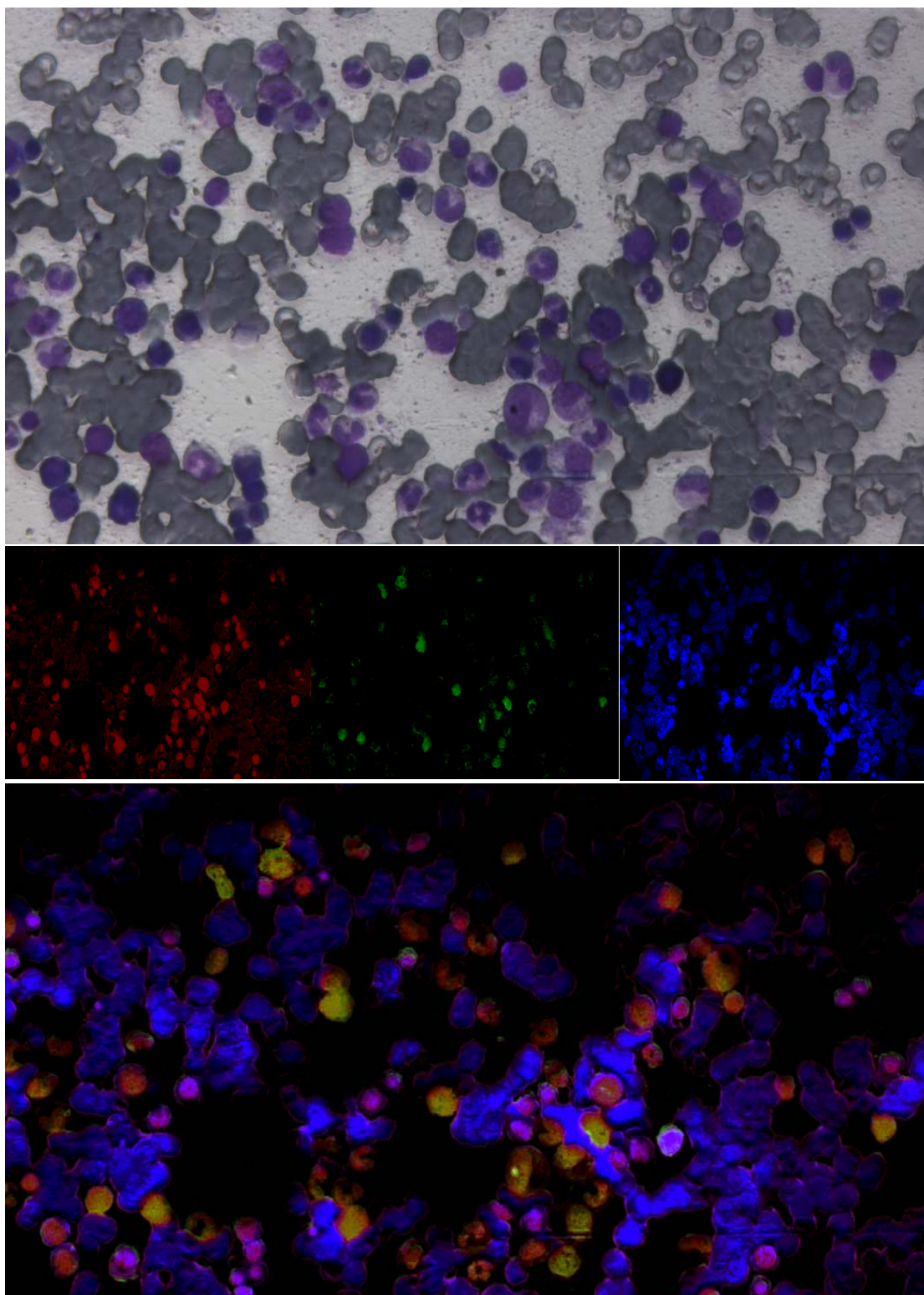
Figure 36 On the top, colour image of blood vessels of leukemia patients are presented as seen by examiners using a common microscope. Underneath primal pseudocolour maps of the concentration per pixel of the three stains used in the colour image are given, firstly for each stain and finally a composite pseudocolour map.

5.   Cervical Intraepithelial Neoplasia

Cervical cancer is one of the deadliest type of cancer affecting women globally [33] and poses a more serious threat in the developing world where 80% of the incidents occur [34], mostly due to lack of effective screening methods of detection of pre-cancerous conditions and their effective treatment before they progress to invasive cancer. During the last half century there has been recorded a cervical cancer deaths decrease of nearly 74%, mainly due to *Papanikolaou*[33], who improved the diagnosis process through the Pap smear screening. Leading causes of this type of cancer are four strains of the Human Papillomavirus (HPV). The cervical cancer type with the most incidences is squamous cell carcinoma. Other known subtypes, distinguished based on histology of the infected cells, are adenocarcinoma, adenosquamous carcinoma, small cell carcinoma, neuroendocrine tumor, glassy cell carcinoma and villoglandular adenocarcinoma [35, 36].
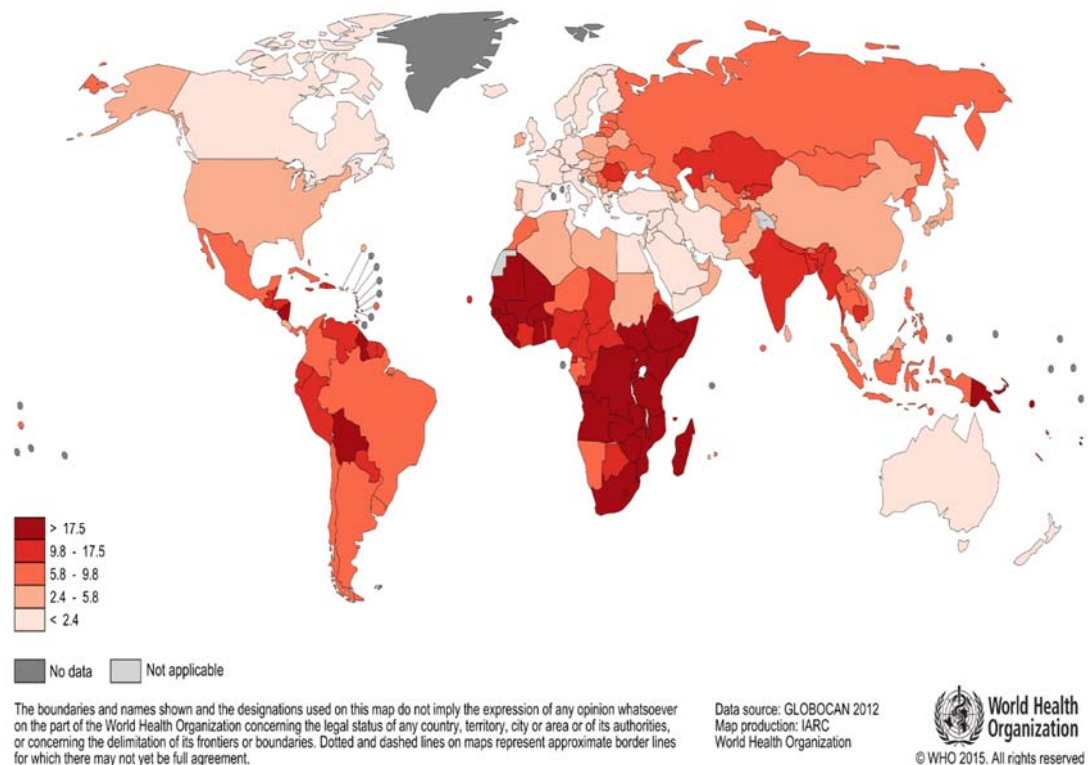
Figure 37 Age-standardised incident rates from Cervix Uteri cancer by country

In situ[1] cervical neoplasia, characterized as stage 0 by the International Federation of Gynecology and Obstetrics (FIGO), is treatable though lethal upon reaching stage IV. This treatable pre-invasive stage is called cervical intraepithelial neoplasia (CIN)

Based on the extent of cell abnormality, CIN is divided into three grades [37]:

- CIN1 indicates mild changes, affecting one third of the thickness of the epithelium layer of the cervix
- CIN2 indicates moderate dysplasia, affecting two-thirds of the thickness of the epithelium
- CIN3 indicates severe dysplasia to carcinoma in situ that spans more than 2/3 of the epithelium.

The aforementioned classification is used to indicate the volume of abnormal cells affecting the cervix.
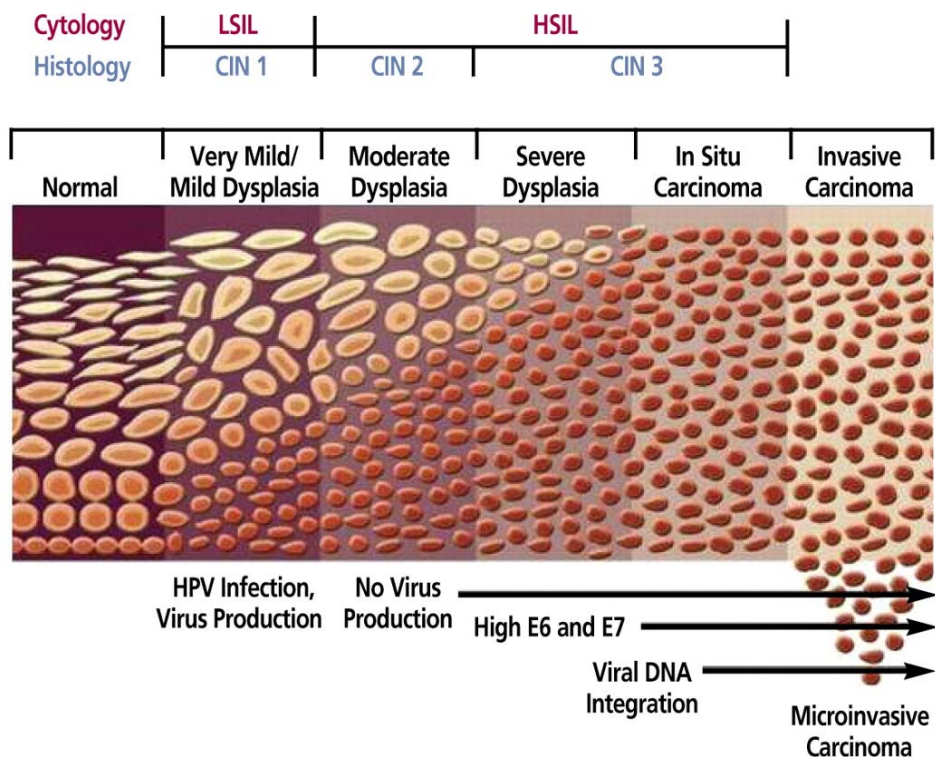
Figure 38 Cervical Epithelium structure in evolving rates of neoplasia

---

[1] In oncology *in situ* cancer means that malignant cells are present as a tumor but has not metastasized, or invaded, beyond the original site where the tumor was discovered

5.1 Diagnosis and Biopsy

Cervical cancer screening is attained through several tests such as the Pap smear (cytology), Visual Inspection with Acetic Acid, Visual Inspection with Lugol's Iodine and HPV testing. Only the Pap smear is applicable in large populations, reducing cervical cancer and mortality incidents globally [38]. For women with abnormal screening results colposcopy examination is performed, followed by biopsy sampling [39]. Colposcopy examination identifies tissue regions with most severe dysplasia in order to be sampled for biopsy [40, 41]. Colposcopy is critical, since its sensitivity and accuracy in identifying and sampling the region, determines the reliability of the diagnosis. It is based on visually observing the tissue through the colposcope (low magnification microscope) for the optical signal triggered after the application of acetic acid solution as a contrast agent, a phenomenon known as acetowhitening or by staining with Lugol's Iodine. As a rule, the induced optical effects are inherently very informative reflecting of the selective uptake of the contrast medium and of the reversible pharmacodynamics by the biomarker. The incorporation of the dynamic features of the bio-optical phenomena into the examination permit the creation of quantitative measures for the cancer-specific characteristics. In particular, if the correlation between the biomarker kinetics and the measurable dynamic optical signals is established, the estimation of quantitative traits, such as the functional and structural features of the abnormal areas, can be made possible. This enhancement may improve the sensitivity and specificity of the imaging modalities in the field. Traditional colposcopy practice suffers from subjectivity as it is highly based upon the visual prowess and training of the examiner, providing qualitative results. Therefore, colposcopy suffers from low sensitivity, high biopsy sampling error rate and disagreement in identification of cervical lesions [40 - 42].
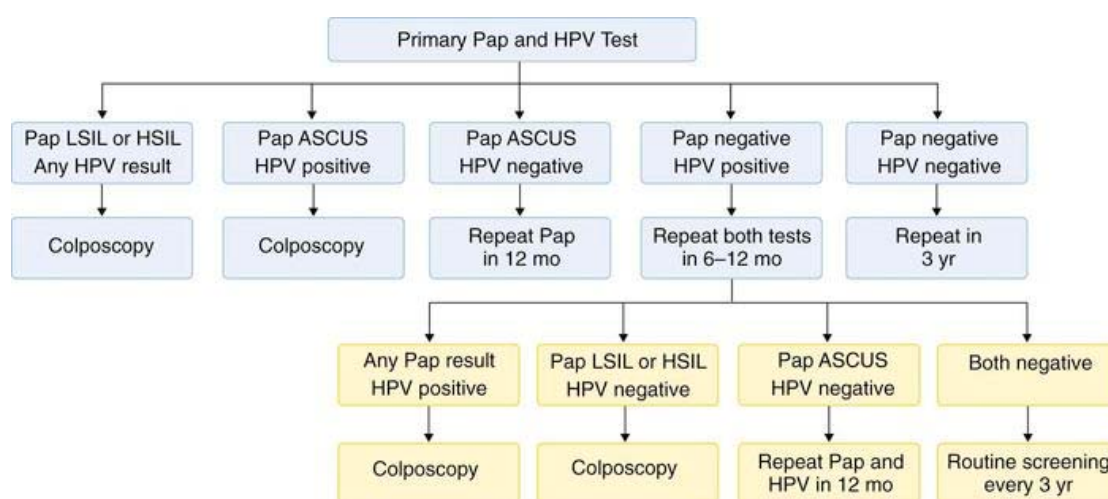
Figure 39 Typical Procedure following Test Pap based on findings of the test.

5.2   Acetowhitening Phenomenon

Infusion of acetic acid solution upon the epithilium, induces the acetowhitening phenomenon, which manifests at abnormal cells. The dynamic characteristics of the optical signal recorded during the pheomenon are directly related with both the perchentage of neoplastic cells in the tissue and their abnormal metabolic activities [43]. This correlation of backscattered light and the population of infected cells grants the capability of identifying the neoplasia stage (CIN I, II, III).

Glucolysis, taking place in the cytosol of cells,is a metabolic pathway where a glycose molecule is dissolved into pyruvate acid (1.1) and is the fundamental energy source for a cell.

$$C_6H_{12}O_6 \rightarrow CH_3COCOO^- + H^+ \quad (5.1)$$

Neoplastic cells reproduce faster than normal, thusly demanding more volumes of oxygen. Hypoxia forces pyruvate acid to disolves into lactic acid (1.2), which is emitted towards the extracellular space.

$$CH_3COCOOH \rightarrow 2C_3H_6O_3 \quad (5.2)$$
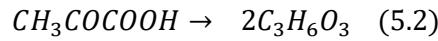
In order for a given, neoplastic or not, cell to sustain its functionality, it needs to have neutral pH value ranging from 7 to 7.5. This leads to acidic extracellular space around neoplastic cells, allowing slow accumulation of weak acids in the intracellular space, which are constantly ionized. The cellular membrane is impregnable to charged particles thus entrapping the ions within the cells ("ion trapping").

When infusing acetic acid in the tissue, it is instantly ionized producing salt and a hydrogen cation (1.3).

$$CH_3COOH \leftrightarrow CH_3COO^- + H^+ \quad (5.3)$$
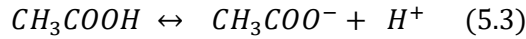
Ionization of the acitic acid is a duplex chemical reaction, thus governed by Le Ch$\hat{a}$telier 's principle (Equilibrium Law):

"If a chemical system at equilibrium experiences a change in concentration, temperature, volume or partial pressure the equilibrium shifts to counteract the imposed change and a new equilibrium is established."

Obeying this principle, acidic acid is passively diffused unionized inside neoplastic cells, where pH regulation mechanisms of the cell kick in.

As a result, there is high concentration of hydrogen cations, which transubstantiate the proteins inside the cellular core, altering the scattering characteristics of the core, thusly manifesting a different EMR-tissue interaction. This is a reversible procedure and within few moments the tissue regains its original characteristics once intracellular pH levels return to normal.

5.3 Dynamic Spectral Imaging System
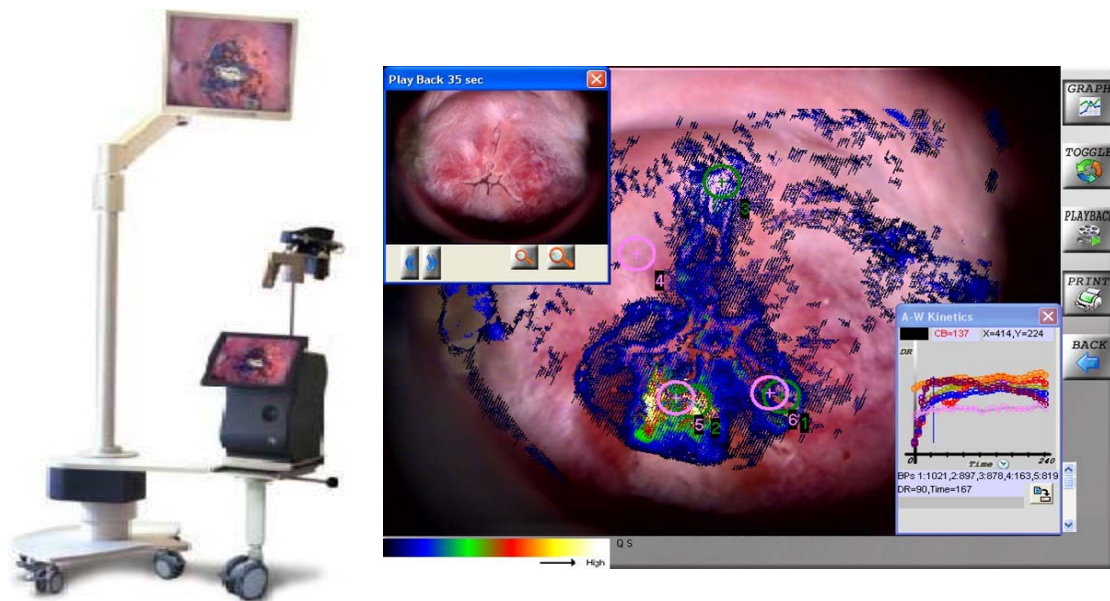
Figure 40 On the left is the Dynamic Spectral Imaging System. On the right is a typical output pseudocolour mapping of the cervix by the system

Dynamic contrast enhanced (DCE) imaging has emerged over the past decade as a promising method for diagnosis, grading, staging, new drug development and evaluation of treatment effectiveness [43]. In principle, DCE imaging is a technique able to capture the spatio-temporal, biomarker-induced, bio-events and processes in tissues, *in vivo*, non-invasively and in real time. Owing to these features, DCE imaging has been established as a non-surgical tool for the study of tissue perfusion kinetics and has shown an impressive prognostic and predictive capacity in cancer radiology [44 - 46]. The concept of DCE continues to evolve rapidly and has been translated to several biomedical modalities including optical imaging. In fact, the *in vivo* optical imaging aspect of DCE (DCE-OI) was established in late nineties [47, 48]. Particularly, a DCE optical imaging method and platform was developed for measuring and mapping the evanescent backscattering signals [49] in pursuit of more accurate screening methods.

Thusly, the Dynamic Spectral Imaging System was created. The DySIS™ integrates an optical imaging head supported by a mechanical base. The base incorporates weight counters and space translating mechanisms, permitting easy manual positioning of the optical imaging head. Moreover, there are both mechanical and electromagnetic brakes, manually activated through a trigger, once positioning that provides the optimum field-of-view has been achieved. In order to maintain approximately the same field-of-view throughout the entire examination procedure, the optical imaging head is detachably connected through a mechanical shaft attached to a vaginal speculum.

The optical head is configured to capture images from a 23mm X 20mm tissue area, including the entire transformation zone of the cervix. Assuming an average 35µm cell diameter and given the spatial resolution of the sensor, the backscattered light intensity recorded by a given pixel can easily be calculated as corresponding approximately to the area occupied by a single cell.

The initiation of the image capturing process is triggered by application of the acetic acid, in order to ensure synchronization between the phenomenon and the image acquisition process. A reference image is captured prior to the application of the acetic acid solution, followed by

automatic image capturing during the evolution of the AW phenomenon. The captured images are then aligned using an embedded registration algorithm, in order to compensate for both image translations and deformations, caused by tissue's contractions and patient's movement respectively. Temporal knowledge of the target aids in glares recorded despite hardware and optics added to remove such effects. From the captured images stack, and particularly, from the green channel, the diffuse reflectance (DR) curves are calculated for every image pixel, expressing the temporal response of the AW phenomenon. Based on the DR curves, a series of features are then calculated, such as time integral, DR peak value (DR_{max}) etc. A pseudocolour map is then generated, with different colours representing different feature values, which is overlaid onto the real-time displayed colour image of the cervix.

The greatest advantage of DySIS™ is elimination of subjectivity inherent in current diagnostic procedures (cytology and colposcopy), providing an additional quantitative measurement as aid to the diagnosis. Therefore, incorrect diagnoses of lesions are minimised. DySIS™ performs a rapid, quantitative and side effect-free examination procedure to provide in-vivo topography of the lesion. As such, DySIS™ technology is emerging as an indispensable tool for the diagnosis, screening and follow up, and for the on-line guiding of biopsy sampling and surgical treatment.

5.4 Clinical Studies

Two independent, large clinical studies took place in order to test DySIS™, resulting into peer-reviewed publications. All eligible members of the validation group had an abnormal pap-test and had been referred for colposcopy. The diagnostic performance of DySIS™ was compared against cytology (Pap test) and colposcopy, using histology as the ground truth. There was no interference between the DySIS™ scan and the operator's assessment, since the grading of the lesion was performed in an automated basis, according to the protocol.

The first clinical trial [50] took place in the colposcopy clinics of Hammersmith Hospital and St Mary's Hospital, London, United Kingdom and at the Alexandra Hospital, Athens, Greece. Initially, 529 women were recruited; of those, 82 were recruited to the training group. The remaining 447 women were recruited to the test group. 139 women of those were excluded, leaving only 308 women eligible.

The aim of the second clinical trial [51] was to examine whether the performance of DySIS™ would be further improved by combining both DySIS™ and conventional colposcopic examination. The trial took place in three Dutch Hospitals; the VU University Medical Centre in Amsterdam, the Reinier de Graaf Hospital in Voorburg and the St. Antonius Hospital in Nieuwegein. In total 275 women were included in the study.

5.4 Epithelium

5.4.1 Structure and Morphology of the epithelium

A layer of cells known as the epithelia surrounds inner body cavities and many organs. A main function of the epithelium is acting as a protective barrier. Thusly epithelial cells are contiguous and joined together by special junctions. In general, intercellular space between epithelial cells is limited. Depending of the functionality they serve epithelial tissue can be impermeable (*eg*. skin) or absorbent (*eg*. epithelium lining the intestine). Some have secretory functions (*eg*. glands) while others actively participate in metabolism (*eg* endothelial cells lining blood vessels). All are attached to the underlying tissue through a basement membrane, which in general is not identifiable by light microscope due to its thin nature, and have a free surface, to which there is no cellular or extracellular elements attached.

The epithelium can be classified in a number of ways.

- by the number of cellular layers
    - *Simple*. A single layer epithelium
    - *Stratified*. Two or more layers
- by the cellular shape
    - *Squamous*. The cells have assumed a flattened shape
    - *Cuboidal*. Cells of same height, width and depths
    - *Columnar*. The cellular height exceeds width

In stratified epithelia where cells are of different shapes the classification is based upon the outermost layer, which is the free surface.

In the scope of this thesis, we focus on epithelial neoplasia mainly occurring in the cervix of the uterus, where epithelial tissue is either simple columnar or stratified squamous, depending on the cervix region they cover.

The cervical epithelium, depending on the stage of neoplasia it has progressed, undergoes fundamental structural transformations. Accurate cytological diagnosis is based on the distinction of cancer to normal cells by light microscopy, by distinction of these differences between neoplastic and normal cells.
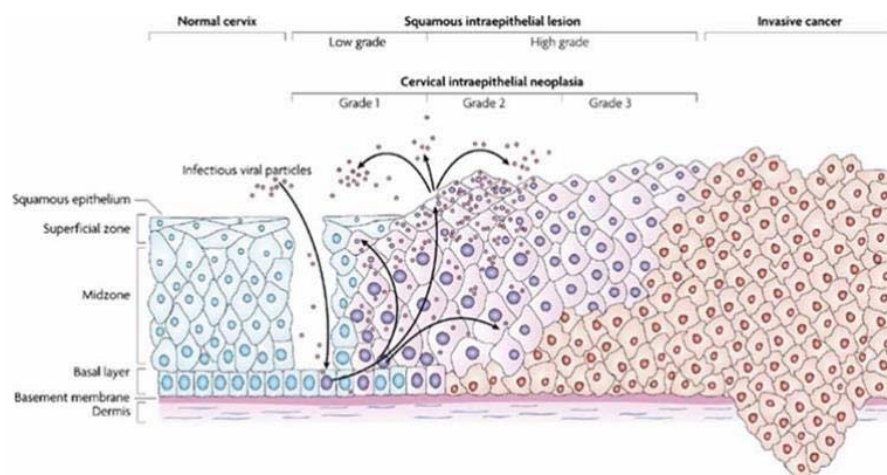
Figure 41 Cell packaging in the epithelium based on grade of neoplasia

HPV virus, like any virus penetrates the cells and exploits their genetic mechanism in order to multiply. If not suppressed by the immune system or treated by medication, infection evolves to inflammation. When the inflammation firstly develops, it is confined at the layers of the epithelium hence the term Cervical Intraepithelial Neoplasia. Mitosis contribute in creation of new infected by HPV cells. In normal tissue each cell, based on the layer it participates, has a certain form and size. When neoplasia begins, regardless of the cellular layer, the form and size of infected cells begins to assume a certain shape and volume. This results in generating homogenous epithelium as CIN stages progress. Nucleus size is also significantly different; a lesion named anisonucleosis, and at the same time the nucleus shape is varying than in normal state. In HSIL there can also exist cells with multiple nucleus. Moreover, coarse granular chromatin[2] is unevenly distributed throughout the nucleus and is often increased. The amount and distribution of chromatin varies due to the abnormal cell division. Hyperchromasia is observed on neoplastic cells due to common reflecting increased chromatin and/or rapid cell turnover[3]. These differences are caused by errors in mitosis, which normally is an ability only the basal layers of the epithelium have. Pap test is based on the distinction between normal, precancerous and cancerous epithelium. The distinction between stages of CIN is made upon the population size of neoplastic cells. Epithelia cellular homogeneity can be observed throughout the epithelium (CIN III) or may differ from the basal layer to the free surface. Abnormal nuclei in superficial or intermediate cells indicate a low-grade CIN, whereas abnormality in nuclei of parabasal and basal cells indicates high-grade CIN. High grade CIN are likely to have a greater proportion of the thickness of epithelium composed of undifferentiated cells, with only a narrow layer of mature, differentiated cells on the surface.

5.4.2 Tight Junctions

Tight junctions are junctions that connect adjacent cells and control the paracellular substance exchanges. The tight junction pores are dynamic ion channels. Studies have shown that during neoplasia the tight junctions are reduced, thus allowing the creation of gaps in the epithelium, and allowing greater infusion of ions and molecules.

---

[2] Chromatin is the combination of DNA and proteins which consists the contents of the cellular nucleus.
[3] Cell turnover is a term referring to the replacement of old cells with newly generated ones.

5.5. Biological Model

5.5.1 Compartmental modeling

5.5.1.1 Basic Principles

In general, models are used to describe functions of the real world. In mathematical modeling that description is translated into mathematics. The most commonly used method to describe products of chemical reaction and nutritious substances in based on compartmentation. The tissue is divided into sequential compartments and the substance fluxes are translated in mathematical equations. A compartment in biological systems is considered a common block of cells with the same structural and functional characteristics. Many compartments can coexist in the same region of a living organism.
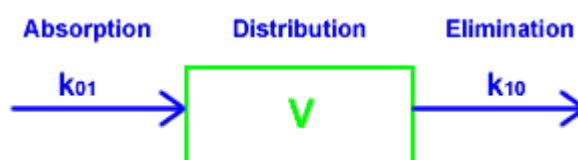
Figure 42 Single Compartment model

5.5.1.2 Single Compartmental modelling of tissues

The simplest application of compartmental modeling is in observing a single compartment. A single compartment can be considered the equivalent of a single cellular layer. The concentration of the solution, C, infused inside a compartment through time, can be described by a single differential equation

$$\frac{dC}{dt} = \frac{Input(t) - (CL * C)}{V} \qquad (5.4)$$

Where:

- CL is the rate of infused solution elimination divided by plasma concentration, giving a volume of plasma from which the solution is completely removed per unit of time,
- V is the volume of the compartment.

5.5.1.3 Multi Compartmental modelling of tissues
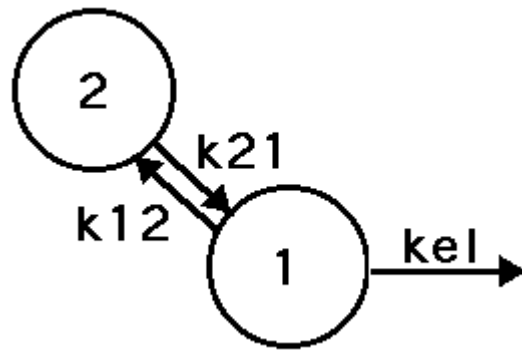
Figure 43 Two Compartment Pharmacokinetics Model

In multi compartmental modeling many distinct compartments are used to describe different structural or functional regions of tissue and the connections between the compartments are represented [53]. The arrows connecting each compartment denote the mobility orientation and the amount of substance moved is denoted usually as *k(i, j)* or *L(i, j),* where *i* is the compartment of origin and *j* the target compartment. The function of a single compartment is described by a balance of the mass of the form:

$$\frac{dQ_i}{dt} = \sum R_{ij} - \sum R_{ji} \quad (5.5)$$

Where, $\sum R_{ij}$ is the sum of the mass flux rates from compartment *i* to compartment *j*.

The transaction is possible either by a chemical reaction or by natural transport. As a result of sequential positioning the amount of a substance entering a given compartment is less than the one that entered the previous and more than the one following. Differential equations are used to describe a change of state over a time span.

A model is considered linear, when all values of the parameters of the equations are either constants or time functions. A model is considered on the other hand as non-linear, when at least a single transport factor is a size function of at least one compartment. The capability of describing a system as a compartmental model depends on its characteristics and is valid only if the substances consisting different compartments and the exchanges occurring are clearly discrete. The transaction time rates need to be constant throughout the simulation, for consistency to be maintained. Any alteration of the substance being studied that occurs inside a compartment is considered instant compared to the time needed for the transaction.

5.5.2 Biological Model of Neoplastic Cervical Epithelium

The mathematical model developed in [54] is based in multi-compartmental modeling and provides an accurate description of the biological procedures during infusion of acetic acid in the epithelium of the cervix. Each compartment represents a single cellular level. The number of compartments depends on the stage of CIN, low in number in cases of CIN I with the number rising as the CIN progress. Each compartment is divided into two smaller ones, one for the intracellular space (IS) and one for the extracellular space (ES). Altogether, the developed model is a deterministic, non-linear, algorithm that includes a scalable system of coupled differential equations. The differential equation system expresses material exchange between the compartments of a single neoplastic layer.

The developed model simulates the AA motion from the first neoplastic IS to its surrounding ES and vice versa for each dysplastic cellular layer and from there to the next level.
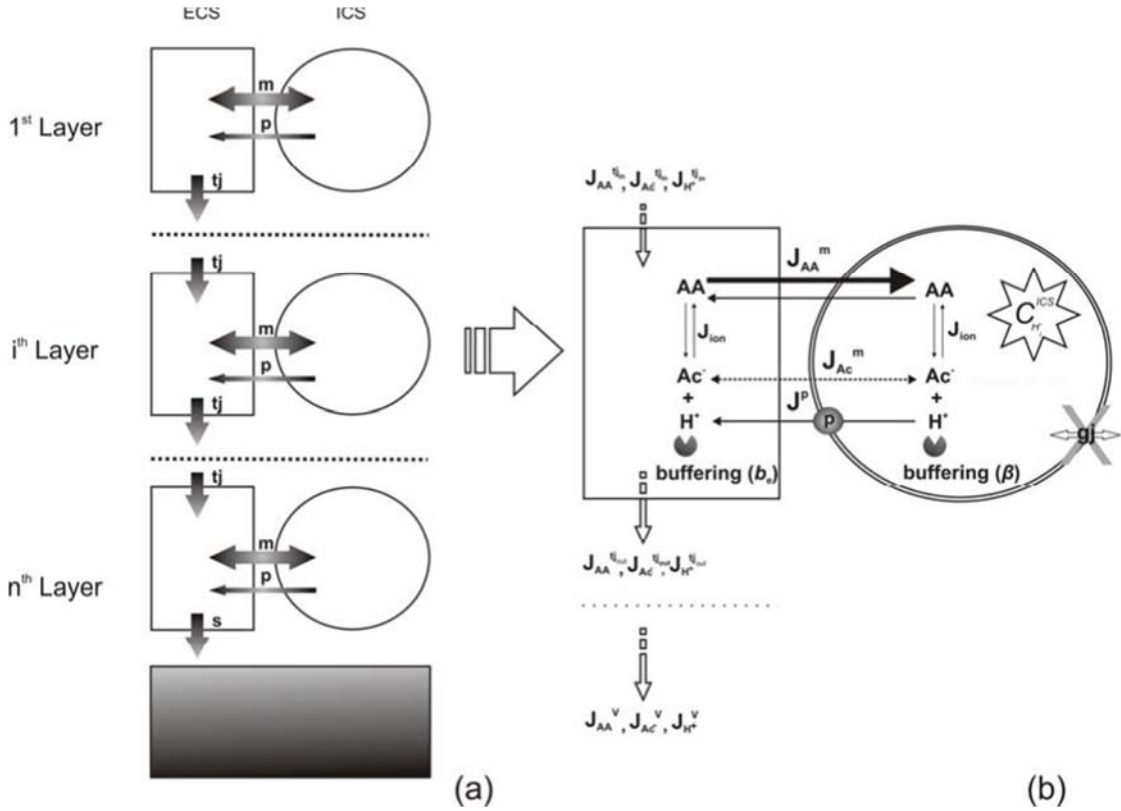
Figure 44 (a) Epithelial compartments and transport fluxes (b) The two-compartment cell model and transport fluxes

In Figure 44 (a) is shown the flow diagram of the biomarker through multiple compartments, clearly depicting the transport fluxes in and out of each compartment. Exchange of mass of the biomarker is permitted by passive infusion through the cellular membrane (m) and by active ion flux (p). Intercellular communication is achieved by passive electroosmotic infusion, through the membrane of the tight junctions that exist between each compartment and its adjacent upper and lower cellular levels.

In Figure 44 (b) the communication of intra- with extracellular space is more clearly represented. Acetic acid, anions of acetic acid (Ac^-) and cations of hydrogen (H^+) enter the extracellular space from the upper cellular level through the tight junctions ($J_{AA_i}^{tj_{in}}, J_{AC_i}^{tj_{in}}, J_{H_i}^{tj_{in}}$). The acetic acid (AA) is ionized (J_{ion}) depending on the extracellular pH (pH_{ES}) and the extracellular buffering capability (β_{ES}). As a result of the AA ionization pH_{ES} drops and the hydrogen buffering mechanisms are activated. Molecules of acetic acid are passively diffused through the cellular membrane towards IS. The molecules that entered the cell undergo the same reactions resulting on the same results, drop of intracellular pH value (pH_{IS}) and activation of the hydrogen buffering mechanisms of the cell (β_{IS}). Differences between pH$_{IS}$ and pH$_{ES}$ create a weak conductivity field that allows infusion of Ac$^-$ ($J_{AC_i}^m$). Once the intracellular hydrogen concentration ($C_{H_i}^{IS}$) rises, the proton pumps of the cell (J^p) are activated actively defusing H$^+$ out of the cell. Anions of acetic acid and cations of hydrogen still remaining within the cell are joined together again into neutral acetic acid. After this process concludes its cycle, residual molecules and ions in the extracellular space are diffused through the tight junctions ($J_{AA_i}^{tj_{out}}, J_{AC_i}^{tj_{out}}, J_{H_i}^{tj_{out}}$) into the next compartment beginning a new cycle of the biochemical process, as was just described.

5.5 Mathematical Model of Neoplastic Cervical Epithelium

5.5.1 Introduction to the differential equations of the model

Epithelial dysplastic layers

$$n = \sum_{i=1}^{4} \frac{90}{h_i} \quad (5.6)$$

The total *number of epithelial layers*, N, for each CIN grade is estimated by (5.6) where n is the total number of layers and h_i is the cell height for each epithelial section. The constant value 90 is calculated by dividing the proven cervical epithelial depth (360µm) by the number of different epithelial section, after making the assumption that each of the four different epithelial sections (basal, parabasal, intermediate and superficial) span equally sized areas.

Acetic acid ionization (J_{ion})

AA ionizes following (5.3) chemical equation and is subjugated to k_1 and k_2, forward and backward dissociation rates, respectively. According to the mass action law, the rate which AA is ionized is

$$J_{ion} = -k_1 C_{AA}(t) + k_2 C_{AC^-}(t)\, C_{H^+}(t) \quad (5.7)$$

where *C(t)* is the concentration of the biomarker at a given time. Based on the acute nature of AA it is considered as being constantly at chemical equilibrium. As a result, for $J_{ion} = 0$, at which steady state is assumed *the AA dissociation constant K_a subjugates to the following function:*

$$K_a = \frac{k_1}{k_2} = \frac{C_{AC^-}(t) C_{H^+}(t)}{C_{AA}(t)} \quad (5.8)$$

The model assumes that AA kinetics is constantly in equilibrium. Based on that, solid state (ss) of passive diffusion between two adjacent compartments is governed by Fick's Law resulting in the function:

$$J_{AA}^{pm_{1\to 2}} = -\frac{Dk_S}{d}\, C_{AA}^{1} \overset{ss}{=} P_{AA}^{pm}\,(C_{AA}^{1} - C_{AA}^{2}) \Leftrightarrow$$

$$-C_{AA}^{1} = \rho_1 P_{AA}^{pm}(C_{AA}^{1} - C_{AA}^{2}) \qquad (5.9)$$

where D is the AA diffusion factor, k_S the AA factor in aquatic environment, d the length of the pores, P_{AA}^{pm} the membrane permeability and ρ_1 the ratio of area to volume. The rates of concentration changes in (3.6) are given by the equations:

$$\dot{C}_{AA_i}^{IS} = -\rho_{IS}J_{AA_i}^{m} = -\rho_{IS}P_{AA}^{m}\big(C_{AA_i}^{ES} - C_{AA_i}^{IS}\big) \qquad (5.10)$$

$$\dot{C}_{AA_i}^{ES} = -\rho_{ES}J_{AA_i}^{m} = -\rho_{ES}P_{AA}^{m}\big(C_{AA_i}^{IS} - C_{AA_i}^{ES}\big) \qquad (5.11)$$

where ρ_{IS} ,ρ_{ES} are the area/volume ratios of the intracellular and extracellular space and P_{AA}^{m} is the diffusion coefficient of AA through the cellular membrane. In cases of small pores, as is those of the tight junctions (4.9 to $7\hat{A}$), and due to the relative size of AA molecules ($3\hat{A}$) diffusion is considered as hindered diffusion. According to the Renkin's Law the permeability of the hindered diffusion is described as:

$$P_{AA}^{H} = \frac{N\pi r^2 D_{AA}^{bulk} F(a/r)}{d * \frac{1-\frac{a}{r^2}}{1-\frac{a_w}{r^2}}} \qquad (5.12)$$

where P_{AA}^{H} is the hindered diffusion of AA, N the number of pores, D_{AA}^{bulk} the bulk solution diffusion factor of AA, d the length of the pore, a_w the molecular diameter of water and a factor between AA and the walls of the tight junctions, $F(a/r) \approx 1-2.1044(a/r)+2.089(a/r)^3-0.948(a/r)^5$. For a given cellular level i, the rate of AA concentration in ES from the previous level towards the next is:

$$\dot{C}_{AA_{tj_i}}^{ES} = \rho_{ES}(J_{AA_i}^{tjin} - J_{AA_i}^{tjout}) = -\rho_{ES}P_{AA}^{H}\big(C_{AA_{i-1}}^{ES} - 2C_{AA_i}^{ES} + C_{AA_{i+1}}^{ES}\big) \qquad (5.13).$$

Ions are infused also due to electrical fields appearing due to the pH difference. Assuming that the electrical field that has been generated in between the two sides of the cellular membrane is stable, the Goldman-Hodgkin-Katz assumes the form:

$$J^{I \to II}_S = \frac{z_S FDV}{RT} P_S C^I_S - \frac{C^{II}_S e^{\frac{z_S FDV}{RT}}}{1 - e^{\frac{z_S FDV}{RT}}} \Leftrightarrow \dot{C}^{II}_S = \rho J^{I \to II}_S \quad (5.14)$$

where z is the valence, F the Faraday's constant, R gas constant, T the temperature, index S denotes the diffusing ion (H$^+$ or Ac$^-$), ρ is the volume/area ration of the diffusing compartment and C^I, C^{II} are respectively the concentrations of compartment I and II (positive flux from I to II).

Despite the cations over anions discrimination in tight junction pores, a common channel resistance policy is adopted for the developed model and Ac$^-$ diffusion is considered hindered based on the molecular dimensions. Using (5.12) the ions concentration change rates of IS and ES at any given layer is:

$$\dot{C}^{ES}_{S_{tj_i}} = \rho_{tj}(J^{tj_{in}}_{S_i} - J^{tj_{out}}_{S_i}) = -\rho_{tj} \frac{z_S FDV_{tj}}{RT} P^H_S \left(\frac{C^{i-1}_S - C^i_S e^{\frac{z_S FDV_{tj}}{RT}}}{1 - e^{\frac{z_S FDV_{tj}}{RT}}} - \frac{C^i_S - C^{i+1}_S e^{\frac{z_S FDV_{tj}}{RT}}}{1 - e^{\frac{z_S FDV_{tj}}{RT}}} \right) \quad (5.15).$$

Assuming similar formulation is applied in passive ion diffusion through the cellular membrane, the rates of Ac$^-$ in IS and ES due to electrodiffusion of the membrane is:

$$\dot{C}^{IS}_{Ac^-} = -\rho_{IS} J^m_{Ac^-} = -\rho_{IS} \frac{(z_{Ac^-})FDV_m}{RT} P^m_{Ac^-} \frac{C^{ES}_{Ac^-} - C^{IS}_{Ac^-} e^{\frac{(z_{Ac^-})FDV_m}{RT}}}{1 - e^{\frac{(z_{Ac^-})FDV_m}{RT}}} \quad (5.16)$$

$$\dot{C}^{ES}_{AA_i} = -\rho_{ES} J^m_{Ac^-} = \rho_{ES} \frac{(z_{Ac^-})FDV_m}{RT} P^m_{Ac^-} \frac{C^{IS}_{Ac^-} - C^{ES}_{Ac^-} e^{\frac{(z_{Ac^-})FDV_m}{RT}}}{1 - e^{\frac{(z_{Ac^-})FDV_m}{RT}}} \quad (5.17)$$

The fraction of unionized AA ($C^{IS}_{AA_T}$) is given by the formula:

$$a = C^{IS}_{H^+_i} / (C^{IS}_{H^+_i} + K_a) \quad (5.18)$$

Thus in (3.12) the number of variables can be reduced by the use of:

$$C^{IS}_{Ac^-} = (1 - a)C^{IS}_{AA_T} \quad (5.19)$$

Acetic acid extrusion from the cells and stroma diffusion are unidirectional, proportional to the concentration of the native diffusing solute and to its perfusion rate through the membrane.

$$J = kC_S \qquad (5.20)$$

is used to describe the fluxes in the most simplistic circumstances, where k is a proportionality constant (cm/sec) and C_S is the concentration of transported solute. The concentration change rates by a generic pump $\dot{C}_{H^+_p}$ and stroma diffusion $\dot{C}^{ES}_{Sv}$ are described by:

$$\dot{C}_{H^+_p} = \rho_p J^p_{H^+} = k_p C^{IS}_{H^+} \qquad (5.21)$$

$$\dot{C}^{ES}_{Sv} = \rho_V J^V_S = k_V C^{ES}_S \qquad (5.22)$$

where k_p, k_V are the proportionality constants, ρ_p and ρ_V are the area/volume ratio of pump and stroma respectively and S the diffusing AA, Ac⁻ and H⁺.

Differential equation system of the model

As described in Chapter 1.3, the AW dynamics are proportional to the pH_{IS} dynamics. This lead to the model equations to be developed, with the purpose of providing pH_{IS} as output.

These dynamic characteristics ($\dot{C}^{IS}_{H^+_p}$), as well as the total AA concentration ($\dot{C}^{IS}_{AA_p}$), are described by the following differential system:

$$\dot{C}^{IS}_{H^+_p} = -\ln 10^{C^{IS}_{H^+_p}} \rho_{IS}\left((1-a_i)J^m_{AA_i} - a_i J^m_{Ac^-_i}\right) - J^p_{H^+} \qquad (5.23)$$

$$\dot{C}^{IS}_{AA_i^T} = \rho_{IS} J^m_{AA_i} + \rho_{IS} J^m_{Ac^-_i} \qquad (5.24)$$

where $\ln 10^{C^{IS}_{H^+_p}}$ is a factor describing the conversion of pH to H⁺, ρ_{IS} is the cell area/volume ration (A_{cell}/V_{cell}) and β is the intracellular buffering power of a solution. ($\beta = dC^{IS}_{H^+_i}/dpH_{IS}$).

The equivalent system for the ES is:

$$\dot{C}^{ES}_{AA_i} = \rho_{tj}\left(J^{tjin}_{AA_i} - J^{tjout}_{AA_i}\right) + \rho_{ES} J^m_{AA_i} + J_{ion} \qquad (5.25)$$

$$\dot{C}^{ES}_{Ac^-_i} = \rho_{tj}\left(J^{tjin}_{Ac^-_i} - J^{tjout}_{Ac^-_i}\right) + \rho_{ES} J^m_{Ac^-_i} - J_{ion} \qquad (5.26)$$

$$b_{ES} \dot{C}^{ES}_{H^+_i} = \rho_{tj}\left(J^{tjin}_{H^+_i} - J^{tjout}_{H^+_i}\right) + \rho_{ES} J^m_{H^+_i} - J_{ion} \qquad (5.27)$$

where ρ_{ES} and ρ_{tj} are the area/volume ratio of the ES and the tight junctions respectively, b_{ES} is a proportionality constant defined by the ratio of the ionized/non-consumed protons in the ES. Regarding the last layer, $\rho_{tj}J^{tjout}_{AA_i}$, $\rho_{tj}J^{tjout}_{Ac^-_i}$, $\rho_{tj}J^{tjout}_{H^+_i}$ are substituted by the terms $k_V J^V_{AA_i}$, $k_V J^V_{Ac^-_i}$, $k_V J^V_{H^+_i}$ respectively.

The differential system, as described above, results in high computational cost. It is desirable to reduce computational cost without sacrificing accuracy. A stricter observation of the parameters of the model reveals two kinds of kinetics during the AW phenomenon, the slow and fast kinetics procedures. In order to simplify the model the Rapid Equilibrium Approximation method was applied, resulting in expunging J_{ion} from the differential equations and reduced the number by one. By setting

$$X_i = C_{AA_i}^{ES} + C_{Ac_i^-}^{ES} \qquad (5.28)$$

$$Y_i = C_{H_i^+}^{ES} - C_{Ac_i^-}^{ES} \qquad (5.29)$$

And by differentiating (3.25) and (3.26), the result is the sum of (3.22) and (3.23) for the first and the subtraction of (3.24) from (3.23):

$$\dot{X}_i = \rho_{tj}\left(J_{AA_i}^{tj_{in}} - J_{AA_i}^{tj_{out}}\right) + \rho_{ES}J_{AA_i}^{m} + \rho_{tj}\left(J_{Ac_i^-}^{tj_{in}} - J_{Ac_i^-}^{tj_{out}}\right) + \rho_{ES}J_{Ac_i^-}^{m} \qquad (5.30)$$

$$\dot{Y}_i = \rho_{tj}\left(J_{H_i^+}^{tj_{in}} - J_{H_i^+}^{tj_{out}}\right) + J_{H_i^+}^{p} + \rho_{tj}\left(J_{Ac_i^-}^{tj_{in}} - J_{Ac_i^-}^{tj_{out}}\right) - \rho_{ES}J_{Ac_i^-}^{m} \qquad (5.31)$$

The following differential equation system is created for each neoplastic layer [55]:

$$\dot{C}_{TA_i}^{IS} = a^{-1}(J_{AA_i}^{m} + J_{Ac^-}^{m}) \qquad (5.32)$$

$$\dot{C}_{H_i^+}^{IS} = -\ln 10^{C_{H_p^+}^{IS}} \alpha\beta_{IS}\left(q_i^{IS}J_{AA_i}^{m} - w_i^{IS}J_{Ac_i^-}^{m} - J_{H_i^+}^{p}\right) \qquad (5.33)$$

$$\dot{C}_{TA_i}^{ES} = b^{-1}J_{AA_i}^{m} + b^{-1}J_{Ac^-}^{m} + a^{-1}\varepsilon J_{AA_i}^{tj} + b^{-1}\varepsilon J_{Ac^-}^{tj} \qquad (5.34)$$

$$\dot{C}_{H_i^+}^{ES} = -\ln 10^{C_{H_i^+}^{IS}} \beta_{ES}^{-1}[q_i^{ES}\left(b^{-1}J_{AA_i}^{m} + a^{-1}\varepsilon J_{AA_i}^{tj}\right) - w_i^{ES}\left(b^{-1}J_{Ac_i^-}^{m} + a^{-1}\varepsilon J_{Ac_i^-}^{tj}\right) + b^{-1}J_{H^+}^{p} + a^{-1}\varepsilon J_{H^+}^{tj}]$$
$$(5.35)$$

where the dot ($\cdot$) denotes the time derivative, *TA* is the total AA concentration, in both ionized and unionized form, *i* is the ith neoplastic layer (*i=1,2,…,N*), *q* and *w* account for the dynamic ionization constants of AA, including its self-burning effect. The developed differential equation system is solved numerically with the aid of a mixed-integer, nonlinear algorithm. It should be noted that the reservoir layer equations (3.31) and (3.32) are abolished and for the last layer the outgoing paracellular flux is replaced by the K_VC term, where K_V is the permeability at the boundary between the epithelium and the stroma and C corresponds to the concentration of either AA, Ac– or H$^+$.

5.6 Global Sensitivity analysis, parameter identifiability and estimability

As mention before pH_{IS} over time is produced as output of the model. That is graphically depicted as a curve of intracellular H^+ versus time. Information on all structural and functional biological parameters, that determine the AA pharmacokinetics through the epithelial and are related to neoplasia, is contained in the model predictions. Under an idealized, *in silico*, environment Global Sensitivity Analysis (GSA), parameter identifiability and parameter estimability has been performed [55]. GSA provides an estimate to the sensitivity of the output towards the variations of the input parameter. The GSA outcomes was used as input for both parameter identifiability and parameter estimability. A given parameter is considered as identifiable when its respective sensitivity function is neither null nor collinear with the sensitivity function of another parameter. In parameter estimability analysis the level of interactions and/or correlations between the identifiable parameter sets was defined. Based on these studies the parameters were ranked with the purpose of reducing the dimensionality of the inverse problem that is described in Chapter 6. The parameters, which display high sensitivity, no collinearities and minimum interdependency with other parameters, are considered as the key determinants of the bio-optical dynamic characteristics. Moreover, parameters that do not fulfil these criteria can be considered as non-identifiable and are kept constant at their nominal values. An initial nine input parameters of the model was reduced to four most identifiable and estimable ones.

Finally, the value ranges of the set of neoplasia related biological parameters, as measured experimentally are shown in Table 9.

Table 9 Value Range of biological parameters

Parameters	Description	Lowest value	Highest value
N	dysplastic cellular layers number	1	10
b	ES linear dimension	$4 * 10^{-7}$	$8 * 10^{-7}$
pH$_{ES}$	pH value of ES	6	7
ε	tight junctions' porosity factor	$0.7 * 10^{-9}$	$3 * 10^{-9}$

These parameters were deemed most identifiable after the analyses where completed. These parameters are all structural and functional parameters that have identified to directly correlate with existence and progress of cancer.

- N is the discrete number of dysplastic cellular layers. As cancer progress in stages, the number of dysplastic cellular layers increase.
- B expresses in continuous values the area of the extracellular space. Cancerous cells are mole loosely connected thus the distance between them increases.
- pH$_{ES}$ is the value of pH in the extracellular space. Studies have shown that cancerous cells are surrounded by acidic environment.
- ε is the factor that depicts the ability of the tight junctions between cells to allow movement of ions, expressed in continuous values by this parameter.

These parameters are of outmost importance in clinical practice where *N* and *b* are the key parameters upon which routine histological grading of biopsies is based; pH$_{ES}$ is strongly linked with the ability of tumor cells to form invasive cancers; and *ε* represents the tight junction porosity changes due to malfunction at neoplasia. It is essential to stress here, that pH$_{ES}$ and *ε* are functional parameters that cannot be assessed *in vivo* by any medical procedure known thus far.

6 Inverse problem

Even though the systematic, theoretical reduction of the model is expected to enhance the well-posedness of parameter estimation problem, it does not prove existence, uniqueness, and continuous dependence of the solution to the parameter values. To establish this a practical confirmation of the *a priori* analyses mentioned earlier is required, by efficient and mathematically rigorous estimation methods.

The first step towards this direction is to state the inverse problem as the minimization of a cost function that calculates the goodness of the fit between the model output and a given experimental data set, subject to the dynamics of the system [56].

6.1 Stating the inverse problem

An *inverse problem* is a term used to describe a problem in which the observed measurements are attempted to be convert into information about a physical problem or system. Thusly, dynamic optical data, in form of curves depicting concentration of hydrogen within the cytoplasm of the epithelium and obtained during screening were fitted towards outputs of the model, in order of asserting the values of the aforementioned, both structural and functional, biological parameters.
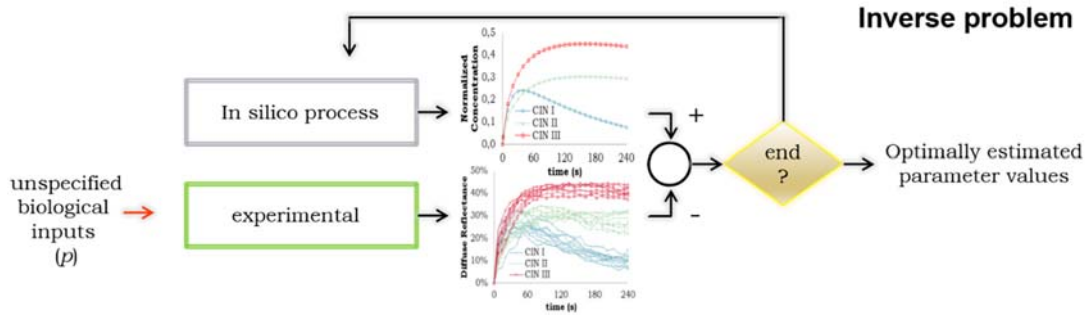
Figure 45 System of inverse problem investigated

This is the minimization of the non-linear objective function of this system:

$$J = \left\|y^{exp}(p,t) - y^M(p^{trial},t)\right\| \qquad (6.1)$$

which is subjected to: $\mathrm{f}\left(\dfrac{dx}{dt}, \mathrm{x}, p^{trial}, \mathrm{u}\right)$

$$t_0 = 0, \quad x(t_0) = x_0, \ t \in [0,240]$$

$$p_L \leq p^{trial} \leq p_U$$

$$\mathrm{u} = u_0,$$

where f is the dynamic description of the model, x are the differential state variables, p^{trial} is latest set of p values used for an estimation, u is the initial amount of acetic acid and p_L, p_U are the lower and upper bounds of the values of the parameters respectively.

77

6.1.1 Experimental process

From medical examinations with DCE-OI, clinical experimental dynamic optical data are obtained by recording measurements of diffuse reflectance of the backscattered light through time, which reflect the pharmacokinetics of AA through the epithelial tissue during the AW phenomenon.

6.1.2 in silico process

From the deterministic, *in silico*, mathematical method described in subchapter 5.5.1, which simulates the experimental process, the normalized concentration of H^+ versus time is obtained for a given set of biological parameters.

By fitting an experimental curve to a model output, the known parameters that produce the output of the mathematical model can be assigned to the parameters of the experimental process with adequate accuracy, as shown in [56].

In the ideal case the global minimum is unique and has the form (in an analogous problem of three parameters) depicted in Figure 46

the ideal case of global minimum   global minimum at the case of reality
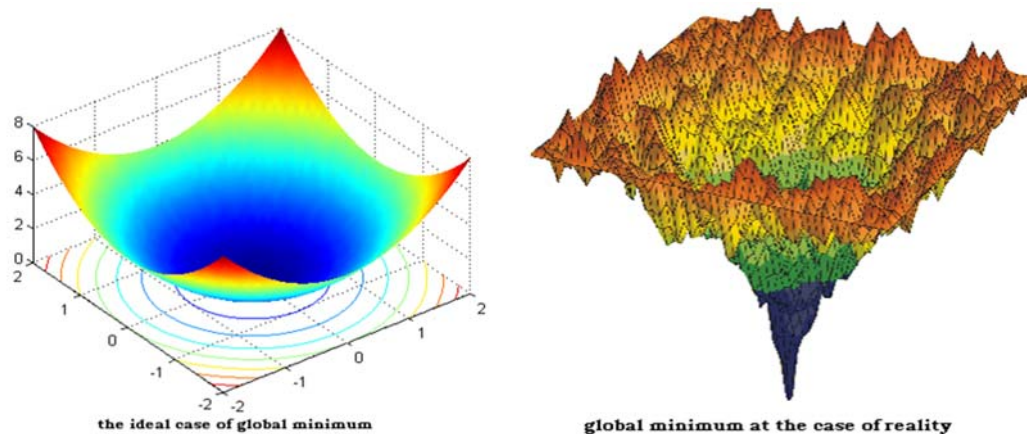
Figure 46 The ideal and the realistic global minimum problem for three parameters

The system described at the left in Figure 46 is not ideal though. More specifically, there are many local minima throughout the dimensional space defined by the system. In case of failing to locate the global minimum, an accepted estimation of the solution would be the value that is found closest to the global minima. A more realistic representation for the problem at hand would be the one presented at the right in Figure 46.

6.2 Fitting constrictions

The system described in every fitting estimation assigns real values to the parameters, one of each is discrete and not continuous (parameter N that describes cellular layers is an integer). It is not deterministic thus cannot be solved in polynomial time. Finally the system is non-linear as the differential equations described in *Chapter 3.3.1* do not represent a linear combination of the variables. Thus the system is a real valued mixed integer non-linear system NP-complete problem, thus the fitting is difficult to be achieved and is of outmost importance to maintain the non-linearity that it includes. In order for the fitting to be achieved and the parameter values described in *Table 9* to be assigned to the experimental data, derivative free global optimization algorithms are conscripted [56].

The most critical step when attempting to solve the inverse problem is to verify whether this problem converges to a unique solution. Converging to multiple sets of parameters corresponding to a single experimental curve indicate a meaningful process, since this has no biological basis. In [57, 58] Global Optimization analysis (GO) was implemented in order to investigate the reproducibility and adequate accuracy of estimations of the set four parameters. GO analysis is based on the minimization of the deviation of the function of simulated data from normalized experimental data. In this context, constrained, direct search, point-to-point and population based, GO algorithms such as the: simulated annealing (SA), controlled random search (CRSwCH), shuffled complex evolution (SCE), genetic algorithm (SRES) and differential evolution (DE), were used for the GO analysis of our model. The purposes of employing all these algorithms, was twofold: a) to develop a strong confidence on whether the problem inherently converges and b) to identify the algorithm (if any) that can be used in real clinical settings (in terms of acceptable combined accuracy and speed). The Normalized Root Mean Squared Deviation (NRMSD) was used as convergence metric between experimental characteristics and model predicted parameters.

Thirty pseudo-experimental (PE) curves by simulation were formulated from a known range of parameter values. In order to represent all the clinical stages of neoplasia and concurrently capture the full spectrum of the output space of the model; these data were selected as follows. First, ten PE curves were empirically adopted based on the features of the experimental dynamic optical data of different CIN stages. Next, another ten PE were developed by dividing the feasible search domain of each parameter into ten subintervals of equal length and then systematically, step-wise, sampling from the lower to the higher values. The rest of the PE curves where randomly created from a stochastic sample, uniformly distributed within the domain of the parameter values. To better assess whether the convergence of the inverse problem to unique solutions practically increases by reducing the parameter dimensionality, this procedure has been followed in order to create two PE data ensembles, one for the four most identifiable parameters provided by prior analysis and one for all possible parameters as input. Of course, all of these simulated data represent exact results, that is, devoid of measurement noise. Finally each algorithm used in this global optimization analysis follows same input rules and constrains as well as having common termination criteria and run under identical computing environment.

It is concluded that the inverse problem has a unique solution. The various algorithms tested show a different degree of convergence with DE followed by CRS performing optimally for our inverse problem. Overall, the problem converges adequately, since the majority of parameter estimation error are under 8.5%. The ability to fit mathematically obtained data to the experimentally obtained data was assessed and an accuracy as high as 99.93% is reached for certain algorithms. Finally, the parameters rejected by global sensitivity analysis consistently fail to converge for all algorithms, reconfirming the four parameters identified in Subchapter 5.6 as the most significant.
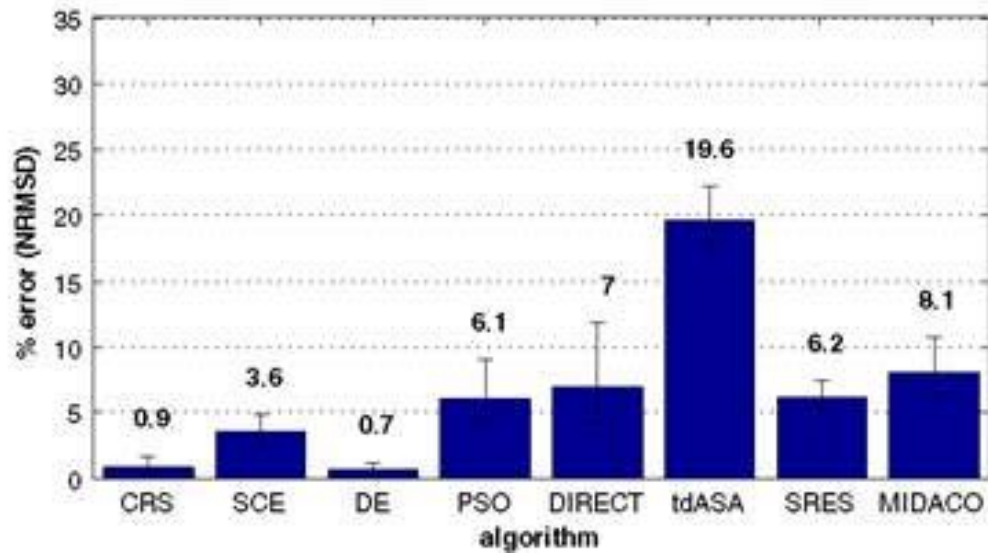
Figure 47 Normalised Root Mean Error of each of the tested global optimisation algorithms for the same set of inverse problem

Table 10 Execution Speed of each of the tested global optimisation algorithms for the same set of inverse problem

Algorithm	Execution Speed (min)	Algorithm	Execution Speed (min)
CRS	0.6151	DIRECT	0.5273
SCE	1.0298	tdASA	1.6227
DE	0.5536	SRES	0.8032
PSO	0.7766	MIDACO	1.5017

Moreover, DE has been identified and proposed as the optimal algorithm due to:

- best degree of accuracy on fitting mathematically produced curves to experimental recorded curves of Hydrogen concentration versus time,
- best degree of accuracy on identifying the values of biological and structural parameters of neoplastic cells
- high degree of performance on minimal time.

This finding is corresponding to statements throughout the literature that DE is a very good algorithm to be applied for global optimization compared to other stochastic algorithms such as the ones included in the study. This concludes that the solution converges to a unique set of biological parameters that correspond to a certain macroscopic dynamic bio-optical curve, depicting the biomarker's uptake kinetics.

6.3 Differential Evolution

Differential Evolution [59, 60] was introduced as a reliable, flexible and easy to use global optimization algorithm. It belongs to the class of evolutionary methods, while integrating essential elements from the adaptive random search methods. As such it is a stochastic, population-based algorithm. There is a plethora of alternative versions of DE in literature. Here, we upgraded the original version of the DE algorithm to handle constraints and integer parameters. Particularly, the algorithm starts by randomly sampling the objective function over the d-dimensional parameter space for creating an initial population of chromosomes i.e. the first generation of feasible parameter sets. Then (mutation stage), some of the initial chromosomes are randomly chosen for the creation, by reflection, of a donor vector of parameter values, without violating any of the constraints. Through a random process this donor vector exchanges some of its constituent parameter values with another random vector that is called the target vector in order to enhance the diversity of the population (crossover stage). Next, the objective value of the resulting offspring and that of the target vector, are compared and the one with the lowest value survives through the next generation. This procedure continues iteratively until a maximum of generations are created or the fitness criteria are met.

6.3.1 Iterative Description

At the start of the algorithm, and if not provided, minimum and maximum nominal value for each dimension is set and a random initial population P is created. Each member of the population is evaluated by the objective function and the best member is identified. During an iteration of the algorithm each and every member of the population is targeted arrow to go under two stages, stage of mutation and the stage of crossover.

In the stage of mutation three randomly chosen members of the population are chosen and a new vector, v, of parameters is created from the parameters of these points. In the case of DE, F is a constant factor provided to the algorithm from the interval [0, 2]. A trial vector, u, is created by the following method

$$u_{j,i,G+1} = \begin{cases} v_{j,i,G+1}, & \text{if } rand_{j,i} \leq CR \text{ or } j = I_{rand} \\ u_{j,i,G+1}, & \text{if } rand_{j,i} > CR \text{ and } j \neq I_{rand} \end{cases} \quad (6.2)$$

where $i=1,2,…,N$ members of population currently targeted, $j=1,2,…,d$ parameter currently observed, $rand_{j,i} \sim U[0, 1]$, I_{rand} a random integer of the interval $[1,2,…,d]$, CR is a probability threshold called crossover factor.

Once the trial vector is completed, it is evaluated towards constrains set upon the algorithm, such as the value of the parameters being within the desired bounds. If no constrain is evaluated it proceeds to the next step, otherwise it is discarded. On the next step, the accepted trial vectors are evaluated towards the objective function and compared towards their respective targeted vectors. The ones with the best out of the two evaluations will be accepted back in the population. Once the termination criteria are assessed, if none is met the algorithm begins the iteration from the start.

6.3.2 Flow Diagram
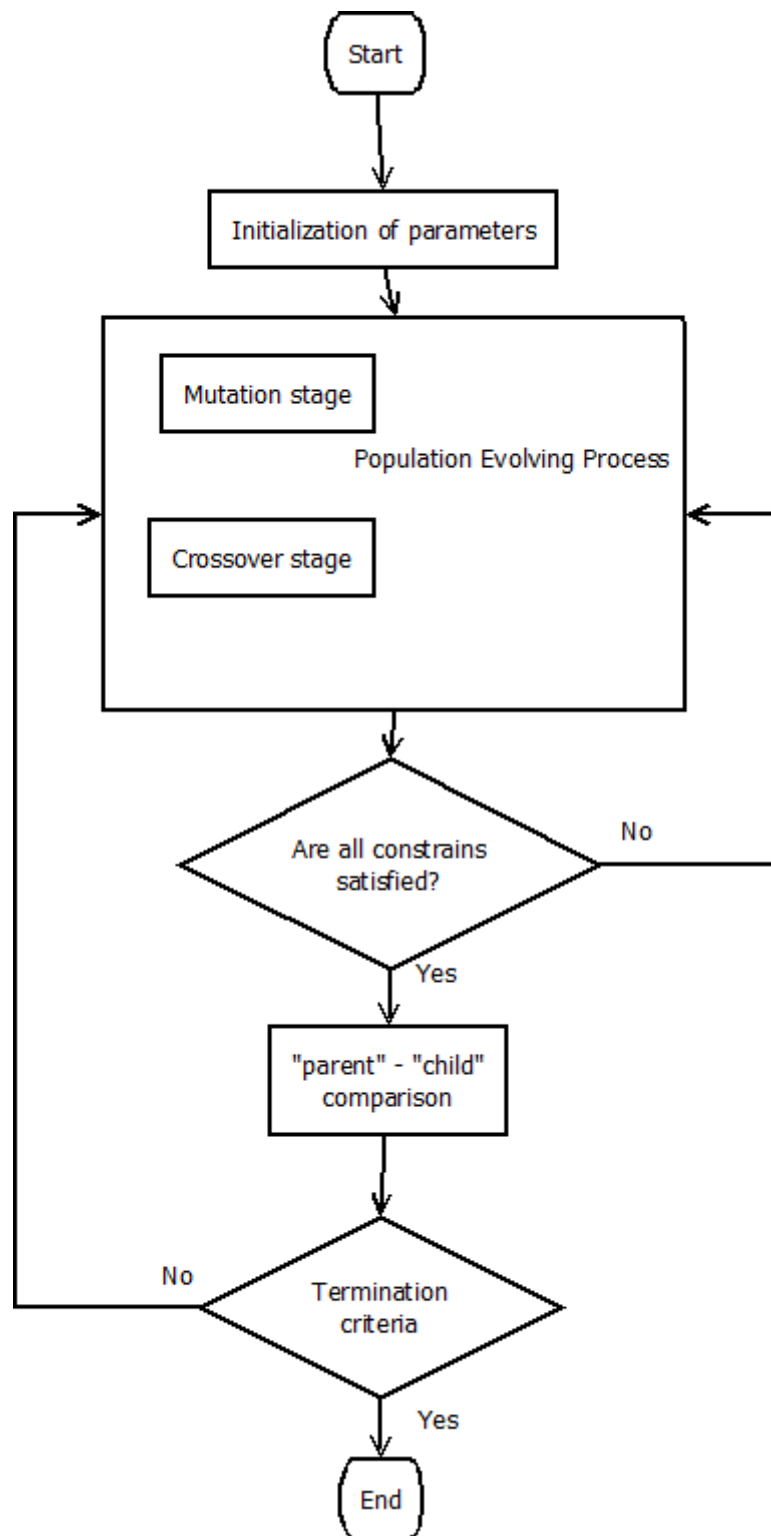
Figure 48Flow Chart of the Differential Evolution Algorithm

6.3.3 Termination criteria

The algorithm would come to a halt once at least one of three criteria was met. These criteria were:

1. If fitting of the curve was achieved. A curve is considered to be fitted if the Euclidian distance of the experimental data from the mathematically produced data was at maximum 0.001cm.
2. If the appointed maximum running time was reached or exceeded. The running time concerns one trial of a given algorithm for each experiment.
3. If the population of the algorithm degenerates so that the mean distance of the members from the geometrical mean of the population falls under a customizable threshold.

6.3.4 Set of parameters provided to the algorithm

*   bu, upper bounds of the variable parameters of the mathematical bio-model that produces an estimated solution
*   bl, lower bounds of the variable parameters of the mathematical bio-model that produces an estimated solution
*   max time, maximum time limit that each algorithm is allowed to spend searching for the global optimum for one run of the algorithm
*   Pop, initial sample multiple/single estimation via which the algorithm can start computing its iterations. The sample size (single or multiple) depends on the mechanics of each algorithm, as same require a single point in the search domain via which to expand , where others require a multiple sample to evolve and inquire. Moreover the size of the sample is analogous to the number of parameters we seek to converge (reduced sample for half-set, increased sample for full-set)
*   peps, an algorithm terminating parameter that determines the lower threshold under which the mean of all dimensions of the problem normalized mean absolute deviation of the estimated population of solutions in each algorithm is considered to have degenerated. Meaning that if the solutions tend to gather in a small area around a certain solution then it is better to terminate the algorithm earlier. Basically this algorithm parameter acts as a primal detection of local optima entrapment of the algorithm.
*   VTR, it is the rough estimation of the global minima of our function that informs the algorithms that any solution produced lower than the value 'VTR' can consider as successful global minima identification.
*   I_bnd_const, flag for existing boundary constrains
    *   1: bounds as bound constrains
    *   0: no bound constrains
*   I_strategy, choice of DE strategy/version to be followed
    *   1 → DE/rand/1
    *   2 → DE/local-to-best/1
    *   3 → DE/best/1 with jitter
    *   4 → DE/rand/1 with per-vector-dither
    *   5 → DE/rand/1 with per-generation-dither
    *   6 → DE/rand/1 either-or-algorithm
*   F_weight, mutation scale factor from interval [0, 2] (referenced as F in literature)
*   F_CR, crossover probability constant from interval [0, 1]. (referenced as CR in literature)

I_bnd_const is determined as 1 due to the inverse problem specifications. The DE version used in the experiments provide the choice of 6 different versions of DE through the I_strategy parameter to which the value 1 was assigned for the classical approach of DE.

As described in literature the F_weight parameter, which provides the mutation scale factor for the DE, is agreed that it is should be optimally chosen from the [0.4, 1] interval as other values are only occasionally effective. It is also noted that the higher the value of F_weight the more premature convergence of the population and its degeneration. As far as F_CR is concerned, it is stated that the higher the value the faster the convergence to the global optimum value inquired, with 0.1 a good first choice followed by 0.9 and 1 with fast convergence when the solution is dependent from the mathematical model parameters.

As is suggested in [61], the values of F_weight and F_CR that correspond to our inverse problem are within the interval F_weight = [0.9, 1] and F_CR = [0.7, 0.9].

Through some practical experimentation, it was concluded that suitable values for F_weight and F_CR are 1 and 0.8 respectively.

6.4 Time complexity

The mathematical model simulating the AW phenomena needs to calculate from 4 up to 40 differential equations. This large differential system was proactively proven time consuming. More specifically, the mathematical model in Matlab script takes approximately 0.6sec to produce a solution. This time consumption is of extreme importance, considering the fact that every algorithm needs to solve the differential equation at minimum once per iteration to maximum the size of the entire population per iteration. For that reason each algorithm run needed maximum 1.5 hours. For the purpose the algorithms were compared, that time was not applicable. The results of this comparison were presented in [58].

In order to reduce time complexity, the script of the biomathematical model was downloaded from Matlab (a high level programming language) to FORTRAN (a low level programming language) [57]. FORTRAN is a low level programming language similar to C that is often used for problems of mathematics and physics. More specifically the version of Fortran 90 was used with a free distribution of DLSODE differential equation solver scripted in Fortran 77, needed for the biomathematical model.

This led to the creation of an even faster bio model identical to the Matlab script that offered approximately 6666% speed increase, producing an output in just 0.009sec on average, while no transformations of the output space needed to be made thus maintaining the reliability the deterministic bio model offers. By implementing this solution, time was reduced from 1.5 hours to 2.5 minutes per run.

An alternative and much faster than the GO method of finding the actual values of the parameters, in case of convergence, is the comparison of the experimental data with a vastly populated set of pre-calculated model curves corresponding to all possible combinations of parameter values [62 - 67].

In an attempt to reduce time complexity even further, a reference table was made as a minor database of estimation points. Based on the bounds of each parameter, that are set by global sensitivity analysis, the model output space is sliced in equal spaces and equally stepped samples

are taken. For each set of parameters (approximately 800.000 sets) a simulated curve is formulated. On the basis that the in silico model is 1-1, the table is refined by omitting sets of parameter with their respective curves, removing sets of higher values of the first parameter representing inactive cellular layers, thusly producing same curves through the in silico model. On the same time, a failsafe in cases of existence of more than one curves within the LUT with the exact same Euclidean Distance with the experimental one, chooses the curve positioned in an earlier entry within the LUT as the closest one. The parameter values that are corresponding to the in silico curve that best matches the experimental on, constitutes the inverse problem solution.

Each parameter was sampled with the following steps

- Parameter N: as it is discrete all values from 1 to 10 were used
- Parameter b: $0.08 * 10^{-7}$
- Parameter pH_{ES}: 0.02
- Parameter ε: 0.3

The parameter sampling, suggest a by default reduction in fitting accuracy by removing a set of solutions from the inverse problem.

6.5 Application of the inverse problem solution on clinical cases

 In order of confirming the actual time complexity reduction while assessing the fitting accuracy trade off, two biopsy confirmed cases were chosen, a high grade and low grade. For each case, pixels are uniformly sampled from the entire image, choosing each time the middle pixel over a square area of 3x3 pixels. This is done in order to reduce the time needed for execution by reducing the pixels used in the procedures to an adequate number. If the surrounding pixels depict a curve with a difference in the area of the curve higher than a predefined threshold, then those pixels are added to the pool of samples. In each case, following this sampling preprocess, comes a parallel pixel by pixel comparison, meaning each sampled experimental curve is either compared directly to the simulated curves in the LUT or run through DE. As termination criteria in the case of the algorithm, the ones introduced in Subchapter 6.3.3 are kept, whereas in the case of the LUT, the LUT member curve with the minimum Euclidian Distance from the experimental pixel curve is considered as the solution. Once all the curves are adequately fitted, the parameters identified per pixel are assigned to the eight neighboring pixels for better visual representation of the pseudo-colour map, though this increase in pixel size is not taken into consideration at the statistical comparison of the two procedures and is used only as visual enhancement. Details of the LUT method are presented in Subchapter 6.6. Moreover, all comparisons made in the scope of this thesis take advantage of parallel computing, utilizing multiple CPU cores.

In order to quantitatively compare the differences of the produced maps for each case, the normalised RMSD of the Euclidean Distance of each fitted curve towards the respective experimental curve was calculated, as well as the collective execution time needed.

Table 11 Execution time and Average Performance of LUT and algorithm based solution approaches to inverse problem

Grade of Lesion	Execution Time (min)		Average Performance (ED Norm. Units)	
	LUT	GO	LUT	GO
LG	0.22	498	0.43	0.35
HG	0.87	456	0.31	0.26

Table 11 summarizes the results of the comparisons performed. As it can be seen, there is a huge difference in the execution time between the GO (8-9 hours) and the LUT (13-50 s) for calculating the values of the four parameters and for displaying the corresponding maps. The second column of the table compares the performances of the two methods using the Euclidian Distance between the experimental curve and the best fitting GO or LUT curve.

The results refer to approximately 10.000 parameter estimations performed for each experimental case. Clearly, the LUT fitting operation outperforms GO fitting as far as time is concerned, with a minimal cost in fitting accuracy.

As far as time complexity is concerned, two things need to be taken into consideration. Firstly, the actual time spent on each pixel is unknown and unpredicted in both GO and LUT methods. For the GO method, time delay is introduced due to the unpredictability of the steps needed to be made by the algorithm towards parameter estimation and only the maximum time is known, which is 2,5 minutes. On the other hand, LUT time variance is due to the size of the LUT compared with each curve, which approximately on average is 10ms with deviation a few milliseconds. Time spent per pixel in the LUT method significantly reduces the time complexity of the entire methodology, since it is of a lower order of magnitude and on the same time has the advantage of further reduction with more targeted search within the LUT. In addition, by accepting the loss of fitting accuracy and implementing the LUT fitting procedure, we can achieve, within few minutes, optimal pixel resolution by rendering the sampling process obsolete. Higher pixel resolution lays the foundation for acquiring additional biological information of the lesion, since each pixel has been found to correspond approximately to the area covered by a single cell.

Parameters	Grade of Lesion	
	LG	HG
N	0.08%	0.07%
b	0.32%	0.15%
pH$_{es}$	0.16%	0.05%
ε	0.25%	0.09%
MEAN	0.20%	0.09%

Moreover, the normalized root mean square deviation of all estimated sets of parameters, for each case has been calculated in order to better asses the difference in estimation of the two methodologies. It is presented in Table 12, where the small deviation of the maps produced by both methods, is evident. As it can be seen, there is a mean difference of approximately 10% to 20% among the estimated sets. Moreover, LG shows a higher differentiation amongst the parameters. Finally, what needs to be noted is that in both cases the number of dysplastic layers is at approximately 0.07-0.08%, which given the discrete nature of the parameter, asserts to a minimal trade-off to estimation of the parameter upon which the classification of the grade of the lesion is heavily dependent.

The minimal loss in fitting accuracy is acceptable in view of the gain in time reduction and clinical applicability. Moreover, it is encouraging to assume that further fitting accuracy and parameter estimation improvement can be achieved with larger LUTs that better sample the output of the model, moderating the time expenditure by targeting the search within the LUT. This leads to the conclusion that both methods can converge to a single unique per parameter per case map. This practically means that instead of a time consuming complex mathematical procedure such as GO, we can produce the same mappings in a matter of minutes by creating a LUT that permits better curve fitting.

Figure 49 Pseudocolour maps per parameter for a high grade lesion. The first column is the maps produced by the algorithm whereas the second is produced by LUT.In the third column a boxplot of the values per parameter found per method is presented

In Figure 49, the pseudo-maps of each parameter by both procedures are depicted along with their respective boxplots for the HG lesion case. Histology results suggest severe malignancy in both points where biopsies are taken. These biopsy points are denoted on the maps by black circles. For both procedures it is clear that at these points the N and b parameters takes the maximum value, while in the same time high acidic environment is displayed in the extracellular pH map. Moreover, we observe a mild overestimation of the N parameter from the LUT methodology with a mild underestimation of the extracellular space compared to the GO one, yet a consistent highly acidic environment. Although we have quantitative inconsistency, we can assume consistency from a biological point of view, where both methodologies suggest HG malignancy, while the LUT methodology attributes its severity to a more vertical and stratified topology whereas the GO methodology attributes it to a more horizontal topology due to increased extracellular space. This malignancy grading comes into agreement with the histology results and can be considered a first validation to both methodologies. Observing the pH map, we identify quantitative consistency between the two methodologies, while in the same time we identify mild to high acidic environment in the areas where the N and b parameter receive high values while gradually more neutral pH values to surrounding areas. This indicates the potential of these maps to borderline the lesion as well as to inform about the risk of metastasis. Particularly, according to the "acid-mediated tumour invasion model", the H^+ flow to peritumoural normal tissue provokes normal cell necrosis or apoptosis and extracellular matrix degradation [68]. Because, the tumour cells are capable of resisting to the toxicity induced from this flow, they are able to invade the damaged normal tissue. This allows them to spread, and eventually form invasive cancers. Finally, in the mappings of the permittivity of the tissue to the biomarker the highest values are found near the biopsy points, yet seems moderate throughout the map, probably indicating a lesser grade of lesion as indicated by the N map.

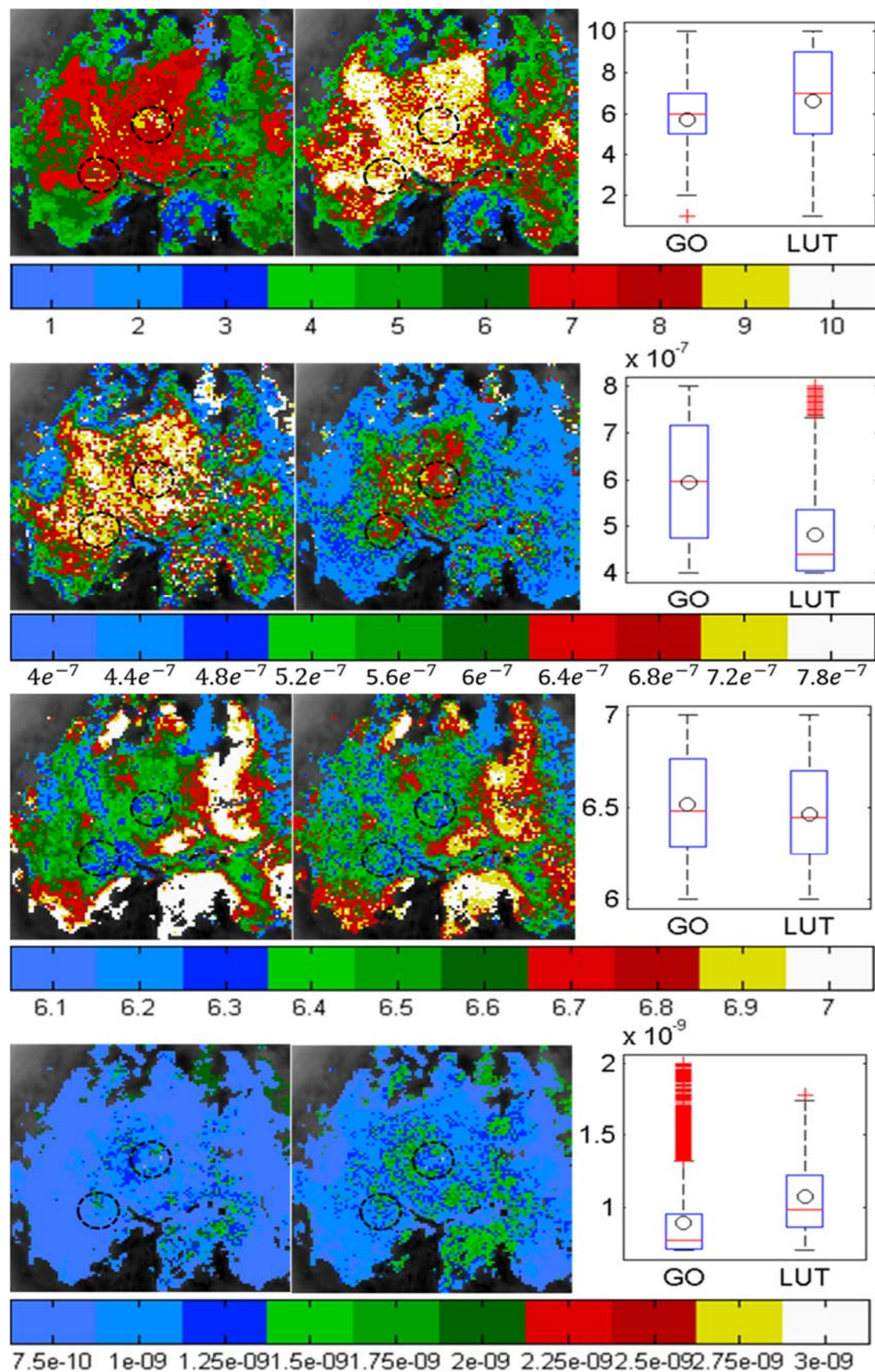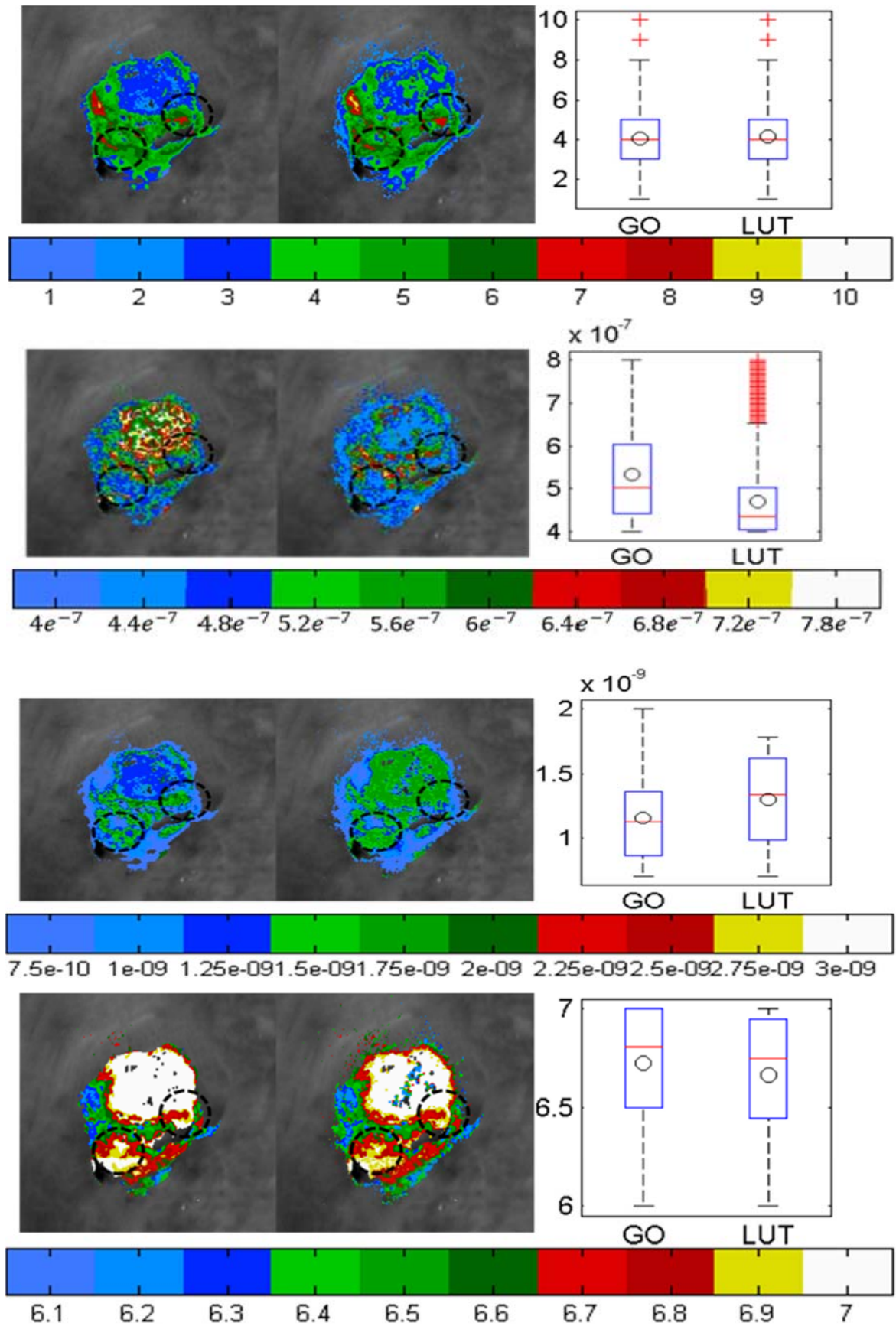*Figure 50 Pseudocolour maps per parameter for a low grade lesion. The first column is the maps produced by the algorithm whereas the second is produced by LUT. In the third column a boxplot of the values per parameter found per method is presented*

In Figure 50, the pseudo-maps of each parameter by both procedures are depicted along with their respective boxplots for the LG lesion case. Histology results suggest early stage neoplasia in both points where biopsies are taken.

The maps corresponding to the LG case show consistency of interpretations with the ones made in the HG case. Here, in the biopsy confirmed points, lower N and b and permeability values have been calculated, while pH_{ES} increases towards neutral values.

As illustrated, there is a moderate cell packaging but no severe malformations. Additionally, no sharp edges or large neoplastic tissue patches appear in the maps. Peak values of N and b parameter from both methodologies are concentrated to the same tissue areas, while throughout the epithelium neutral and mild acidic environment manifests. Both methodologies identify areas of high N and b values, highly acidic extracellular space but low tissue permeability close to the edges of the cervical epithelium. One reasonable explanation of this would be the existence of columnar epithelium. Another explanation for this inconsistency could be the similarity of the features passed on the dynamic signals by two different biophysical mechanisms. It is generally accepted that in LG neoplastic tissues, the signal recorded by DCE-OI is delayed because the biomarker must penetrate into the lower half of the epithelium where the atypical cells are situated [69]. This passes on the dynamics of the measured signals resembling to prolonged acidification, but it is of significantly lower intensity. Based on this similarity, therefore, our predictions of low pH values in LG areas are reasonable but exaggerate.

In all mappings, between the two procedures, there is a deviation to the parameter values estimated. These result in noticeable differences between pixel areas of the pseudocolour maps. The normalized difference between the parameter sets produced by the two methods for each curve is calculated and for each pixel the mean difference of all parameters is considered as the pixel deviation and illustrated as the deviation percentage in Figure 51 for each case. In the majority of the pixels we have low deviation between the two methods, partially due to the mild difference between the performances of each method in terms of fitting accuracy.
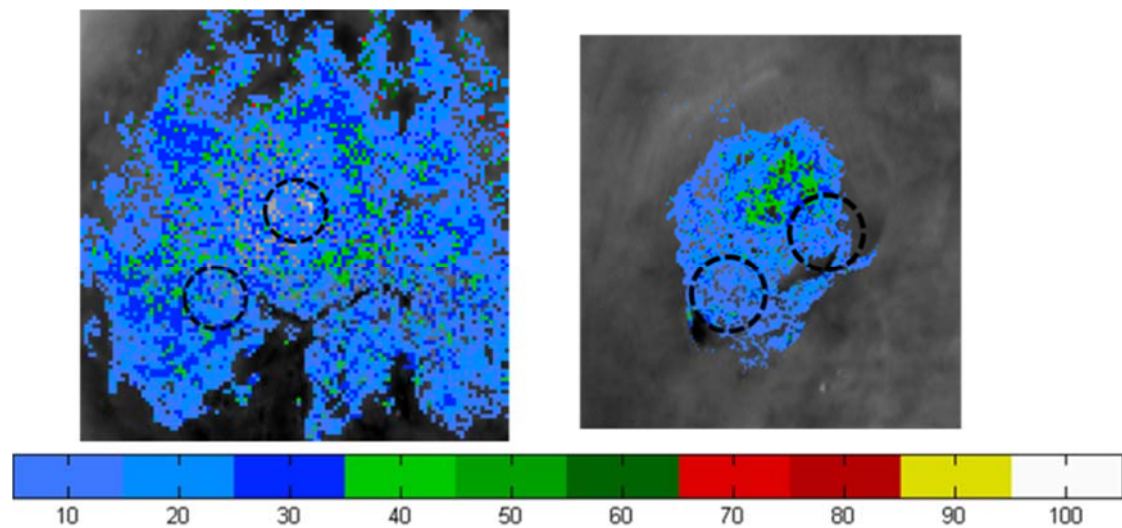
Figure 51 Normalised Root Mean Square Deviation per pixel between algorithm and LUT based solutions of the inverse problem

91

6.5 Optimisation of the LUT based inverse problem solution

A first step towards solving the optimisation problem by the use of a LUT, is the creation of a proper LUT in terms of sufficient size to cover possible solution. That size, although initially consists of approximately 800.000 curves, it is not optimal in terms of time complexity in identifying the optimal solution. Depending on ways of traversing the LUT in search for the solution time varies, yet the result would remain unchanged.

A linear search, also referred to as brute force search, is the most common and simplistic way, where each curve populating the LUT would be compared towards an experimentally obtained curve and assessed. This is often the slowest search method, unless the solution lies at the first entries of the table. Yet it remains as the certain validating method of proof of existence of a solution within the LUT.

Binary search is a commonly used method of divide and conquer search algorithm. With this method each step the table is divided in partitions and by comparison with the point of division, the partition in which the solution lies is identified and fed to the next step as the table. The process repeats until either the solution is successfully identified or no further partitions are possible. Application of such method is possible only if the table is sorted based on the search parameter. In the case under study, the search parameter would be ED of the experimental curve, which practically would suggest comparing the experimental curve with the entire LUT and then have the LUT sorted in order to find optimal solution. This would lead in a time complexity higher than the brute force solution due to the additional time needed to sort the table.

Another method involves use of trivial hash function. With this method, each position within the table is assigned to a key, which is used as an index to reduce the size of possible solutions or in the best cases each solution corresponds to a single key. For small ranged, this method can be amongst the fastest lookup, even exceeding binary search speed with zero branches and executing in constant time. Again due to the nature of intended use of the LUT, in our case a hash table is not easy to be compiled.

In order to decrease time complexity of the procedure, two directions were chosen. Firstly, the size of the LUT used per curve needed to be reduced from the maximum of the linear search, in order to cut down the number of Euclidean Distances needed to be computed. Moving towards that direction, features of the experimental curve towards a curve existing in the LUT are exploited. For the purposes of this thesis this method will be named optimised search. Secondly, the   script responsible for these comparisons was downgraded to a lower level language. The download of the script from Matlab (a high level programming language) to FORTRAN (a low level programming language) was chosen, following the precedence of time reduction on the inverse solution based on the algorithm. FORTRAN is a low level programming language similar to C that is often used for problems of mathematics and physics. More specifically the version of Fortran 90 was used.

6.5.1 Optimised Search

First of all, the table is divided according to the number of neoplastic cellular layers into ten partitions. In order to identify the partitions of interest, four features of a given curve are utilised for a crude estimation of the neoplastic layers. Therefore, for each partition the maximum and minimum value per second is computed, the peak value and the fade point of a given curve. In this manner, four features for each partitions are computed, which provide knowledge of features of all the curves that are part to each. These features are graphically represented in Figure 52. A simple comparison of the corresponding features of an experimental curve towards these ten sets, can reduce the size of the necessary LUT by optimally 90%, with these sets acting as boundaries.

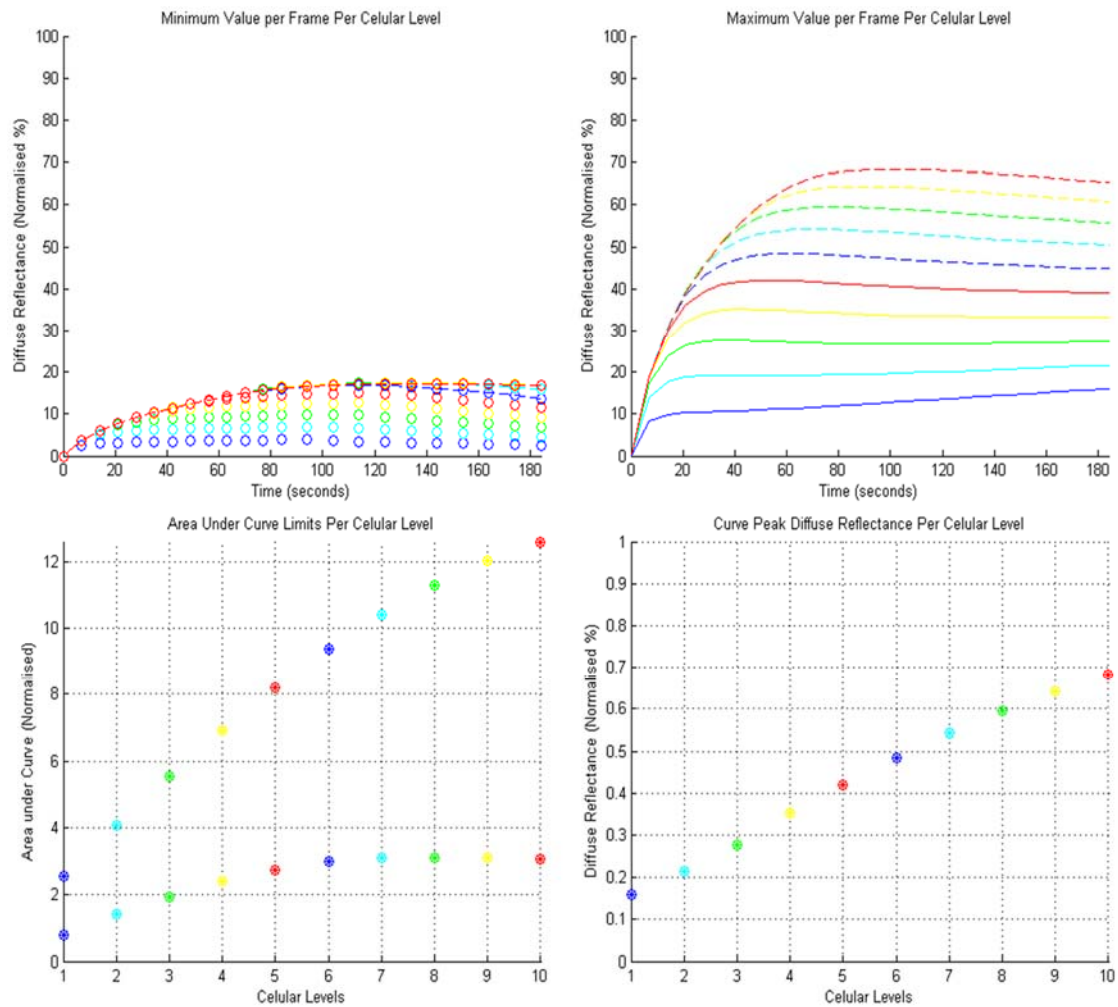*Figure 52 Optical Depiction of the curve features used for optimising the search pattern of the LUT*

Furthermore, each of the ten partitions is once again divided based on the Area under the Curve (AUC). This clustering of curves based on their features can act like a key to a hash table. Computation of the AUC reduces the number of curves needed to be compared from the full LUT to a small number.

As means of assessing the time complexity reduction gained by both the choice of search strategy as well as the script language change, three sets of 1000, 10000 and 100000 distinct curves randomly selected from the LUT and assessed by both search strategies and with both script languages. Moreover, this serves also as means to compute the systematic deviation of the inverse problem solution by computational errors in the LUT search methods. This translates to an uncertainty at each curve convergence. The results are presented in Tables 13 and 14. In the first Table the mean normalised root mean deviation of each strategy over each script language is presented, whereas in the second one, the overall executional time for each case is computed.

Table 13 Normalised Root Mean Square Deviation of the Search methods of the LUT

Number of Curves	Linear Search NRMSD (%)		Optimised Search NRMSD (%)	
	Matlab	Fortran 90	Matlab	Fortran 90
1000	0.00	0.09	1.12	1.08
10000	0.00	0.09	1.15	1.10
100000	0.00	0.09	1.16	1.10

Table 14 Mean Execution time of the Search methods of the LUT

Number of Curves	Linear Search Time (sec)		Optimised Search Time (sec)	
	Matlab	Fortran 90	Matlab	Fortran 90
1000	1.24	0.13	0.07	0.06
10000	11.99	0.81	0.17	0.12
100000	115.80	6.38	1.34	0.71

Linear search has a systematic deviation of 0% in Matlab and 0.09% in Fortran 90 mainly due to systematic deviation in computations due to machine numerical precision. Optimised search has a slightly increased systematic deviation of 1.1% to 1.15% caused by both numerical precision and deviations from the feature extraction process that narrows the LUT search scope. This 1% reduction in estimation accuracy is negligible in the indisputable high reduction in time complexity. The gain by both the change in search strategy from linear to optimised search as well as paramount in inverse problem solution to be applicable in a full scale frame and within the time span appropriate for clinical use.

A data set of biopsy confirmed cases was selected to compare the two strategies of LUT traverse under experimental conditions. Outliers were excluded, meaning cases such as cases with bleeding tissue, glare artefacts, foam and excessive mucus. Sixteen cases were selected as part of the comparison set. Half of those cases were confirmed as high grade and the other half were confirmed as normal or low grade.

In each case pixels that present curves that are not identified as a response expected to be induced by the AW phenomenon, are excluded by the optimisation process. In order to automatically select the pixels fed to the optimisation process, each frame is pre-processed in order to extract the AW induced optical signal. It needs to be noted that this pre-processing is not optimised nor in its time complexity neither in feature extraction accuracy, yet it provides a good first estimate in downsizing the initial pixel number. In each RGB frame, the green channel is selected, where the optical signal induced by AW is more dominant. From each frame the first frame, in which the tissue is captured absent of acetic acid, is subtracted. Thusly only the temporal difference per pixel is isolated, thusly unaffected by AW tissue areas are

automatically set to zero. Moreover, in order to enhance the signal, the frame is also normalised towards the difference of the green channel of the first frame from the maximum intensity that the sensor can record. This difference expresses the general scattering intensity at the green portion of the EMR. Normalisation towards this enhances signal produced by backscattering, even to areas where human vision might be insensitive.

$$DR_{experimental}(i) = \frac{frame(i)_{green} - frame(1)_{green}}{Maximum\ Intensity - frame(1)_{green}} \quad (6.3)$$

Where

- $DR_{experimental}(i)$ is the recorded diffuse reflectance curve per pixel during the time span of the examination, providing the experimentally obtained signal
- $frame(i)_{signal}$ is the green channel of a frame in a given time instance i of the examination
- $Maximum\ Intensity$ is the maximum pixel intensity recorded by the camera in use. In our case that is 255.

Afterwards, curves identified as outliers are removed based on features such as their peak value, their area under the curve and the signal fading point. Once pre-process is complete, for each curve a set of parameters is attributed from the LUT using one of the two search procedures. This process is done to each curve per pixel for each of case using both search options. Moreover, it needs to be noted, that the optimised search exploits certain features in order to reduce the size of the LUT used. This leads to a number of pixels to be reduced, as their curve can be identified with features outside of the range of the LUT.

Table 15 Detailed results of the two LUT search methods per clinical case

Case of study ID number	Grade of lesion	Linear Search			Optimised Search		
		Pixel No	Mean NRMSD (%)	Time (min)	Pixel No	Mean NRMSD (%)	Time (min)
DS-014	High	114934	7.78%	13.13	114936	9.65%	0.75
DS-018	High	254701	5.69%	29.36	254735	6.47%	1.61
DS-031	High	198615	7.57%	27.29	198615	9.22%	1.18
DS-038	High	146219	6.73%	21.83	146219	7.44%	0.99
DS-047	High	110578	8.40%	15.49	110589	9.82%	0.73
DS-058	Low/Normal	21647	4.70%	3.47	21647	5.38%	0.22
DS-070	Low/Normal	45124	4.53%	6.16	45124	5.40%	0.34
DS-073	Low/Normal	9642	9.20%	1.59	9650	11.28%	0.13
DS-076	Low/Normal	15436	10.44%	2.51	15436	10.96%	0.17
DS-079	High	211418	7.35%	26.27	212222	8.87%	1.26
DS-092	High	177131	18.21%	19.48	177285	18.84%	1.09
DS-121	Low/Normal	165251	6.90%	19.78	165303	8.41%	1.01
DS-318	Low/Normal	38547	11.03%	4.81	38547	13.42%	0.27
DS-337	High	135034	8.42%	18.13	135040	8.95%	0.86
DS-607	Low/Normal	19015	2.81%	3.06	19015	3.05%	0.23
DS-621	Low/Normal	58830	10.61%	7.20	59016	12.79%	0.40

Table 16 Collective results and difference of the two LUT search methods

	Linear Search	Optimised Search	Difference
Total Number of Pixels	1722122	1723379	-1257
Mean NRMSD (%)	8.15%	9.37%	-1.22%
Mean Time (min)	13.72	0.70	13.02
Total Time (min)	219.56	11.23	208.34

In order to quantitatively asses the degree of convergence of each search method, the normalised RMSD of the Euclidean Distance of each fitted curve towards the respective experimental curve was computed and an average over the number of curve per pixel was produced. Moreover, the total time needed for each method to estimate a set of parameters for each curve was recorded.

In Table 15 and in Table 16 the analytical results per case and the aggregated results are presented respectively. It is evident that in the majority of the cases, both methods provide a degree of convergence higher than 85% in a matter of minutes.

In comparison with the inverse solution methodology which involves deploying and optimization algorithms, both LUT based methodologies provide also an adequate first estimation with a mean normalised RMSD close to 10%, leading to the assumption that they provide a good and adequate first estimate with room for future improvement. Moreover, both LUT methods provide full pseudocolour maps for four parameters in a matter of minutes. Advantages of use of the LUT over algorithm is clearly evident, since in average 1.5 minutes would be a time needed for adequate convergence by means of the algorithm for a single pixel, whereas in average 0.7 minutes are sufficient for thousands of pixels to have sufficient parameter sets estimated. Moreover, in less time needed for a single case to be processed by the algorithm, linear search, which is the slowest of the two search methods, has processed a total of twenty cases.

The inverse problem as described in Subchapter 6.1, has a number of local optima, where an optimisation algorithm might be trapped. On the other hand using a predefined set of solution, at the worst case scenario multiple curves would be found with the exact same ED from the experimental curve. In such occurrences the method of search within the LUT hold a fundamental role. Linear search bases the outcome only to the metric used, in this case ED. On the other hand the optimized search exploits curve features that may lead to rejection of a certain set of curves that might have a smaller ED. A difference in mean NRSMD is observed to be close to the systematic deviations in estimation, where linear search provides a lower deviation than optimised search at the scale of 1.32%. Moreover, the mean time complexity of the search per case is increased by almost 2000%. Furthermore, the mean time needed for the optimized search is under 5 minutes which is a time frame that could be applicable in clinical conditions. More specifically, a mean time of approximately 40 seconds is needed to fully solve the inverse problems for all the identified pixels of a single case with an accuracy higher than 90%. This trade-off between time and accuracy allows room for further investigation of achieving higher accuracy with minimal cost to the applicable time. More densely populated LUTs can be deployed, as well as use of the deferential evolution algorithm in a limited number of pixels.

In Table 17 the mean differences in parameters produced by the two methods for each case are presented. The converged curves in both cases have less than 0.8% Euclidian distance between them, yet a mean difference of 3.69% over the estimated parameter sets is observed. This proves that both methods are statistically similar. On the other hand a high average 8.55% difference in the extracellular space estimated is observed and a 2.43% difference in the primary parameter of cellular layer. This difference is of significant importance as it could potentially influence an automated grading of the case, yet it is small enough to be of minimal impact. Moreover, despite the crude initial estimation of the cellular layers in the optimized search of the LUT, the average estimation of the layers is approximately similar. This holds potential for further guided estimation by means of features of a given curve that could be used to reduce the time needed by either an LUT search or an algorithm based estimation and increase the overall convergence.

Table 17 Normalised Root Mean Square Deviation per parameter per case for the two LUT search methods

| Case of study ID number	Grade of lesion	Differences (%)				
		Cellular Layers	Extracellular Space	pH	Tight Junctions	Convergence Deviation
DS-014	High	2.27%	5.89%	2.15%	1.13%	0.41%
DS-018	High	2.34%	7.31%	2.59%	1.23%	0.44%
DS-031	High	2.23%	5.01%	2.83%	0.77%	0.36%
DS-038	High	2.08%	8.43%	2.44%	1.04%	0.44%
DS-047	High	2.80%	8.33%	2.33%	1.92%	0.48%
DS-058	Low/Normal	2.60%	12.64%	3.48%	0.88%	0.54%
DS-070	Low/Normal	3.23%	8.49%	3.04%	1.99%	0.42%
DS-073	Low/Normal	2.78%	11.93%	2.28%	2.37%	0.64%
DS-076	Low/Normal	1.74%	12.34%	1.44%	0.96%	0.31%
DS-079	High	2.33%	5.29%	3.13%	0.92%	0.37%
DS-092	High	2.66%	11.07%	2.95%	2.10%	0.74%
DS-121	Low/Normal	3.38%	9.84%	1.57%	2.46%	0.50%
DS-318	Low/Normal	2.08%	6.82%	1.89%	1.27%	0.34%
DS-337	High	2.02%	9.66%	2.19%	0.95%	0.39%
DS-607	Low/Normal	1.42%	5.10%	1.29%	1.26%	0.17%
DS-621	Low/Normal	2.92%	8.59%	1.70%	1.98%	0.51%
Mean over all cases		2.43%	8.55%	2.33%	1.45%	Mean over all cases and parameters
						3.69%
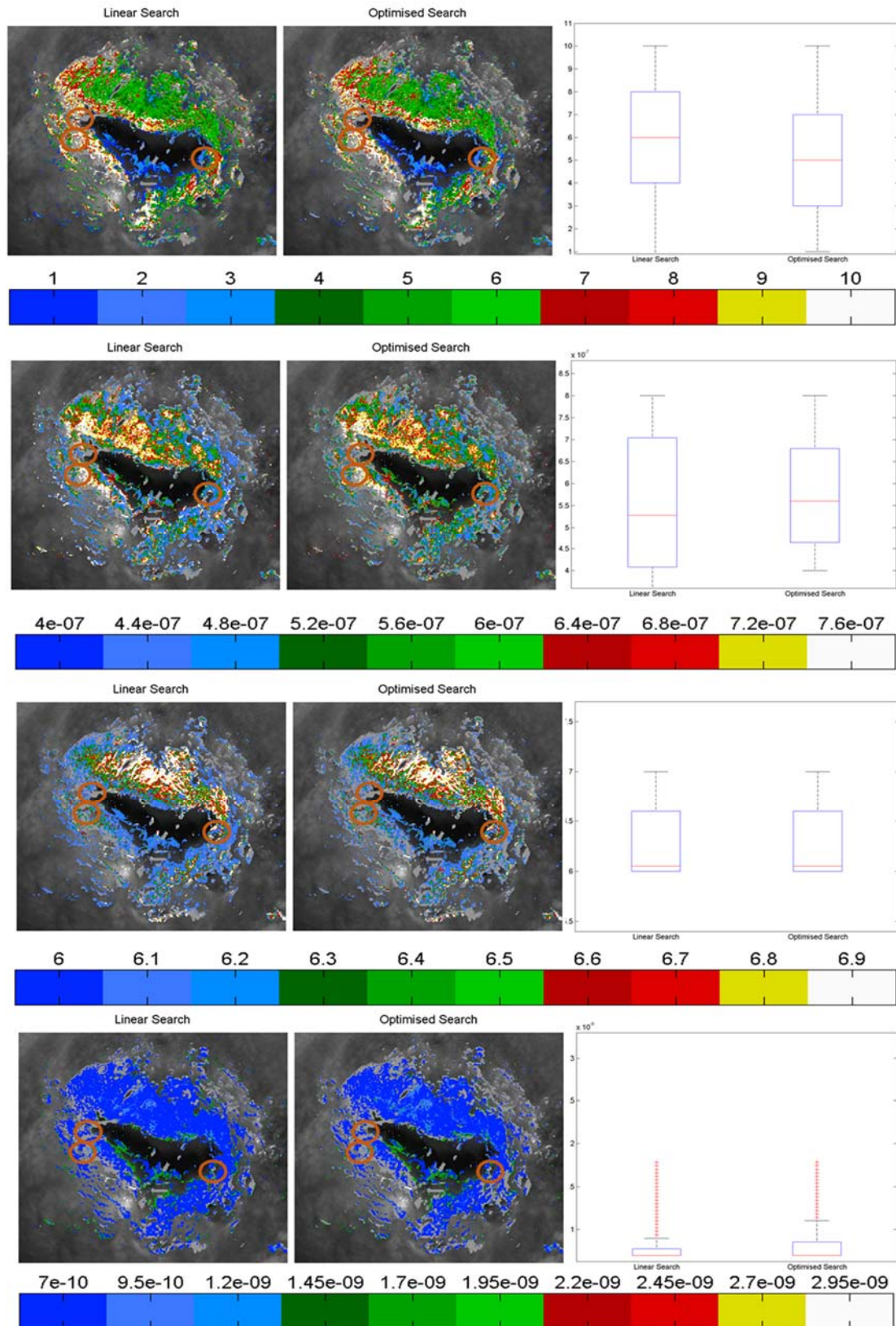
Figure 53 Pseudocolour maps per parameter for a high grade lesion. The first column is the maps produced by the linear search whereas the second is produced by optimised search. In the third column a boxplot of the values per parameter found per method is presented
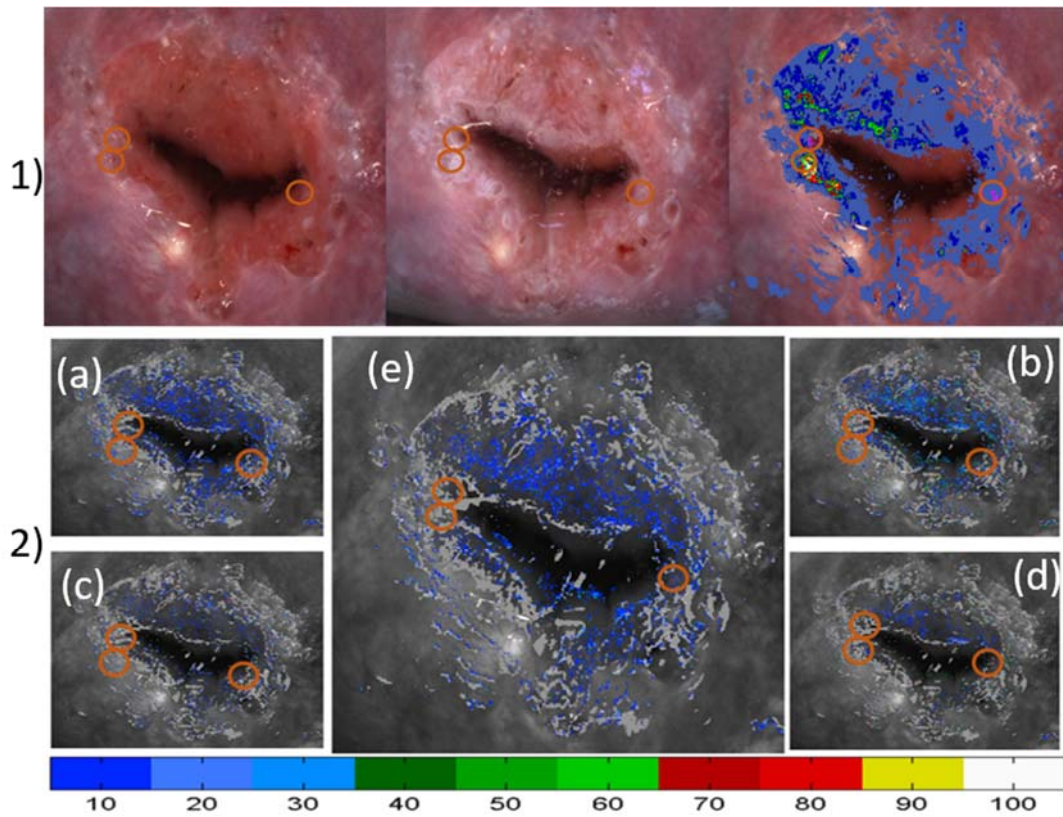
Figure 54 1) images pre and post acetic acid application upon the cervix are presented next to the pseudocolour map given by DySIS.
2) Normalised Root Mean Square Deviation per pixel for a) Cellular layers b) extracellular space c) extracellular space pH d) tissue permeability e) average over all four parameters

In Figure 54 the tissue of a HG case, where the LUT search methods achieved 7.78% for linear search and 9.65% for optimised, is shown at its natural state absent of AA, as well as 144 seconds after application of AA with the resulting pseudocolour map produced by DySIS. Moreover, percentage pseudocolour mappings for each parameter as well as for an average over all parameter is given to depict the spatial distribution of the difference between the two searches. It is clearly evident the estimated parameter sets have minor difference, statistically insignificant and limited to a portion of the sets rather than the entirety of the mappings. The detailed mappings produced of each parameter by both LUT search methods are depicted along with their respective boxplots in Figure 53.

Histology results suggest severe malignancy in two of the three points where biopsies are taken, and a CIN II lesion at the third. It is of high interest to note that in this case, the assigned colposcope predicted high grade for one of the two severe lesion sites identified and low for the other, whereas the CIN II point was identified as normal. On the other hand DySIS identified the two HG sites correctly whereas the mild neoplasia site was identified as normal. These biopsy points are denoted on the maps by deep-orange circles.

For both procedures it is clear that at these points the N and b parameters takes high values, while in the same time high acidic environment is displayed in the extracellular pH map. Moreover, no significant difference in values can be seen with naked eye, suggesting that difference in set estimation is limited to comparatively few number of pixels and in a difference of a single sampled step in the LUT. We can assume consistency from a biological point of view, where both methods suggest HG malignancy, suggesting increased neoplasia even to the biopsy confirmed point that both a trained colposcope and DySIS failed to identify. This malignancy grading comes into agreement with the histology results and can be considered a first validation. Observing the pH map, we identify quantitative consistency between the two methodologies, while in the same time we identify mild to high acidic environment in the areas where the N and b parameter receive high values while gradually more neutral pH values to surrounding areas. This indicates the potential of these maps to indicate the extensiveness of the malignancy as well as indicate its potential propagation and possible growth from primal to metastatic cancer in a more accurate perception that state of the art technology. Moreover, despite not an increased convergence in average of the pixels, the findings provide consistent with histology findings. Finally, while findings are as consistent with histology as amongst the two methods, the optimised search provides estimations of parameters sets in approximately a single minute instead of more than 10 minutes needed by linear search, providing a paramount increase in speed.

Figure 55 Pseudocolour maps per parameter for a low grade lesion. The first column is the maps produced by the linear search whereas the second is produced by optimised search. In the third column a boxplot of the values per parameter found per method is present
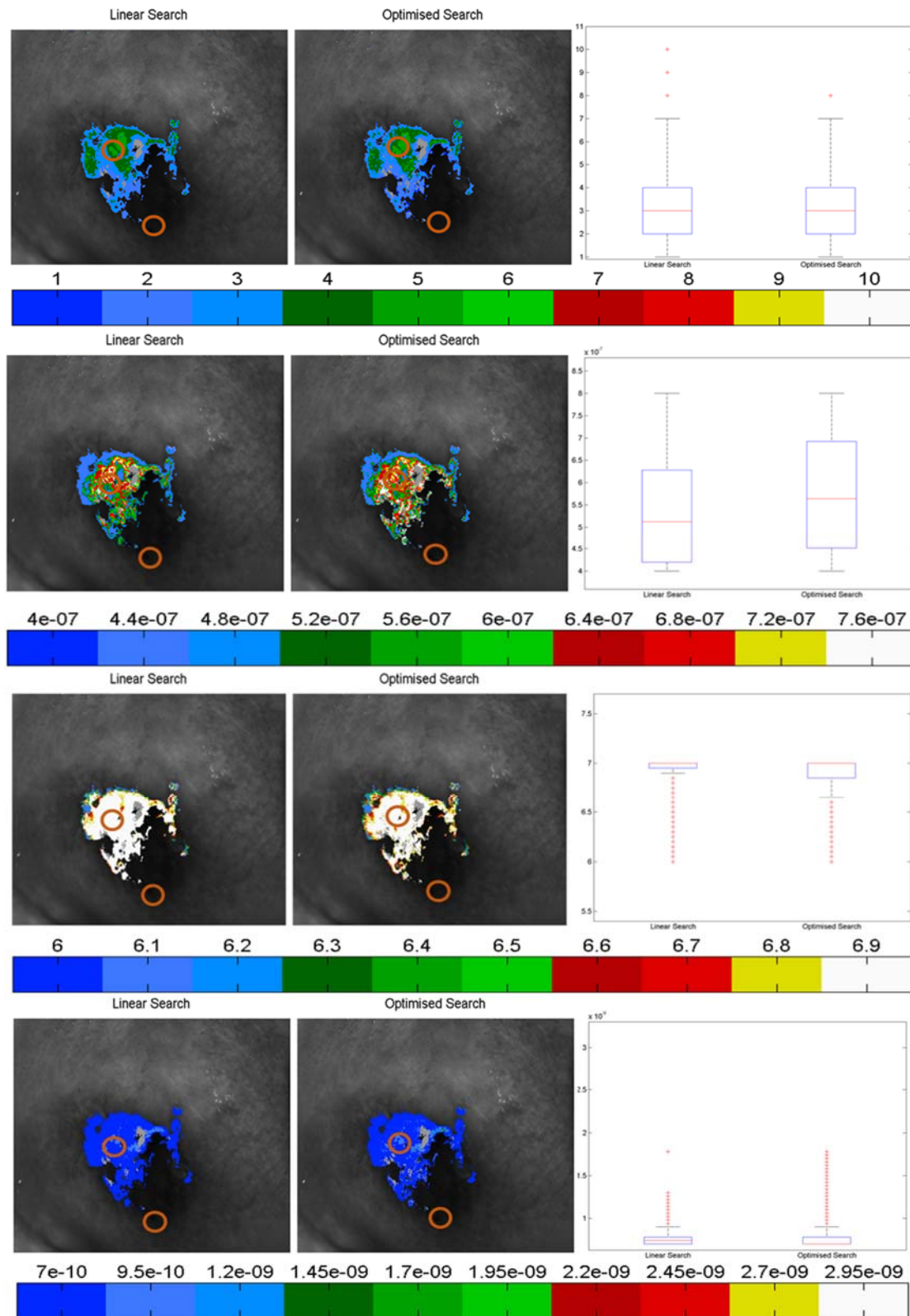
In Figure 55, the pseudo-maps of each parameter by both search methods are depicted along with their respective boxplots for the LG lesion case, where linear and optimized methods had 4.7% and 5.38% NRMSD respectively. Histology results suggest early stage neoplasia in one of the points where biopsies are taken and normal tissue at the second. The tissue in normal state as well as 144 seconds after application of AA and the pseudocolour map produced by DySIS are shown in Figure 56.

The maps corresponding to the LG case show consistency of interpretations with the ones made in the HG case. Here, in the biopsy confirmed points, mild N and b and low permeability values have been calculated, while pH_{ES} increases towards neutral values.

As illustrated, there is a moderate cell packaging but no severe malformations. Additionally, no sharp edges or large neoplastic tissue patches appear in the maps. Peak values of N and b parameter from both methodologies are concentrated to the same tissue areas, while throughout the epithelium neutral and mild acidic environment manifests. Both methods identify areas of high b values and of highly acidic extracellular space but low tissue permeability close to the edges of the cervical epithelium. This suggests an area of draining where the applied acetic acid concentrates, lowering the pH values of the extracellular area. The rest of the parameters do not suggest sever malformations which indicates that pH is acetified mainly due to the biomarker.

In the majority of the pixels we have low deviation between the two methods, yet an increased difference is observed at the extracellular space at the site of the tissue where the signal is increased mainly due to the lack of depth.
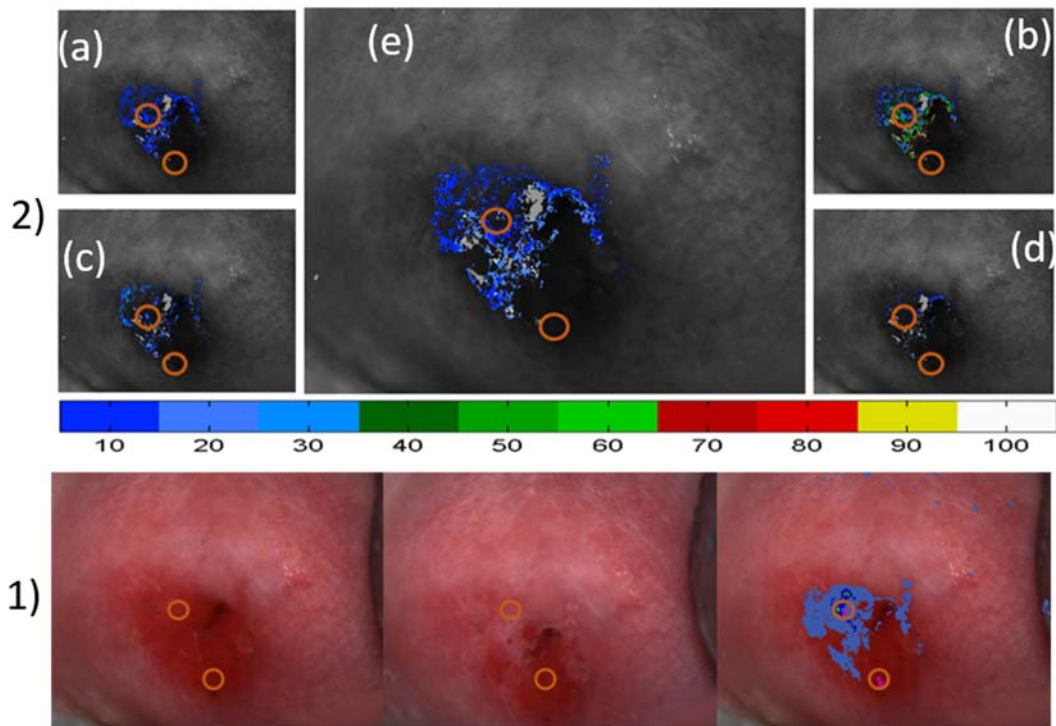

Figure 56 1) images pre and post acetic acid application upon the cervix are presented next to the pseudocolour map given by DySIS.
2) Normalised Root Mean Square Deviation per pixel for a) Cellular layers b) extracellular space c) extracellular space pH d) tissue permeability e) average over all four parameters

Figure 57 1) images pre and post acetic acid application upon the cervix are presented next to the pseudocolour map given by DySIS for a high grade case. 2) Pseudocolour map of the spatial distribution of neoplastic cellular layers with the respective boxplot of the distribution 3) Pseudocolour map of the spatial distribution of extracellular space with the respective boxplot of the distribution parameters 4) Pseudocolour map of the spatial distribution of pH values of extracellular space with the respective boxplot of the distribution 5) Pseudocolour map of the spatial distribution of tissue permeability with the respective boxplot of the distribution

In Figure 57 the tissue of a HG case, where the LUT search methods achieved 7.57% for linear search and 9.22% for optimised, is shown at its natural state absent of AA, as well as 144 seconds after application of AA with the resulting pseudocolour map produced by DySIS. The detailed mappings produced of each parameter by optimized search in LUT are depicted along with their respective boxplots in Figure 61.2 to 61.5, produced in 1.18 minutes.

Histology results suggest severe malignancy in two of the three points where biopsies are taken, and a normal tissue at the third. It is of interest to note that in this case, the assigned colposcope predicted low grade for one of the two severe lesion sites identified. All the rest predictions by both the colposcope and DySIS were accurate. These biopsy points are denoted on the maps by deep-orange circles.

It is clear that at these points the N and b parameters takes high values, while in the same time mild acidic environment is displayed in the extracellular pH map and low permeability. We can assume consistency from a biological point of view. This malignancy grading comes into agreement with the histology results and can be considered a validation. Observing the pH map, we identify mild acidity instead of an expected high acetic environment at a high grade lesion. As it can be seen under the adjacent neighbouring white tissue, there is a dense branch of the blood circulation system. As a result pH values tend to increase towards neutral values, due to the effective removal of produced waste by mitosis. Such cases might lead to a partial decrease to the produced signal by AA and lead to underestimation of the severity of the lesion by trained professions, as in this case, increasing the subjectivity of the examination.
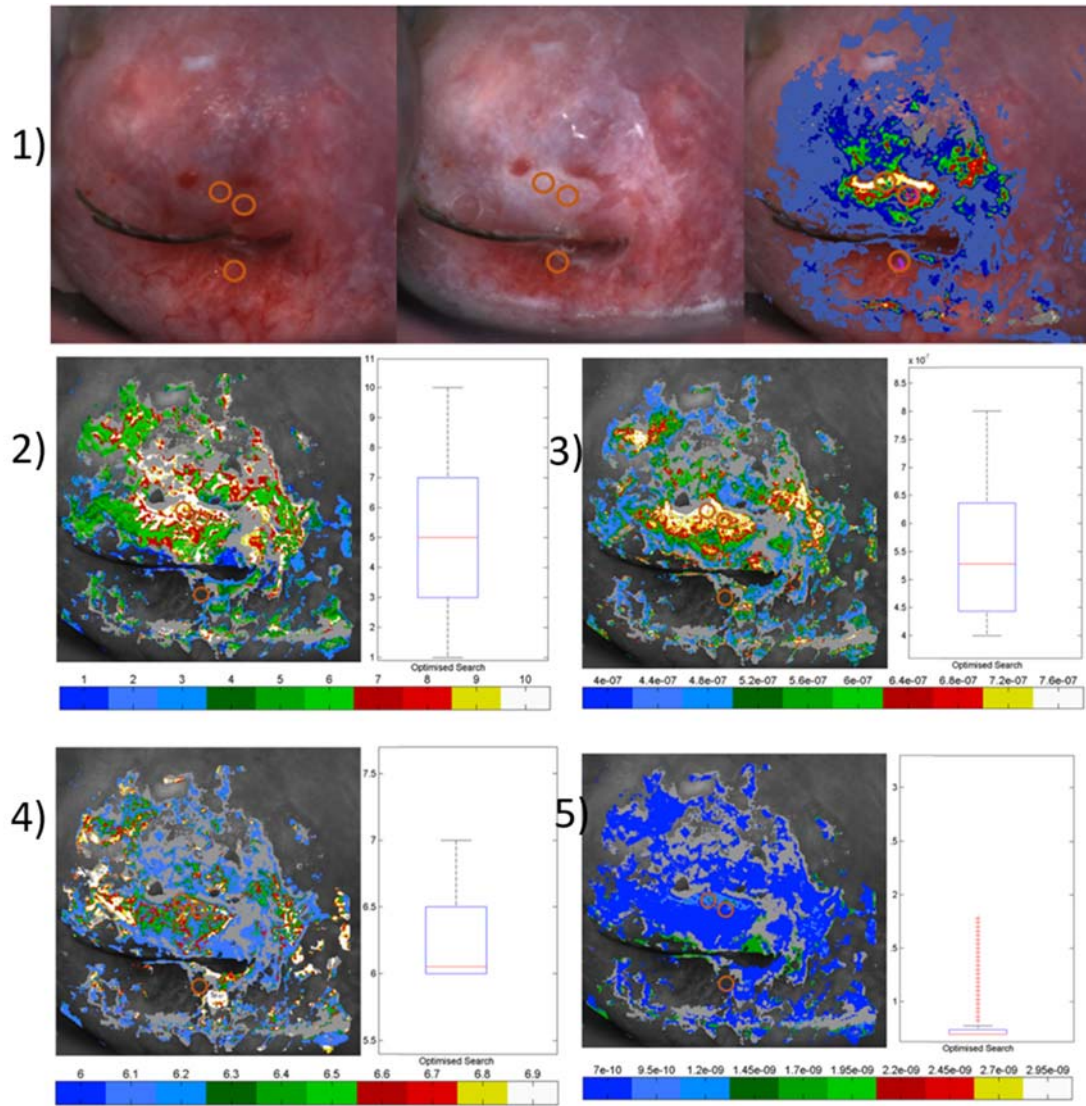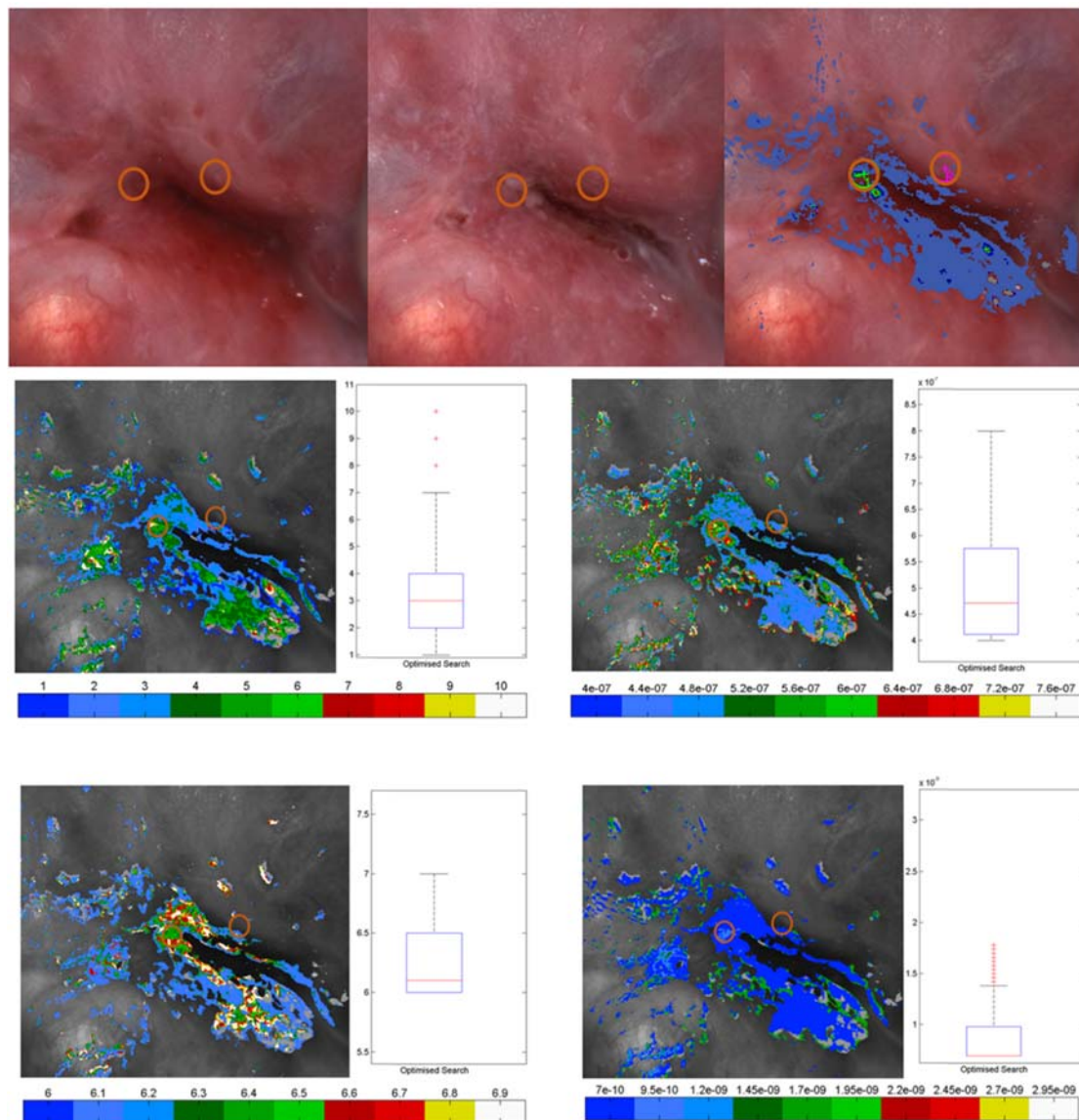

Figure 58 1) images pre and post acetic acid application upon the cervix are presented next to the pseudocolour map given by DySIS for a low grade case. 2) Pseudocolour map of the spatial distribution of neoplastic cellular layers with the respective boxplot of the distribution 3) Pseudocolour map of the spatial distribution of extracellular space with the respective boxplot of the distribution parameters 4) Pseudocolour map of the spatial distribution of pH values of extracellular space with the respective boxplot of the distribution 5) Pseudocolour map of the spatial distribution of tissue permeability with the respective boxplot of the distribution

In Figure 58, the tissue in normal state as well as 144 seconds after application of AA and the pseudocolour map produced by DySIS are also shown for a LG case. Underneath, the pseudo-maps of each parameter by optimised search method are depicted along with their respective boxplots, where linear and optimised methods had 4.53% and 5.4% NRMSD respectively. Histology results suggest normal tissue in the points where biopsies are taken.

The maps corresponding to the case show consistency of interpretations with the ones made in the HG case. Here, in the biopsy confirmed points, low N and b and low permeability values have been calculated, while pH_{ES} tends towards neutral values.

As illustrated, there is an insignificant to minor cell packaging but no severe malformations. Additionally, no sharp edges or large neoplastic tissue patches appear in the maps. Peak values of N and b parameter from both methodologies are concentrated to the same tissue areas, while throughout the epithelium neutral and mild acidic environment manifests. Tissue areas where AA is drained are resulting in high acetic pH values yet the rest parameters do not suggest any sever malformations, reaffirming a low grade to normal estimation to the state of the tissue.

7. Discussion and Future Work

7.1 Discussion

Cancer research is rigorously ongoing, with only recent advancements focusing on tumour heterogeneity. New screening methods and more specific biomarkers are constantly being researched. Under this light and in the scope of this master thesis, a new imaging modality is introduced as a means of a low cost, non-invasive real-time screening methodology, customizable towards a chosen set of biomarkers applied simultaneously at the same tissue area. This modality holds high potential in recording spectral information for temporal phenomena. Thusly, multiple biomarkers can be used simultaneously on tissue samples either in vivo or in vitro and be simultaneously analysed and quantified using spectral, temporal and spatial information. This comes as a valuable next step to common practices limited to use of a single biomarker observed only by a trained examiner, thusly being subjective by human perception, while resulting to qualitative information. As consequence in providing in vivo, early detection and grading of a lesion, this may lead to minimizing the need for biopsies, to offer objective follow up, to be a valuable guide and evaluator to see-and-treat practices and to become a valuable tool to personalised medicine, reducing the cost of diagnosis and treatment while increasing its specificity and sensitivity all the while reducing mortality.

The use of a high-resolution real time novel multispectral system is proposed as the main hardware composition of the imaging modality. A Spectral Deconvolving algorithm as well as a Camera Sensitivity measurement were presented in association with the system to eliminate any cross-talking between the spectral bands captured. The results of this spectral deconvolution and channel cleansing is validated in order to assess plausible loss of information and verify spectral fidelity and crosstalking noise removal. Spectral estimation can be performed with this system and the effects of the proposed spectral deconvolution and channel cleansing towards spectral estimation accuracy are explored and found of increase in spectral sensitivity of a given low cost RGB sensor.

In addition and surplus to the aim of this thesis, the resulting spectral information become of great importance and can be used to provide a number of additional information. First of all, in a simple use, it can be used to perform weighted colour reproduction resulting in high fidelity colour images, free of metamerism. Moreover, by incorporating regression algorithms of the expected spectral signatures recorded, the concentration of chemical stains and biomarkers can be estimated providing real time spatial information of their uptake in the form of pseudo-colour maps.

Temporal knowledge of this uptake of a given biomarker is a valuable asset in diagnosis of a pathology. The volume of the uptake is an indicator to the severity of the disease and the functional and structural characteristics of the tissue and can provide objective and quantitative analysis to the diagnosis. To the best of our knowledge such an efficient and integrated solution that provides information in vivo, non-invasively and in real time, has not been reported so far.

On a step even further, use of temporal characteristics of the uptake of a biomarker can be incorporated with bio-mathematical and bio-physical models, providing valuable information of the imaged tissue even down to molecular level. Focusing on the use of Acetic Acid and a formerly presented bio-mathematical and bio-physical compartmental model of Cervical Intraepithelial Neoplasia a novel bio photonic method for estimating and mapping a set of neoplasia-related biological parameters, from dynamic optical data (DCE-OI), in vivo is

described. This method comes as a natural continuation to the imaging modality described in this thesis and is incorporated as a complete proposed modality for multiband dynamic molecular imaging of a tissue by observing dynamic phenomena occurring after the use of multiple biomarkers.

The inverse problems stated between the temporal uptakes of acetic acid, in the form of concentration towards time, and the estimated uptake depending on structural and functional parameters of the tissue has been found to be adequately solved and statistically converge to a single solution of a set of the aforementioned parameters. The inverse problem is solved per pixel by means of the optimal global optimisation algorithm (GO) as well as by means of a look up table (LUT). Both methods for solving the problem has been found of statistical significant convergence providing pseudo-colour maps depicting spatial information for each of the structural and functional parameters of the tissue. By comparing the two procedures, consistency and adequate accuracy was shown by both. However, the LUT approach was proven to be hugely faster than the GO approach offering, at the same time, similar accuracy levels. This makes the LUT approach suitable for clinical implementation and a valuable means for calculating maps of biological parameters directly correlated with the malignancy grade. This is supported by results from the application of the method in real clinical cases, where a high degree of consistency between the methodology results, histologic analysis and data from literature was observed. In addition, optimal search methods of the LUT were explored and evaluated based on fitting accuracy and time complexity. An optimal search method is proposed as an initial search pattern.
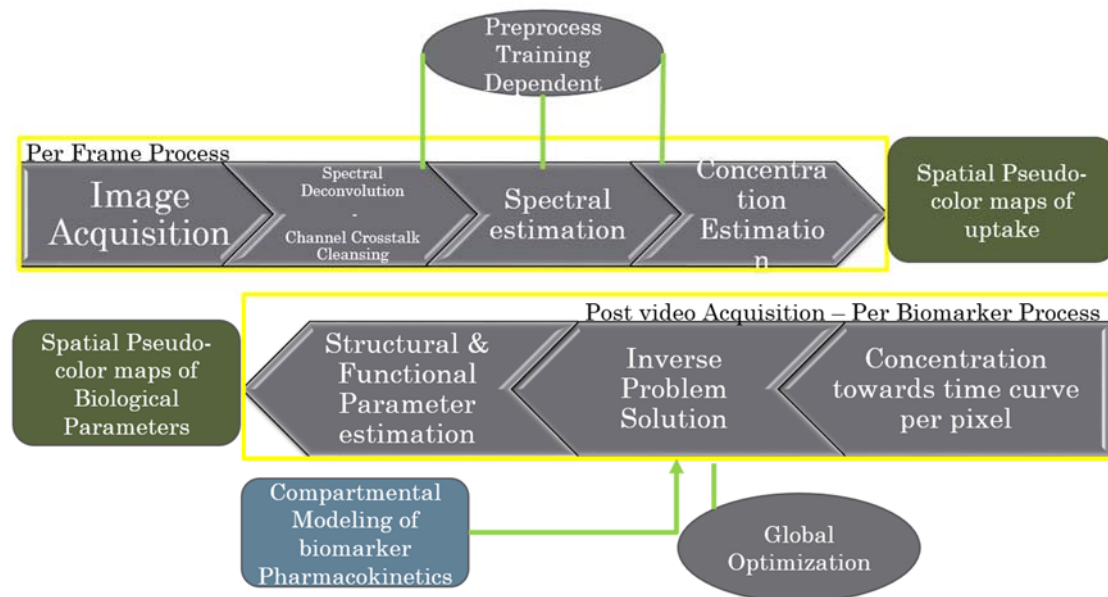
Figure 59 Multiband Dynamic Molecular Imaging workflow

In conclusion, a real time spectral imaging modality of high spectral accuracy, fidelity and resolution is proposed initially for the visible range of the electromagnetic spectrum, constraint only by a priori knowledge of the sensitivity of the imaging components. A priori knowledge of the spectral profile of biomarkers in question, once incorporated to the modality, allow for imaging of simultaneous application of multiple biomarkers and identification of the spatial profile of their concentration on a single tissue specimen. This capability, allows real time spectral imaging of dynamic phenomena induced by the biomarkers, by recording the temporal response of biomarker-tissue interaction. This temporal response of each biomarker can be fitted to simulated response, produced by bio-mathematical model for each biomarker, and provide valuable biological information of structural and functional parameters of tissue.

Focusing on Acetic Acid in the case of Cervical Intraepithelial Neoplasia fitting of the response is found adequate and requires a minimal time to be performed in high resolution frame. Findings of this procedure agree to medical golden standards (biopsy). Our findings suggest strongly that our method can improve our understanding of the neoplasia development mechanisms and of tumour growth and metastasis physiology. Corollary, it may become a valuable diagnostic tool that will also facilitate the development and evaluation of new cancer therapies and guided personalised medicine. At the same time, the method developed encompasses the potentials of a novel screening method by laying the foundations towards optical biopsy.

Finally, the paramount advantage of this imaging modality stand to the wide field of applications it can be incorporated into. First and foremost it stands alone as a valuable low cost real time multiband imaging system. Thusly, dynamic phenomena can be observed across a wide field of the electromagnetic spectrum in real time. Moreover, it holds the potential of observing the spatiotemporal uptake of biomarkers and stains, which provides quantitative data of biological and biomedical value. Furthermore, more elaborate analysis of these observed data as described in the case of Cervical Intraepithelial Neoplasia, provides even more detailed and quantitative structural and functional information of the underlying tissue non-invasively and in vivo.

7.2 Future work

Despite these very good initial results, a higher confidence and accuracy, with regards to the snapshot spectral imaging after spectra deconvolution and channel cross-talk cleansing needs to be established for medical applications. Before moving to a possible clinical testing of the modality spectral fidelity and accuracy of the estimation must remain consistent and with the most negligible deviation.

Higher resolution of the matrix weight by incorporating knowledge of the spectral signature of the available light source. Moreover, expanding the methodology towards the infrared and the ultraviolet region of the electromagnetic field holds potential for identification of a more broad set of potential stains and biomarkers.

Furthermore, a database of spectral signatures of biomarkers and stains with their corresponding concentrations needs to be established, in order for the modality to be able to recreate pseudo-colour maps of their spatial distributions.

Moreover, pharmacokinetics of biomarkers need to be studied in order for their corresponding bio-mathematical and bio-physical models to be formulated, towards molecular imaging based on the pharmacodynamics of the tissue after application of the biomarkers. For instance, the pharmacodynamics of Lugol's iodine could provide a second bio model of the Cervical Intraepithelial Neoplasia. Once established, the joint dynamic phenomenon of simultaneous application of Acetic Acid and Lugol's iodine can be studied and a combined response model can be formulated and compared towards the individual components.

Finally, reduction of temporal complexity and increase in convergence accuracy of the stated in this thesis inverse problem can be explored, by increase of the LUT size and development of a more elaborated and optimized LUT search method as well as using biophysical or tissue feature based models [70] as masks to limit the targeted pixel size. On the same time, downgrading of the global optimization algorithm to a faster script language needs to be established and studied towards time and accuracy improvement. Based on findings of these two courses of action a hybrid solution to the inverse problem can be introduced.

References

[1] World Health Organisation repository, apps.who.int/classifications/icd10/browse/2010/en

[2] D.Hanahan, R.A.Weinberg, "Hallmarks of Cancer", Cell, vol 100, page 57-70, 2000

[3] D.Hanahan, R.A.Weinberg, "Hallmarks of Cancer: The Next Generation", Cell, vol 144, page 646-74, 2011

[4] National Cancer Institute, cancer.gov

[5] A.Marusyk, K.Polyak, "Tumor heterogeneity: causes and consequenses", Biochimica et Biophysica Acta – Reviews on Cancer, vol 1805, issue 1, pages 150-117, Jan 2010

[6] V.R.Zellmer, S.Zhang, "Evolving concepts of tumor heterogeneity", Cell & Bioscience, vol 4, issue 69, page 1, 2014

[7] T.A. Yap, M. Gerlinger, P.A. Futreal, L.Pusztai, C.Swanton, "Intratumor heterogeneity: seeing the wood for the trees", Sci Transl Med., vol 4, issue 127, pages 127ps10, 2012

[8] Q.Wang, R.Chaerkady, J.Wu, H.Jung Hwang, N.Papadopoulos, L.Kopelovich, A.Maitra, H.Matthaei, J.R.Eshleman, R.H.Hruban, K.W.Kinzler, A.Pandey,B.Vogelstein , "Mutant proteins as cancer-specific biomarkers", Proceedings of the National Academy of Sciences of the USA, vol 108, no 6, pages 2444-2449, 2010

[9] Z.Tezak, M.V.Kondratovich, E.Mansfield, "US FDA and personalised medicine: in vitro diagnostic regulatory perspective", Personalized Medicine, volume 7, issue 5, page 517-530, 2010

[10] I.Wang, Photodynamic therapy and laser-based diagnostic studies of malignant tumours, Dissertation thesis, Lund University, Lund, Sweden (1999).

[11] J.Mobley and T.Vo-Dinh, Optical properties of tissue, in biomedical photonics handbook, ed.T.Vo-Dinh, pp. 2-1-2-74 (CRC Press, Boca Raton, 2005).

[12] S.L.Jacques and S.A.Prahl. Optical properties, Http://omlc.ogi.edu, (1998).

[13] S.L.Jacques, Reflectance spectroscopy with optical fiber devices, and transcutaneous bilirubinometers, in biomedical optical instrumentation and laser-assisted biotechnology, eds. A.M.Verga Scheggi, S.Martellucci, A.N.Chester and R.Pratesi, pp. 83-94 (Kluwer Academic Publishers, Dordrecht, 1996).

[14] J.R.Mourant, J.P.Freyer, A.H.Hielscher, A.A.Eick, D.Shen and T.M.Johnson, Mechanisms of light scattering from biological cells relevant to noninvasive optical-tissue diagnostics, Appl. Opt. 37, 3586- 3593 (1998).

[15] S.Jacques, Origins of tissue optical properties in the UVA, visible, and NIR Regions, OSA TOPS on Advances in Optical Imaging and Photon Migration, vol. 2, 364-369 (1996)

[16] Bodkin, A., Sheinis, A., Daly, J., Beaven, S., Weinheimer, J. "Snapshot Hyperspectral Imaging – the Hyperpixel Array Camera", Proc. SPIE, 7334-17, (2009)

[17] S. A. Mathews, "Design and fabrication of a low-cost, multispectral imaging system," Applied Optics 47: F71-F76 (2008).

[18] A. Wagadarikar, R. John, R. Willett, and D. Brady, "Single disperser design for coded aperture snapshot spectral imaging," Applied Optics 47: B44-B51 (2008).

[19] L. Gao, R. T. Kester, T. S. Tkaczyk, "Compact Image Slicing Spectrometer (ISS) hyperspectral fluorescence microscopy", Optics Express 17: 12293-12308 (2009).

[20] A. Gorman, D. W. Fletcher-Holmes, and A. R. Harvey, "Generalization of the Lyot filter and its application to snapshot spectral imaging," Optics Express 18: 5602-5608 (2010)

[21] N. Gupta, P. R. Ashe, and S. Tan, "Miniature snapshot multispectral imager", Optical Engineering 50: 033203 (2011).

[22] D.Anglos, C.Balas, C.Fotakis, "Laser spectroscopic and optical imaging techniques in chemical and structural diagnosis of painted artworks" ,Am.Lab.(October)(1999)60–67.

[23] C.Balas, "An imaging method and apparatus for the non-destructive analysis of paintings and monuments", International PatentApp. PCT/GR00/00039.

[24] C.Balas, "A novel optical imaging method for the early detection, quantitative grading and mapping of cancerous and precancerous lesions of cervix", IEEE Trans. Biomed. Eng. 48(2001)96–104.

[25] G. Epitropou, V.Kavvadias, D.Iliou, E.Stathopoulos, C.Balas, "A Real-Time Spectral Mapper as an Emerging Diagnostic Technology in Biomedical Sciences", 15th Annual International Conference of the IEEE EMBS, Osaka, Japan, 2013

[26] K,Hirakawa, "Cross-Talk Explained", 15th IEEE International Conference on Image Processing, San Diego, USA, 2008

[27] V.Kavvadias, "Simultaneous Multi-Spectral Imaging System: Application in Real-Time, Unsupervised Spectral Classification in Endometrial Endoscopy", Master Thesis, 2013

[28] D.Iliou, "Hyper Spectral Data Estimation from Power Dimensionality Experimental Imaging", Master Thesis, 2014

[29] C.Rossos, "Development of a Computer Controlled Tunable Wavelength Light Source from Ultraviolet to Infrared", Diploma Thesis, 2013

[30] Kobus Barnard, Brian Funt. "Camera Characterization for Color Research". COLOR research and application, Volume 27, Number 3, June 200

[31] Kruse, F. A., A. B. Lefkoff, J. B. Boardman, K. B. Heidebrecht, A. T. Shapiro, P. J. Barloon, and A. F. H. Goetz, 1993, "The Spectral Image Processing System (SIPS) - Interactive Visualization and Analysis of Imaging spectrometer Data." *Remote Sensing of Environment*, v. 44, p. 145 - 163.

[32] D.Gkotsoulias, "Development of hyperspectral microscopy for improving the diagnostic accuracy in leukemia diagnosis", Diploma Thesis, 2016

[33] E.P.Armstrong, "Prophylaxis of Cervical Cancer and Related Cervical Disease: A Review of the Cost-Effectiveness of Vaccination Against Oncogenic HPV Types". *Journal of Managed Care Pharmacy,* vol.16, no.3, pp. 217–30, Apr.2010

[34] World Health Organization, "*Fact sheet No. 297: Cancer*", Feb 2006, Retrieved 2007-12-01

[35] Garcia A Hamid O, El-Khoueiry A (2006-07-06). "Cervical Cancer". *eMedicine*. WebMD. Retrieved 2007-12-02.

[36] Dolinsky, Christopher (2006-07-17). "Cervical Cancer: The Basics". *OncoLink* (Abramson Cancer Center of the University of Pennsylvania). Retrieved 2007-12-02.

[37] International Agency for Research on Cancer, "Colposcopy and Treatment of Cervical Intraepithelial Neoplasia: A Beginner's Manual / Chapter 2: An Introduction to Cervical Intraepithelial Neoplasia (CIN) "

[38] World Health Organization, *Comprehensive cervical cancer control: A guide to essential practice* [Online]: http://www.who.int/cancer/detection/cervical_cancer_screening/en/index.html

[39] M. Schiffman,P. E. Castle, "The promise of global cervical-cancer prevention," New England Journal of Medicine, vol. 353, pp. 2101-2104, 2005

[40] E.H. Hopman, F.J. Voorhorst, P. Kenemans, C. Meyer, T.J.M. Helmerhorst, " Observer Aggreement on interpreting Colposcopic Images of CIN", *Gynecologic Oncology,* vol.58,pp. 206-209, 1995

[41] D. Solomon, M. Schiffman, R. Tarone, E. E. Partridge, L. Kilgore, S. Hester, J. L. Walker, G. A. Johnson, A. Yadack, R. S. Guido, K. McIntyre-Seltman, R. P. Edwards, J. Gruss, N. B. Kiviat, L. Koutsky, C. Mao, J. M. Haug, D. Ferris, J. T. Cox, L. Burke, C. M. Wheeler, C. Peyton-Goodall, M. M. Manos, R. J. Kurman, D. L. Rosenthal, M. E. Sherman, M. H. Stoler, D. M. Harper, J. Rosenthal, M. Dunn, J. Quarantillo, D. Robinson, A. T. Lorincz, and L. Rich, "A randomized trial on the management of low-grade squamous intraepithelial lesion cytology interpretations," *American Journal of Obstetrics and Gynecology*, vol. 188, pp. 1393-1400, 2003.

[42] S. F. Wu, L. Meng, S. X. Wang, and D. Ma, "A comparison of four screening methods for cervical neoplasia," *International Journal of Gynecology & Obstetrics*, vol. 91, pp. 189-193, 2005

[43] C. Yue, "The Promise of Dynamic Contrast-Enhanced Imaging in Radiation Therapy," Semin. Radiat. Oncol., vol. 2, no. 21, pp. 147–156, 2011.

[44] Z. M. Bhujwalla, D. Artemov, P. Ballesteros, S. Cerdan, R. J. Gillies, and M. Solaiyappan, "*Combined vascular and extracellular pH imaging of solid tumors.*," NMR Biomed., vol. 15, no. 2, pp. 114–9, Apr. 2002

[45] Y. Hama, Y. Koyama, P. L. Choyke, and H. Kobayashi, "*Two-color in vivo dynamic contrast enhanced pharmacokinetic imaging.*," J. Biomed. Opt., vol. 12, no. 3, p. 034016, 2007

[46] M. A. Rosen and M. D. Schnall, "*Dynamic contrast-enhanced magnetic resonance imaging for assessing tumor vascularity and vascular effects of targeted therapies in renal cell carcinoma.*," Clin. Cancer Res., vol. 13, no. 2 Pt 2, pp. 770–776, Jan. 2007

[47] C. Balas , A. Dimoka, I.Orfanudaki and E. Koumantakis, "*In vivo assessment of acetic acid-cervical tissue interaction using quantitative imaging of back-scattered light: its potential use for the in vivo cervical cancer detection grading and mapping*", SPIE-Optical Biopsies and Microscopic Techniques, vol. 3568, pp.31-37, 1999

[48] C. Balas, et al., "*In vivo detection and staging of epithelial dysplasias and malignancies based on the quantitative assessment of acetic acidtissue interaction kinetics*", Jour. Photoch. Photob. B-Biol., vol. 53, no. 1-3, pp. 153-157, 1999

[49] C. Balas, *"A Novel Optical Imaging Method for the Early Detection, Quantitative Grading and Mapping of Cancerous and Precancerous lesions of Cervix"*, IEEE-Transactions on Biomedical Engineering, vol. 48, No 1, pp. 96-104, 2001

[50] C.Balas, G.Papoutsoglou, A.Potirakis, "*In Vivo Molecular Imaging of Cervical Neoplasia Using Acetic Acid as Biomarker*", vol. 14,no.1, Jan 2008

[51] Louwers J, Zaal A, Kocken M, ter Harmsel W, Graziosi G, Spruijt J, Berkhof J, Balas C, Papagiannakis E, Snijders P, Meijer C, van Kemenade F, Verheijen R. *Dynamic spectral imaging colposcopy: higher sensitivity for detection of premalignant cervical lesions*. BJOG 2010; DOI: 10.1111/j.1471-0528.2010.02806.x, Dec 2010

[52] Eurocytology "Anatomy, histology and function of the uterine cervix" http://www.eurocytology.eu/en/course/930

[53] University of Greenwich, CMS staff, "An introduction to Mathematical Modeling", [Online]: http://staffweb.cms.gre.ac.uk/~st40/Books/MathematicalModelling

[54] G.Papoutsoglou, "Modelling of epithelial transport phenomena related with the acetowhitening optical characteristics: Potential for the *in-vivo* diagnosis of Cervical Neoplasia", M.S. thesis, ECE, Tech University of Crete, Greece, 2007

[55] G.Papoutsoglou, C. Balas,"Estimation of Neoplasia-Related Biological Parameters through Modeling and Sensitivity Analysis of Optical Molecular Imaging Data", Research Support, Department of Electronic and Computer Engineering, Tech University of Crete, Dec 2012.

[56] C. G. Moles, P. Mendes, and J. R. Banga, "Parameter estimation in biochemical pathways: a comparison of global optimization methods.," Genome Res., vol. 13, no. 11, pp. 2467–74, Nov. 2003

[57] T.M. Giakoumakis, "Global Optimization analysis of dynamic optical data for the in-vivo diagnosis of epithelial neoplasia", Diploma Thesis, 2013

[58] G. Papoutsoglou, T.-M. Giakoumakis, and C. Balas, "Dynamic contrast enhanced optical imaging of cervix, in vivo: A paradigm for mapping neoplasia-related parameters.," in Conference proceedings : . Ann. Int. Conf. of the IEEE Eng. in Med. and Biology Society. IEEE Eng. in Med. and Biology Society. Conf., 2013, vol. 2013, pp. 3479–82.

[59] S.Das, P.N.Sugathan, "Differential Evolution: A Survey of the State-of-the-Art", *IEEE Transactions on Evolutionary Computation,* vol.15, no.1, pp.4-31, Feb 2011

[60] R.Storn, K.Price, "Differential Evolution - A Simple and Efficient Heuristic for Global Optimization over Continuous Spaces", *Journal of Global Optimization*, vol.11, pp.341-359,1997

[61] E. Magnus ,P. Hvass, "Good Parameters for Differential Evolution", Hvass Laboratories, Tech Rep no. HL1002, 2010.

[62] D.U. Lee, A. Abdul Gaffar, O. Mencer, W. Luk, "Optimizing Hardware Function Evaluation", IEEE Tras. Comput., vol. 54, pp. 1520-1531, Dec. 2005

[63] J.-H. Zhang and Z.-X. Yao, "Globally optimized finite-difference extrapolator for strongly VTI media", Geophysics, vol. 77, no. 4, pp. T125-T135, Jul.-Aug. 2012

[64] W. Dorigo, R. Richter and A. Müller, "A LUT Approach for Biophysical Parameter Retrieval by RT Model Inversion Applied to Wide Field of View Data", Proc. 4th EARSeL Workshop on Imaging Spectroscopy, Warsaw, pp. 599-607, 2005

[65] Y. Onishi, Y. Yonekura, S. Nishizawa, et al., "Noninvasive Quantification of Iodine-123-Iomazenil SPECT", J. Nucl. Med., vol. 37, no.2, pp. 374-378, 1996

[66] H. Kato, E. Shimoseqawa, K. Isohashi, et. al., "Distribution of Cortical Benzodiazepine Receptor Binding in Right-Handed Healthy Humans: A Voxel-Based Statistical Analysis of Iodine-123-Iomazenil SPECT with Partial Volume Correction", Am. J. Neuroradiol., vol.33, no.8, pp.1458-1463, Sep. 2012

[67] B. S. Nichols, N. Rajaram, J. W. Tunnell, "Performance of a lookup table-based approach for measuring tissue optical properties with diffuse optical spectroscopy",J. of Biomed. Opt., vol.17, no. 5, 057001, May 2012

[68] P. A. Schornack and R. J. Gillies, "Contributions of cell metabolism and H^+ diffusion to the acidic pH of tumors," *Neoplasia*, vol. 5, no. 2, pp 135-145, 2003.

[69] A. Singer, J. Monaghan, and S. Quek, "Lower genital tract precancer: colposcopy, pathology and treatment". Oxford, England: Wiley-Blackwell, 2000, p. 323.

[70] A. Savva, "*Analysis and Quantification of Spatiotemporal Features of Diagnostics Importance in Cervical Neoplasia*", Diploma Thesis, 2015